RCA REVIEW

a technical journal

RADIO AND ELECTRONICS
RESEARCH • ENGINEERING

VOLUME XVIII MARCH 1957 NO. 1

PRINTED IN U.S.A.

RCA REVIEW, published quarterly in March, June, September, and December by RCA Laboratories, Radio Corporation of America, Princeton, New Jersey. Entered as second class matter July 3, 1950 at the Post Office at Princeton, New Jersey, under the act of March 3, 1879. Subscription price in the United States and Canada; one year $2.00, two years $3.50, three years $4.50; in other countries: one year $2.40, two years $4.30, three years $5.70. Single copies in the United States, $.75; in other countries, $.85.

RCA REVIEW

a technical journal

RADIO AND ELECTRONICS
RESEARCH • ENGINEERING

Published quarterly by
RCA LABORATORIES
in cooperation with all subsidiaries and divisions of
RADIO CORPORATION OF AMERICA

VOLUME XVIII MARCH, 1957 NUMBER 1

CONTENTS

RCA REVIEW is regularly abstracted and indexed by *Industrial Arts Index Science Abstracts* (I.E.E.-Brit.), *Electronic Engineering Master Index, Chemical Abstracts, Proc. I.R.E., and Wireless Engineer.*

RCA REVIEW

BOARD OF EDITORS

SPACE-CHARGE LIMITATION ON THE FOCUS OF ELECTRON BEAMS

By

J. W. Schwartz

RCA Laboratories,
Princeton, N. J.

Summary—*The motion of electrons within a homocentric uniform-density beam in the presence of space-charge forces is examined. A universal curve for the smallest spot size at the target is obtained. At high beam currents this differs significantly from available curves for the beam cross section at the point of zero radial velocity.*

Introduction

Several papers discussing the effect of mutual electron repulsion on the focus of electron beams have appeared in the past. One of the better known of these is that of Thompson and Headrick.[1]

In cathode-ray tubes and similar electron devices, the smallest spot at the screen is not necessarily obtained by focusing the beam in the plane of the screen. If beam space charge is a significant factor, the smallest spot is obtained by focusing on a plane between the gun and screen. Thompson and Headrick have discussed this phenomenon and indicate how the minimum spot size may be obtained. Their procedure involves the plotting of a multiplicity of beam envelopes for each particular set of electrical and geometrical conditions.

An analytical method of finding the minimum spot size is presented here.[2] Furthermore, a single universal expression that is valid for any current, voltage, beam length, etc. is obtained.

Statement of the Problem

Figure 1 shows the superposition of two idealized electron beams.* The beams have equal currents, voltages, initial diameters and axial

---

[1] B. J. Thompson and L. B. Headrick, "Space Charge Limitations on the Focus of Electron Beams," *Proc. I.R.E.*, Vol. 28, p. 318, July, 1940.

[2] Since the completion of this work, it has come to the author's attention that a somewhat equivalent treatment has been developed by D. L. Hollway: "The Optimum Space-Charge Controlled Focus of an Electron Beam," *Australian Journal of Scientific Research*, Series A, Vol. 5, pp. 430-436, 1952.

* The electron beams discussed in this paper are idealized in certain respects. Thermal velocities, finite source size, etc. are neglected. See Reference (1) for a complete statement of the customary assumptions.

lengths. One beam, however, is focused in such a manner that its minimum cross section occurs at the screen. The other beam has its minimum cross section somewhat ahead of the screen. Since the focus point of the first crossover occurs at a greater axial distance from the gun than that of the second, the radius of the second crossover is of necessity smaller than the first. In fact, the cross section at the screen of the second beam is smaller than that of the beam whose minimum cross section occurs at the screen.

The purpose of this paper is to present a derivation of an expression for the beam size at the screen when the beam is focused in such a manner as to cause the smallest possible spot at the screen.

An outline of the derivation and the final expression are presented in the following section; the complete derivation may be found in the Appendix.

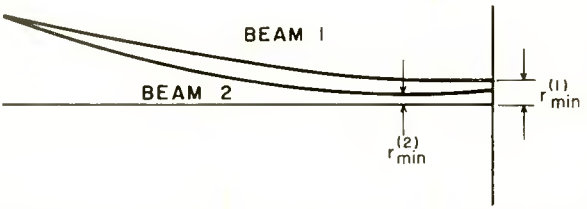

Fig. 1—Cross section of electron beams. Beam 1 is focused for minimum beam cross section at the screen; beam 2 for smallest spot size at the screen.

Universal Expression for the Smallest Spot Size

The time of flight, T, of an electron path coincident with the outside contour of an electron beam is given by the following expression:

$$T = \pm \frac{1}{K} \int_{\text{Beam Contour}} \frac{dr}{\sqrt{\log \frac{r}{r_i} + \frac{\dot{r}_i^2}{K^2}}} \tag{10}$$

Here K is a constant which depends upon beam current and voltage, r the instantaneous radial displacement of the electron along the path, and r_i, and $\dot{r}_i$ the initial beam radius and slope respectively. With the beam length and voltage known, T can be determined. The path of the integral depends upon beam voltage, current, and upon $\dot{r}_i$ and r_i. The final limit of the integral is r_s, the spot size on the screen. Equation (10) is differentiated with respect to r_i holding the other parameters constant in order to find the path yielding the stationary

value of r_s. A transcendental equation involving only the normalized spot size, r_s/r_i, and the quantity $r_i K$, is obtained.

Figure 2 is a graph of a numerical solution of the transcendental equation. It is a universal relationship for the minimum spot size obtainable at the screen for any choice of beam length, Z; voltage, V; current, I; and initial diameter, $2r_i$. A curve which indicates the spot size for the condition where the beam is focused in such a manner that its minimum cross section occurs in the plane of the screen is also shown in Figure 2. At low currents the two curves coincide. At larger currents, however, the smallest spot size at the screen is appreciably smaller than the spot obtained when the minimum beam cross

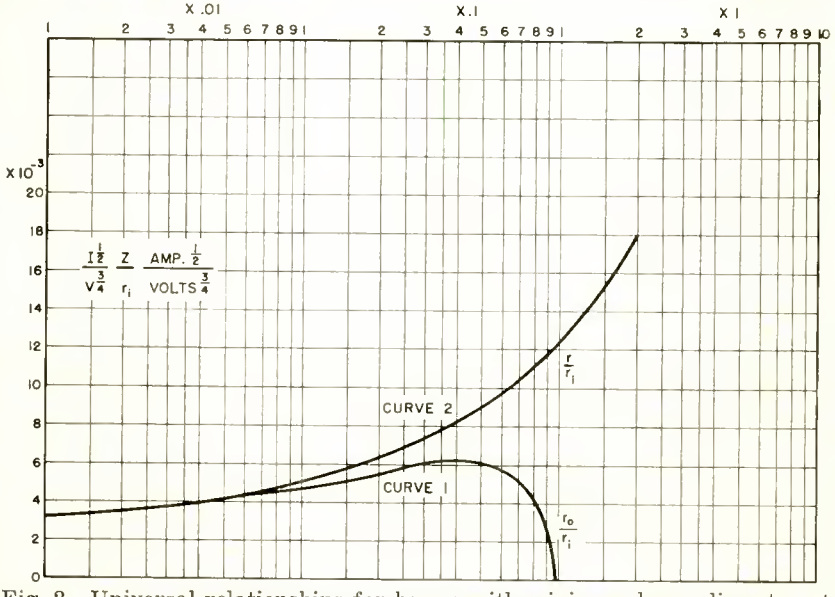

Fig. 2—Universal relationships for beams with minimum beam diameter at the screen (curve 1) and for minimum spot size at the screen (curve 2).

section is made to occur at the screen. In fact, beyond a limiting current of about $4 \times 10^{-5}\ V^{3/2}\ r_i^2/Z^2$ (amperes), the minimum beam cross section cannot be made to occur in the plane of the screen.

The abscissa of Figure 2 is the ratio of the final and initial beam radii and consequently is dimensionless. The ordinate, however, is proportional to the square root of the current and inversely proportional to the ¾ power of the beam potential. Since this is not dimensionless, the curve applies only when this current is expressed in amperes and the potential in volts. For example, at a current of 10^{-2} ampere, a potential of 10^4 volts, beam length of 10 inches, and initial radius of 8×10^{-2} inch, the ordinate is

$$\frac{I^{1/2}}{V^{3/4}} \times \frac{Z}{r_i} = \frac{10^{-1}}{10^3} \times \frac{10}{8 \times 10^{-2}} = 12.5 \times 10^{-3}.$$

Referring to the curves of Figure 2, it is seen that the smallest obtainable spot size is 1.0 times the initial beam size. Curve No. 1 indicates that the beam current is about four times too high to allow the smallest beam cross section to occur at the screen.

Appendix

The following notation is used in the derivation:

r = Instantaneous radius of an electron on the edge of the beam,

$\dot{r}$ = first time derivative of r,

$\ddot{r}$ = second time derivative of r,

r_o = beam radius at the beam minimum cross section,

r_i = initial beam radius, radius at the gun,

r_s = beam radius at the screen,

Z = gun to screen axial distance,

t = time (seconds),

T = gun to screen electron transit time,

I = beam current (amperes),

V = beam potential (volts),

η = electronic charge to mass ratio
$(= e/m = 1.76 \times 10^{11}$ coulomb/kilogram),

ϵ = permitivity of vacuum
$(= 8.85 \times 10^{-12}$ farads/meter),

$K = [\eta I/(\pi\epsilon\sqrt{2\eta V})]^{1/2}$ meters/second,

u = an integration variable
$(= \pm\sqrt{\log r/r_i + \dot{r}_i^2/K^2})$,

$u_s = \sqrt{\log r_s/r_i + \dot{r}_i^2/K^2}$,

$u_o = \sqrt{\log r_o/r_i + \dot{r}_i^2/K^2} = 0$,

$U(x)$ = a non-elementary function, $\equiv \int_0^x e^{u^2} du$,

$W = \dot{r}_i/K$,

$p = r_s/r_i$,

$$f(W,p) = 2\,We^{-W^2}\,(U(u_s) + U(W)),$$

$$g(W,p) = 1 + p\,W/u_s,$$

$\beta =$ value of W for which $g(W,p) = f(W,p)$.

Figure 3 illustrates the usage of the geometrical symbols.

By a simple application of Gauss's law the electric field just outside a long cylinder of charge is found to be

$$\frac{I}{2\pi\epsilon\, r\sqrt{2\eta V}}.$$

Hence in an otherwise field-free region the motion of electrons under the influence of space charge must satisfy the following relation:

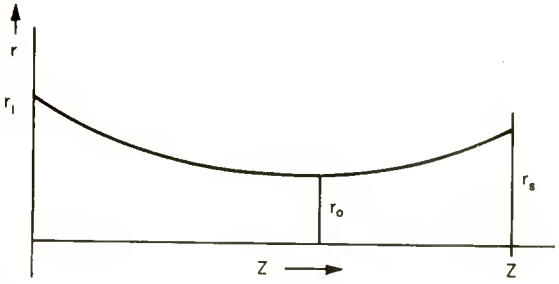

Fig. 3—Beam cross section showing usage of geometrical symbols.

$$\ddot{r} - \frac{\eta I}{2\pi\epsilon\, r\sqrt{2\eta V}} = 0. \tag{1}$$

If Equation (1) is multiplied by $\dot{r}$,

$$\ddot{r}\,\dot{r} - \frac{\eta I}{2\pi\epsilon\sqrt{2\eta V}}\,\frac{\dot{r}}{r} = 0, \tag{2}$$

or, for simplicity,

$$\ddot{r}\,\dot{r} - \frac{K^2}{2}\,\frac{\dot{r}}{r} = 0. \tag{3}$$

But, Equation (3) is an exact differential

$$1/2\,\frac{d}{dt}\left\{(\dot{r})^2 - K^2 \log r\right\} = 0. \tag{4}$$

Hence

$$(\dot{r})^2 - K^2 \log r = \text{constant}. \tag{5}$$

Substituting the initial conditions $r = r_i$, $\dot{r} = \dot{r}_i$, and $t = 0$, (6)

$$\dot{r}^2 - \dot{r}_i^2 - K^2 \log \frac{r}{r_i} = 0. \tag{7}$$

This may be written

$$\frac{dr}{dt} = \sqrt{K^2 \log \frac{r}{r_i} + \dot{r}_i^2}. \tag{8}$$

Then

$$KT = \int_{\text{Beam}} \frac{\mathrm{dr}}{\sqrt{\log \frac{r}{r_i} + \frac{\dot{r}_i^2}{K^2}}}. \tag{10}$$

Since r first decreases from r_i to r_o and then increases to some value r_s,

$$KT = -\int_{r_i}^{r_o} \frac{dr}{\sqrt{\log \frac{r}{r_i} + \frac{\dot{r}_i^2}{K^2}}} + \int_{r_o}^{r_s} \frac{dr}{\sqrt{\log \frac{r}{r_i} + \frac{\dot{r}_i^2}{K^2}}}. \tag{11}$$

For convenience let

$$u^2 \equiv \log \frac{r}{r_i} + \frac{\dot{r}_i^2}{K^2}. \tag{12}$$

Then

$$2u\, du = \frac{dr}{r}, \tag{13}$$

$$r = r_i\, e^{u^2 - \dot{r}_i^2/K^2}, \tag{14}$$

and

$$u = \pm \sqrt{\log \frac{r}{r_i} + \frac{\dot{r}_i^2}{K^2}}. \tag{15}$$

The sign of the square root was taken as negative in the first term and positive in the second term of Equation (11). This was necessary since both sides of Equation (11) must increase monotonically as an electron traces out a path in time. For consistency then, the same sign selection must be made in the application of Equation (15) to the two regions.

Substituting Equations (13), (14), and (15) into Equation (11) gives

$$KT = 2r_i\, e^{-r_i^2/K^2}\left[\int_{u_o}^{-\dot{r}_i/K} e^{u^2}\,du + \int_{u_o}^{u_s} e^{u^2}\,du\right]. \tag{16}$$

When $r = r_o$, however, $dr/dt = 0$. Hence setting Equation (8) equal to zero one obtains

$$K^2 \log \frac{r_o}{r_i} = -\dot{r}_i^2, \tag{17}$$

or

$$r_o = r_i e^{-\dot{r}_i^2/K^2}. \tag{18}$$

Defining $-\dot{r}_i/K \equiv W$, a positive number, and combining Equation (18) with Equation (16) yields

$$KT = 2r_i e^{-W^2}\left[\int_0^{W} e^{u^2}\,du + \int_0^{u_s} e^{u^2}\,du\right]. \tag{19}$$

Let $U(x)$ be defined by the equation

$$U(x) \equiv \int_0^{x} e^{u^2}\,du. \tag{20}$$

Then Equation (19) becomes

$$KT = 2r_i e^{-W^2}\,[U(W) + U(u_s)]. \tag{21}$$

Remembering that u_s is a function of W, Equation (21) is differentiated with respect to W. This is equivalent to differentiation with respect to $\dot{r}_i$ for fixed beam voltage, current, beam length, and initial diameter. The result is set equal to zero in order to obtain the stationary condition with respect to $\dot{r}_i$.

$$-4Wr_i e^{-W^2}[U(W)+U(u_s)]+2r_i e^{-W^2}\left[e^{+W^2}+\frac{e^{u_s^2}W}{u_s}\right]=0. \quad (22)$$

$$2We^{-W^2}[U(W)+U(u_s)]=1+\frac{r_s}{r_i}\frac{W}{u_s}. \quad (23)$$

If a new parameter, p, be defined by $p \equiv r_s/r_i$, Equation (23) may then be written as

$$2We^{-W^2}[U(W)+U(\log p+W^2)]=1+\frac{pW}{\sqrt{\log p+W^2}}. \quad (24)$$

Tables[3] of $U(x)$ are available. Equation (24) therefore establishes a useful universal relationship between p, the normalized spot size and W. It will be noted that W depends only upon the axial beam velocity ($\sim \sqrt{V}$), the initial radial velocity of an outside electron, and the beam current.

Equation (21) is an equation in the same variables as Equation (24) but also involves the parameter T, the time of flight of an electron from gun to screen. Parameter T is given by

$$T=\frac{Z}{\sqrt{2\eta V}}. \quad (25)$$

Here, Z is the beam length.

The desired relation between V, I, r_i, r_s, and Z may be obtained as follows: Define

$$f(W,p) \equiv 2We^{-W^2}(U(u_s)+U(W)), \quad (26)$$

$$g(W,p) \equiv 1+p\frac{W}{u_s}.$$

Select a value of p and plot f and g versus W. The intersection of f and g occurs at some value of W which we may call β. If the process is repeated for a multitude of values of p, a curve of β versus p is established.

---

[3] H. M. Terrill and L. Sweeny, "An Extension of Dawson's Table of the Integral of e^{x^2}," *Jour. Frank. Inst.*, Vol. 237, p. 495, June, 1944; "Table of the Integral of e^{x^2}," *Jour. Frank. Inst.*, Vol. 238, p. 220, September, 1944.

If, now, W in Equation (21) is replaced by β, Equation (24), the minimization constraint on r_s is satisfied. Using the value of T from Equation (25),

$$\frac{KZ}{\sqrt{2\eta V}} = 2r_i e^{-\beta^2} \left(U(\beta) + U(u_s(\beta))\right). \tag{27}$$

In terms of $f(\beta)$ Equation (27) may also be written

$$\sqrt{\frac{\eta I}{\pi e \sqrt{2\eta V}}} \frac{Z}{\sqrt{2\eta V}} \frac{1}{r_i} = \frac{f(\beta)}{\beta}, \tag{28}$$

or

$$174 \frac{I^{1/2}}{V^{3/4}} \cdot \frac{Z}{r_i} = \frac{f(\beta)}{\beta}. \tag{29}$$

Equation (29) is a universal relationship among V, I, Z, r_i, and r_s for the condition that r_s is the smallest possible value. Since β depends only on p $(= r_s/r_i)$, one may plot a single universal curve of

$$\frac{r_s}{r_i} \text{ versus } \frac{I^{1/2}Z}{V^{3/4}r_i}.$$

If the focus is adjusted so that the beam has its minimum cross-section, r_o, at the screen, a similar universal relationship holds. Both curves are shown in Figure 3.

DESIGN, CONSTRUCTION, AND HIGH-FREQUENCY PERFORMANCE OF DRIFT TRANSISTORS

By

A. L. Kestenbaum and N. H. Ditrick

RCA Semiconductor Division,
Somerville, N. J.

Summary—This paper describes a method of fabricating drift-transistor structures[1] by combining solid-phase diffusion with alloy-junction techniques. Design considerations pertaining to devices made in this manner are presented. The electrical characteristics of developmental drift transistors are related to their physical structure and data are given describing their performance as high-frequency amplifiers.

Introduction

In early approaches to the problem of extending the high-frequency range of junction transistors, the size of the conventional alloy-junction and grown-junction structures was scaled down. Two outgrowths were the "tetrodizing"[2] of the grown structure which, in effect, electrically reduces the junction areas and base resistance, and the development of electrochemical etching and plating techniques[3] for providing a thin base layer and small junction areas without changing the configuration of the alloy structure.

The most significant advances, however, have resulted from the development of the drift[1,4,5] and p-n-i-p[6] structures, both of which greatly extend the theoretical frequency limit of the junction transistor. Of the two, the drift structure not only possesses slightly superior frequency possibilities,[5] but is also more feasible to construct as a result of recent improvements in the technique of solid-phase impurity

---

[1] H. Kroemer, "Der Drifttransistor," *Naturwissenschaften*, Vol. 40, p. 578, December, 1953.

[2] R. L. Wallace, Jr., L. G. Schimpt, and E. Dickten, "A Junction Transistor Tetrode for High-Frequency Use," *Proc. I.R.E.*, Vol. 40, p. 1395, November, 1952.

[3] W. E. Bradley et al, "The Surface-Barrier Transistor," *Proc. I.R.E.*, Vol. 41, p. 1702, December, 1952.

[4] H. Kroemer, "Zur Theorie des Diffusions und des Drifttransistors," *Archiv der Elektrischen Ubertragung*, Vol. 8, 1954.

[5] H. Kroemer, "The Drift Transistor," *Transistors I*, RCA Laboratories, Princeton, N. J., 1956, p. 202.

[6] J. M. Early, "P-N-I-P and N-P-I-N Junction Transistor Triodes," *Bell Sys. Tech. Jour.*, Vol. 33, p. 517, May, 1954.

diffusion in semiconductors. The accurate control of impurity distribution obtainable with the diffusion technique has made it possible to construct the extremely thin graded impurity region that produces an accelerating field for minority carriers in the base region of a drift transistor.

The impurity distribution in a p-n-p drift transistor is shown graphically in Figure 1. The high-frequency properties of this structure may be summarized by referring to the commonly used high-frequency figure of merit.[7,8]

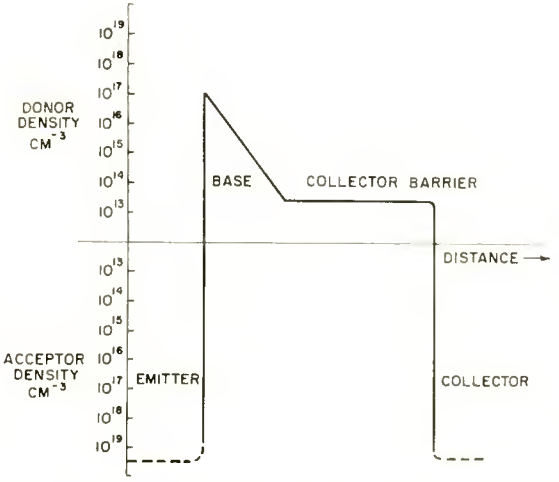

Fig. 1—Impurity distribution for a p-n-p drift transistor.

$$\text{Figure of Merit} = \frac{1}{r_{bb'} C_{b'c} \tau}.$$

The terms $r_{bb'}$ and $C_{b'c}$ in this expression are defined in the hybrid-π equivalent circuit. The term τ is the transit time of the minority carriers in the base.

The "built-in" field provided by the graded impurity density reduces the carrier transit time in the base, τ, considerably as compared to that in a conventional junction transistor in which the current is carried by diffusion. The graded impurity density also provides a high

[7] J. M. Early, "Design Theory of Junction Transistors," *Bell Sys. Tech. Jour.*, Vol. 32, p. 1271, November, 1953.

[8] L. J. Giacoletto, "Study of P-N-P Alloy Junction Transistor From D-C Through Medium Frequencies," *RCA Review*, Vol. XV, p. 506, December, 1954.

average impurity density which tends to make the value of resistance $r_{bb'}$ small. The low average base resistivity has no detrimental effect on the properties of the collector because the capacitance $C_{b'c}$ and the "breakdown" voltage depend primarily on the width of the high-resistivity barrier that separates the collector junction from the active base region.

Construction Techniques

Drift transistors such as the 2N247 having an impurity distribution similar to that shown in Figure 1 have been made by a process combining solid-phase-diffusion and alloy-junction techniques. In this process, the diffusion technique is used to obtain a "skin" of graded n-type impurity on a pellet of high-resistivity (30 to 50 ohm-centimeter) n-type germanium. This skin is then removed from one face of the pellet by acid etching, and a p-type collector junction is alloyed into the etched side. A p-type emitter junction is alloyed into the face

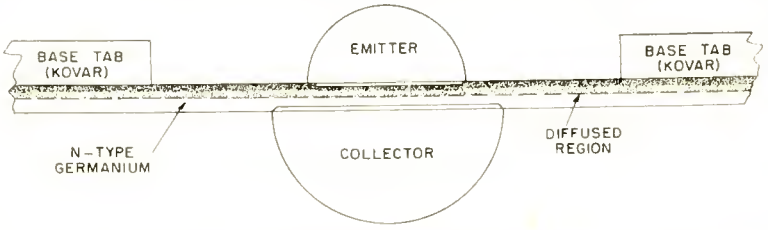

Fig. 2—Cross-sectional view of the drift-transistor structure.

from which the skin of graded n-type impurity was not removed. The structure is completed by a ring-type base tab soldered to the emitter side of the pellet.

A cross-sectional view of this structure is shown in Figure 2. The shading on the emitter side of the germanium pellet indicates the graded impurity region. Important parameters which must be controlled in the construction process are the surface concentration of the diffusing impurity, the impurity distribution in the graded region, and the penetration depth of the alloy junctions.

Diffusion Process

The impurity diffusion is performed in a vacuum furnace having two temperature zones, as shown in Figure 3. The temperature of the first or "source" zone is such that an arsenic vapor pressure of approximately 10^{-3} millimeter of mercury is obtained from a source of pure arsenic. The metal shield in this zone prevents undesirable condensation of the arsenic vapor on the colder portion of the furnace tube. In the

second or "hot" zone, which contains a carbon boat or jig for the germanium pellets, the temperature is adjusted to control the diffusion process.

The impurity concentration at the surface of the crystal pellet is controlled by the vapor pressure of the arsenic, the pellet temperature, and the furnace geometry. For a temperature of 200°C in the source zone and 785°C in the hot zone, the measured* surface concentration is approximately 5×10^{17} per cubic centimeter.

If the surface concentration is assumed to be constant throughout the diffusion period, the impurity distribution in the graded region, $C(x)$, is given by the expression

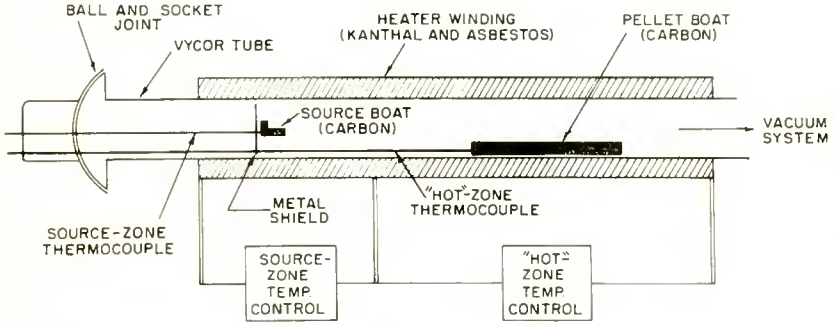

Fig. 3—Sketch of vacuum furnace used for diffusion process.

$$C(x) = C_s \operatorname{erfc} x/2L,$$

where C_s is the surface concentration, x is the distance into the crystal, L is the impurity diffusion length $= (Dt)^{1/2}$, where D is the diffusion constant and t is time, and erfc is the complementary-error function. Because both the surface concentration, C_s and the diffusion constant, D, are functions of the pellet temperature, desired variations in the width of the graded region are made by changing the time of the diffusion process.

After the pellet is diffused, it is imbedded in a coating of Kel F† (200) wax on a glass slide, and the n-type skin is removed from the exposed face by acid etching.

* For this measurement, arsenic is diffused into a crystal having a known acceptor density, and the depth into the crystal at which compensation takes place is determined. Because the diffusion length is known (from the temperature and time of diffusion), the surface concentration can be determined by extrapolation of the assumed complementary-error-function distribution.

† Trademark of the N. W. Kellogg Co., Jersey City, N. J.

Alloying Process

Accurate control of both the area and the depth of penetration of the alloy junctions is obtained by means of the alloying technique described by Mueller and Ditrick.[9] In this technique, the alloy dot is first soldered to the germanium with the aid of a flux at a relatively low temperature (360°C). The soldering insures good wetting, establishes the final area of the junction, and aids in maintaining a flat junction front during the higher-temperature alloying process. After the soldering process, the junction is fired in a hydrogen atmosphere at a temperature determined by the desired depth of penetration. As pointed out by Mueller and Ditrick,[9] the flatness of the junction front with respect to the crystal face depends on the accuracy with which the crystal is aligned with the (111) plane.

Emitter-Junction Design Considerations

The desired penetration of the emitter junction is determined by consideration of the emitter injection efficiency, the magnitude of the field in the base region, and the effect of the emitter transition capacitance, C_{et}, on $f_{\alpha e}$ (the frequency at which the current transfer ratio is 0.707 times the low-frequency value). If, for simplicity, the impurity distribution in the base is assumed to be exponential, the "built-in" field is constant. The strength of this field is equal to the potential change in the base region divided by the width of the base. The base width is defined as the distance between the emitter junction and the edge of the collector depletion layer. Since the potential difference is proportional to the logarithm of the ratio of impurity densities at the edges of the base layer, the field strength is also proportional to this quantity. The field can be increased, therefore, by an increase in the impurity density in the base region adjacent to the emitter. However, because the injection efficiency depends on the ratio of the impurity densities in the emitter and the base region, the density in the base cannot be increased indefinitely without an impairment of injection efficiency. For an alloyed emitter, a good balance between injection efficiency and field strength is reached when the impurity density in the base region adjacent to the emitter is in the range of 5×10^{16} to 10^{17} per cubic centimeter.

The accelerating field in the base reduces the transit time and thereby tends to decrease the capacitance due to storage of minority carriers in the base. However, the high impurity density at the emitter

[9] C. W. Mueller and N. H. Ditrick, "Uniform Planar Alloy Junctions for Germanium Transistors," *Transistors I*, RCA Laboratories, Princeton, N. J., 1956, p. 121.

required to produce this field tends to increase the transition capacitance of the forward-biased emitter diode. The importance of the emitter transition capacitance is illustrated in the simplified common-base equivalent circuit[8] shown in Figure 4. The resistance r_e is shunted by both the storage capacitance, C_s, and the emitter transition capacitance, C_{et}. Because the current through the emitter transition capacitance is a true displacement current, it does not appear either as minority carriers in the base or as collector current. Even if the storage capacitance is neglected, the a-c collector current will be 3 decibels below its low-frequency value when the impedance of the emitter transition capacitance equals the resistance r_e. This condition defines a frequency, f_e, given by

$$f_e = \frac{q I_E}{kT} \frac{1}{2\pi C_{et}},$$

where I_E is the d-c emitter current, q is the electronic charge, k is

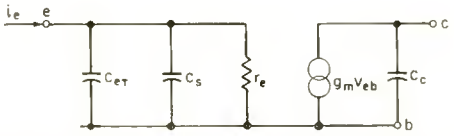

Fig. 4—Simplified common-base equivalent circuit.

Boltzmann's constant, and T is the absolute temperature in degrees Kelvin.

The frequency f_{ace} of the transistor is determined by the parallel combination of the frequency f_e mentioned above and a frequency f_s determined by transit-time effects in the base region:

$$\frac{1}{f_{ace}} = \frac{1}{f_s} + \frac{1}{f_e}.$$

The frequency f_e varies linearly with emitter current provided the emitter transition capacitance does not change appreciably with the applied forward bias. Because f_s is independent of emitter current, f_{ace} should also vary linearly with current for small values of I_E (where $f_e \ll f_s$). Figure 5 shows a curve of f_{ace} as a function of emitter current (with collector-to-base voltage constant) for a developmental drift transistor.

Although some variation of f_{ace} with emitter current occurs in all junction transistors, the relationship is more pronounced in this par-

ticular drift transistor because the emitter and base storage capacitances are of the same order of magnitude. The undesirable effect of the emitter transition capacitance can be minimized by decreasing the emitter area. In the design of a transistor, however, a balance must be reached between the frequency capabilities of the device and the difficulty of construction.

In the alloying of the emitter junction, a dot material having a high injection efficiency[10] is used. A relatively low temperature (450°C) is used to obtain the penetration accuracy necessary to place the

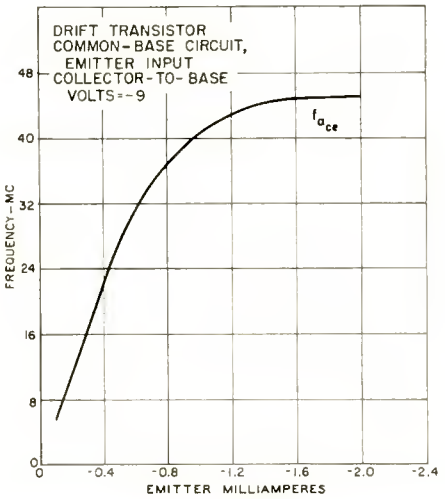

Fig. 5—Curve showing $f_{\alpha ce}$ as a function of emitter current (with collector-to-base voltage constant) for a developmental drift transistor.

junction at the proper impurity level in the rapidly varying graded region. Insufficient penetration results in poor injection efficiency and large emitter transition capacitance. Too great a penetration causes high base resistance (because the average resistivity in the base is increased) and a low collector-to-emitter "punch-through" voltage.

Base-Region Impurity Distribution

Kroemer[5] has shown that the frequency f_s determined by transit-time effects in the base region is given by

---

[10] L. D. Armstrong, C. L. Carlson, and M. Bentivegna, "P-N-P Transistors Using High-Emitter-Efficiency Alloy Materials," *Transistors I*, RCA Laboratories, Princeton, N. J., 1956, p. 144.

$$f_s = \frac{D_p}{\pi W^2}\left(\frac{q\Delta V}{2kT}\right)^{3/2}$$

where D_p is the hole diffusion constant, W is the base width or distance between the emitter junction and the edge of the collector depletion layer, and ΔV is the potential difference determined by the change in base-region impurity concentration between these points. The desired impurity density at the emitter is determined by the considerations discussed previously. The base width and impurity concentration at the edge of the collector depletion layer depend not only on the impurity density gradation but also on the penetration depth of the collector depletion layer into the graded region. An involved iteration process has been developed for calculating the necessary gradation of impurity density to yield a desired value of f_s. However, for the type transistor described, the accuracy of this process is easily approached by an empirical method. In this method, the quantity $(q\Delta V/2kT)^{3/2}$ is assumed to have a value of 4, and a base width for the desired f_s is calculated from the equation above. The impurity change consistent with the assumed value of ΔV is 200. The impurity diffusion length necessary to provide this impurity change in the calculated base width is then obtained directly from the complementary-error function.

Collector-Junction Design Considerations

In the alloying of the collector junction, the depth of penetration must be adjusted so that the width of the collector barrier provides the desired value of capacitance C_c (Figure 4). The width of the high-resistivity region is easily determined by subtracting the width of the graded region from the known pellet thickness. The depth of penetration and the junction area are then adjusted so that the desired capacitance is obtained when the remaining width is substituted for d in the equation

$$C_c = \frac{A\epsilon}{d}$$

where A is the junction area, d is the width of the collector barrier, and ϵ is the dielectric constant of germanium.

In the construction of the collector junction, an In-Zn alloy dot and an alloying temperature of 590°C are used. The pellet thickness and junction area are adjusted as described above to provide the desired capacitance values.

Because wide depletion layers are used to obtain low capacitance, it is necessary to consider the minimum collector-to-base voltage for which the high-frequency characteristics of the device are obtained. This voltage must be large enough to cause the depletion layer to completely penetrate the high-resistivity region so that (1) the transit time through this region is small in comparison to the base transit time, and (2) f_{ace} and the current transfer ratio do not vary appreciably with collector-to-base voltage so that the inherently high output impedance of the drift transistor is realized.

When the resistivity and width of the barrier region are known, the penetration voltage is calculated by means of simple abrupt-junction theory. For minimum transit time, however, the field in the barrier region must be great enough so that the limiting carrier-drift velocity is maintained throughout the region. J. M. Early[6] has shown that this condition requires a minimum field of one volt per micron of depletion-layer thickness and results in a transit time of 2×10^{-11} second per micron. In the developmental drift transistors described here, it has been determined that the field in the collector barrier produced by the minimum voltage necessary to penetrate it is sufficient to make the transit time in the depletion layer negligible with respect to the transit time in the base.

The variation of f_{ace} and output impedance with collector-to-base voltage depends on the rate of change of the base width with collector voltage. This change in base width is caused by the variation in the width of the collector depletion layer with voltage. When the depletion layer terminates in the low-impurity-density barrier region, the variation of width with collector-to-base voltage is large. As the voltage is increased, the depletion layer penetrates the graded region. Because the impurity density increases rapidly in this region, the rate of change of the width of the depletion layer with voltage becomes small. When the variation of base width with voltage is small, f_{ace} does not vary appreciably with voltage and the output impedance is high.

Typical curves of f_{ace} and output impedance as functions of collector voltage for a developmental drift transistor are shown in Figure 6. In the unit measured, the voltage necessary for the depletion layer to penetrate the collector barrier is approximately —2 volts. The data shows the actual starting voltage to be approximately —4 volts.

Calculation of Base Resistance

The calculation of the base resistance for a drift transistor structure such as that shown in Figure 2 is straight-forward.[5] The base resistance consists of the spreading resistance of the base region directly

under the emitter and the extrinsic ring resistance, or resistance of the ring of germanium between the outer edge of the emitter and the base. The spreading resistance, r_s, is given by[7]

$$r_s = \frac{\rho_b}{8\pi W_b}$$

where ρ_b is the average base resistivity and W_b is the base width.

Because the impurity density in the base is graded, the resistivity value is calculated from the average impurity density. A good approximation for average density is obtained by assumption of an exponential distribution. The average density, $\overline{N}$, is then given by

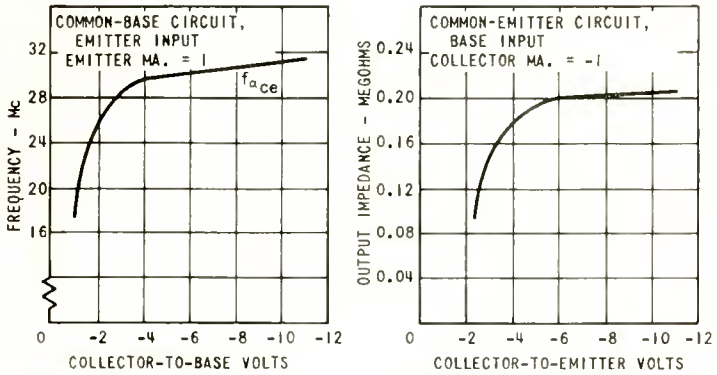

Fig. 6—Curves showing $f_{\alpha ce}$ and output impedance as functions of collector voltage for a 2N247 drift transistor.

$$\overline{N} = (L/W_b)\,(N_c - N_c)$$

where L is the characteristic length of the assumed exponential impurity distribution, W_b is the base width, N_c is the impurity density at the emitter, and N_c is the impurity density at the edge of the collector depletion layer. When the variation of mobility with impurity density is neglected, the average resistivity, ρ_b, is given by

$$\rho_b = \frac{1}{q\,\mu_n\,\overline{N}}$$

where μ_n is the electron mobility. In the developmental units that have been constructed, the average base resistivity is usually of the order of 0.1 ohm-centimeter.

The extrinsic ring resistance, r, is obtained from the equation

$$r = \frac{\rho_b'}{2\pi W'} \ln d_l/d_e$$

where d_l is the diameter of the base tab hole and d_e is the diameter of the emitter. The resistivity ρ_b' in this equation is obtained from the average impurity density in the entire graded region, and the width W_b' is the distance from the pellet surface to the end of the graded region. Because the impurity concentration at the surface is greater than that adjacent to the emitter, ρ_b' is less than ρ_b. W_b' is greater than W_b because the penetration of the emitter junction and collector depletion layer into the graded region need not be considered.

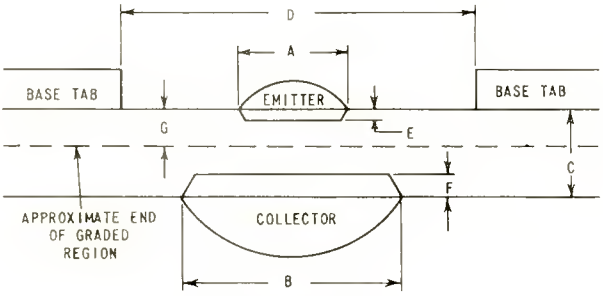

DIMENSION - MILS

TYPE	A	B	C	D	E	F	G
RCA-2N247	10	15	1.8	30	0.2	0.7	0.8
DEVEL. TYPE	6	10	1.1	30	0.1	0.5	0.3
DEVEL. TYPE	3	5	0.75	10	0.08	0.3	0.25

Fig. 7—Dimensions of 2N247 and two developmental drift transistors.

Characteristics of Drift Transistors

The construction techniques and design considerations presented above have been used in the development of the 2N247 drift transistor and in two other developmental units in which the same basic structure is scaled down to improve frequency response. In the developmental units, not only are the junction area and pellet thickness reduced but the diffusion depth and emitter transition capacitance are also decreased, as shown in Figure 7. The impurity diffusion lengths in the 2N247 and the developmental transistors are 0.17, 0.07, and 0.05 mil, respectively. These lengths are the result of arsenic diffusion at 785°C for periods of 3 hours, 30 minutes, and 15 minutes, respectively.

The electrical parameters and power gains obtainable from these devices at various high frequencies are shown in Table I. The power-gain data was measured in a common-emitter unneutralized circuit by the Advanced Development Group of the RCA Victor Television Division at Camden, N. J. Somewhat higher values of gain can be obtained at most frequencies by the use of neutralized circuits.

The 2N247 is an excellent example of the improvement in transistor frequency response that can be achieved by the use of the drift-transistor structure. The high-frequency figure of merit of the 2N247 is an order of magnitude greater than that of conventional alloy-junction transistors, although no appreciable change has been made in the dimensions or processing procedures except for the introduction of a solid-phase impurity diffusion. The results that can be achieved by scaling down the 2N247 structure are indicated by the performance of the developmental types (Table I).

Table I—Electrical Characteristics and Power Gain of Drift Transistors.

	C_c $\mu\mu f$	$r_{bb'}$ Ω	$f_{\alpha ce}$ mc.	f_{max} mc.	10.7 mc. P.G. db*	40 mc. P.G. db†	70 mc. P.G. db‡	noise factor
2N247	1.7	40	30	136	22.5			8 db
Developmental	1.0	< 50	90	225 calc.		14		9 db (45 mc)
Developmental	0.5	< 100	125	400 calc.			14	7 db (70 mc)

* Measured at $V_c = -9$ volts, $I_e = 1$ milliampere.
† Measured at $V_c = -15$ volts, $I_e = 2$ milliamperes.
‡ Measured at $V_c = -15$ volts, $I_e = 1.5$ milliamperes.

VALIDITY OF TRAVELING-WAVE-TUBE NOISE THEORY

By

R. C. Knechtli* and W. R. Beam†

Summary—*This paper presents and discusses the results of a series of experiments designed to investigate the validity of the first-order theory of noise in traveling-wave tubes, and to indicate its limitations. Higher-order effects, also revealed by these experiments, are discussed elsewhere. Making proper allowance for these effects, good agreement between first-order theory and experiment has been established.*

A further purpose of the present measurements was to determine the correlation between beam current and electron velocity fluctuations at the potential minimum in front of the cathode. This correlation was found to be zero within the accuracy of the measurement.

Introduction

ALTHOUGH a consistent first-order theory of noise in traveling-wave tubes has existed for some time,[1-5] no proper experimental verification has, to the authors' knowledge, been described. The purpose of this paper is to present and discuss the results of a series of experiments designed to investigate the validity of this theory and to indicate its limitations. These experiments also bring out the importance of various higher-order effects not predicted by the first-order theory. (These effects are now basically understood and are described elsewhere.[6,7]) However, no attempt was made to measure noise-current smoothing at the potential minimum,[8,9] nor to observe noise figure reduction due to higher-order modes.[10]

---

* RCA Laboratories, Princeton, N. J.

† RCA Tube Division, Princeton, N. J.

[1] D. A. Watkins, "Traveling-Wave Tube Noise Figure," *Proc. I.R.E.*, Vol. 40, p. 65, January, 1952.

[2] S. Bloom and R. W. Peter, "A Minimum Noise Figure for the Traveling-Wave Tube," *RCA Review*, Vol. XV, p. 252, June, 1954.

[3] J. R. Pierce and W. E. Danielson, "Minimum Noise Figure of Traveling-Wave Tubes with Uniform Helices," *Jour. Appl. Phys.*, Vol. 25, p. 1163, September, 1954.

[4] H. A. Haus and F. N. H. Robinson, "The Minimum Noise Figure of Traveling-Wave Amplifiers," *Proc. I.R.E.*, Vol. 43, p. 981, August, 1955.

[5] S. Bloom, "The Effect of Initial Noise Current and Velocity Correlation on the Noise Figure of Traveling-Wave Tubes," *RCA Review*, Vol. XVI, p. 179, June, 1955.

[6] W. R. Beam, "Noise Wave Excitation at the Cathode of a Microwave Beam Amplifier," to be published in *Trans. I.R.E. PGED*, July, 1957.

[7] R. C. Knechtli, "Increase of Electron Beam Noise in Velocity Jumps," presented at the Electron Tube Research Conference, Boulder, Colo., June, 1956.

Theoretical Relations

The Bloom and Peter theory[2] is representative. Noise introduced in the electron beam at the cathode (or the potential minimum) is transformed by the accelerating and drift regions following in the electron gun. In a drift region, for example, the noise current and noise velocity should, according to the first-order theory, follow a regular standing-wave pattern. In an accelerating region, the noise current and velocity are not periodic functions of distance, but it has been shown[4] that the space-charge waves have important conservation properties.

The physically most pleasing model of the space-charge wave transformation in the electron gun and drift regions is the transmission-line analogue of Bloom and Peter.[11] The conservation rules for the space-charge waves on an electron beam are the same as for power on a transmission line, and a "characteristic impedance" W may be defined[9] as follows for the electron beam:

$$W = 2\frac{V_0}{I_0} \cdot \frac{\omega_p}{\omega} \tag{1}$$

where $V_0 =$ d-c beam potential,

$I_0 =$ d-c beam current,

$\omega_p =$ reduced plasma frequency,[1]

$\omega =$ signal frequency.

In a first-order approximation taking only a single space-charge wave into account, the r-m-s noise current, I, in a drift space of constant potential and transverse dimensions varies periodically along the beam between a minimum value I_{min} and a maximum value I_{max}; the variation of I^2 with distance along the beam is sinusoidal and of spatial period equal to $\lambda_p/2$ where λ_p is the plasma wavelength, $2\pi v/\omega_p$, and v is electron velocity.

---

[8] D. A. Watkins, "Noise at the Potential Minimum in the High-Frequency Diode," *Jour. Appl. Phys.*, Vol. 26, p. 622, May, 1955.

[9] P. K. Tien and J. Moshman, "Monte Carlo Calculation of Noise Near the Potential Minimum of a High-Frequency Diode," *Jour. Appl. Phys.*, Vol. 27, p. 1067, September, 1956.

[10] W. R. Beam, "Reduction of Traveling-Wave Tube Noise Figure Including Higher Order Mode Effects," presented at the Electron Tube Research Conference, Boulder, Colo., June, 1956.

[11] S. Bloom and R. W. Peter, "Transmission-Line Analog of a Modulated Electron Beam," *RCA Review*, Vol. XV, p. 95, March, 1954.

According to the first-order theory, the noise figure, F, of a traveling-wave tube also varies periodically with distance, with a spatial period equal to $\lambda_p/2$, as the input end of the helix is moved axially along the beam. When the helix is moved, the minimum noise figure, $F_{\min}$, is obtained for a definite distance l_{opt} between noise-current minimum and helix input, and the maximum noise figure, $F_{\max}$, is obtained for positions $\lambda_p/4$ away from this optimum helix input position. F is also a function of the noise-current standing-wave ratio (SWR), η, at the helix input; l_{opt}, however, is independent of η.

The first-order theory predicts the following relations between noise figure and noise current:

$$F_{\min} - 1 = \frac{W I_{\max} I_{\min}}{kT\Delta f}(1-\nu)\sqrt{4QCf_a f_i \cdot \frac{\eta^2 + \eta^2_{\text{opt}}}{2\eta\eta_{\text{opt}}}}, \qquad (2)$$

$$F_{\max} - 1 = \frac{W I_{\max} I_{\min}}{kT\Delta f}(1-\nu)\sqrt{4QCf_a f_i \cdot \frac{1 + \eta^2\eta^2_{\text{opt}}}{2\eta\eta_{\text{opt}}}}, \qquad (3)$$

where W is the characteristic beam impedance[6] defined in Equation (1). $I_{\max}$ and $I_{\min}$ are the noise-current maximum and minimum in the drift space preceding the helix. Q and C are Pierce's[12] space-charge and gain parameters, respectively. The other quantities appearing in Equations (2) and (3) are

k = Boltzmann's constant,

T = ambient temperature in °K,

Δf = bandwidth over which the noise current, I, is measured (the usual definition of noise theory),

$$\nu = \frac{P_R(a)}{W I_{\max} I_{\min}},$$

$P_R(a)$ = real part of the noise power at the potential minimum, as defined by Bloom,[5]

f_a, f_i = maximum and minimum value respectively, of Watkin's "f" function,[1,5]

η_{opt} = optimum value of the noise current SWR, η, corresponding to the smallest value of $F_{\min}$.

[12] J. R. Pierce, *Traveling-Wave Tubes*, D. Van Nostrand, New York, New York, 1950.

The quantities $\sqrt{4QCf_nf_i}$ and η_{opt} are readily found as functions of QC and of Pierce's helix-loss parameter, d. The parameterization of formulas and the curves published by Bloom[5] are particularly well suited to this purpose. The quantity ν is a measure of the correlation between beam current and electron velocity fluctuations at the potential minimum. It varies between -1 at full negative correlation and $+1$ at full positive correlation, and is zero in the absence of correlation; ν also is identical to π/S, the ratio of the invariant real part π of the cross power density spectrum to the invariant S, both defined by Haus.[13]

The value of l_{opt} (optimum helix position) predicted by the first-order theory is given by

$$\psi_{opt} = \frac{l_{opt}}{\lambda_p} \cdot 2\pi,$$

where (4)

$$\psi_{opt} = \frac{1}{2}(\pi - \gamma),$$

$$\lambda_p = \text{plasma wavelength},$$

γ is a function of QC and d only, and has been defined by Bloom and Peter.[2] ψ_{opt} as defined by Equation (4) also is given directly as a function of QC and d by Bloom's curves.[5] One observes that ψ_{opt} is independent of the noise current SWR, η, and of the correlation parameter, ν.

Description of Measurements

The purpose of the measurements to be described was to establish the validity and any practical limitations of the theoretical relations, Equations (2), (3), (4), and to determine the experimental value of the correlation parameter ν appearing in Equations (2) and (3). For this purpose, the beam noise current, I, had to be measured in a drift region as a function of axial position. The noise figure, F, corresponding to this noise current had also to be measured as a function of helix position along the axis of the beam. This could only be done by performing noise current and noise figure measurements on the same beam, keeping the conditions of measurement (gun parameters, beam current and electrode potentials) unchanged throughout each set of measurements.

---

[13] H. A. Haus, "Noise in One-Dimensional Electron Beams," *Jour. Appl. Phys.*, Vol. 26, p. 560, May, 1955.

The noise current was measured by means of a resonant cavity, loosely coupled to the beam, and movable along the beam axis. The noise figure was measured on a traveling-wave amplifier consisting of this same beam and a movable helix assembly. The whole assembly is schematically sketched in Figure 1. For mechanical convenience, the cavity and helix move together as a single unit (constant spacing between cavity gap and helix input end). To prevent any effect of the cavity on the helix noise figure measurements, the latter were performed at a frequency differing by about 100 megacycles (at 3,000 megacycles) from the resonant frequency of the cavity. The beam is launched from a conventional three-region low-noise gun sketched in

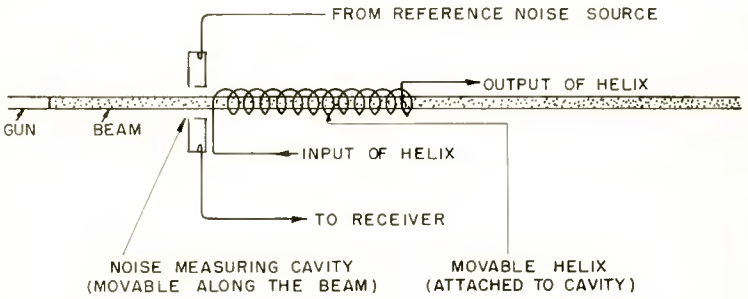

Fig. 1—Noise current and noise figure measuring assembly.

Figure 2. The details of the measuring apparatus and the method of measurement are described elsewhere.[14]

In Equations (2) and (3), F_{min} and F_{max} are given as functions of the beam "noisiness" $W\,I_{max}\,I_{min}$, of ν, and of the noise current SWR, η. According to the first-order theory, the noisiness, for given d-c beam current and cathode temperature, should be constant and independent of η. It was found, however, that the noisiness varied with the gun potentials and, therefore, with η. These effects are not predictable by the first-order theory. They are mainly caused by the effects[7] produced by potential discontinuities in the gun. In addition, the theoretical value of noisiness predicted by assuming Rack velocity[15] and full shot noise at the potential minimum also was found to be incorrect as a consequence of higher-order effects.[6,7] Under these conditions, all that

[14] W. R. Beam and R. C. Knechtli, "High Precision Demountable Electron Beam Noise Measuring Apparatus," presented at the Congres Tubes Hyperfrequence, Paris, France, May, 1956.

[15] A. J. Rack, "Effect of Space Charge and Transit Time on Shot Noise in Diodes," *Bell Sys. Tech. Jour.*, Vol. 17, p. 592, 1938.

the first-order theory can predict is the noise figure corresponding to the measured noisiness and the unknown ν. This suggests the following program of measurements:

1. measurement of the beam noisiness,
2. measurement of noise current SWR, η,
3. measurement of the corresponding values of $F_{\min}$ and $F_{\max}$,
4. comparison of both sets of measurements with Equations (2), (3), and (4), finding the value of ν for which the experimental data fits the theoretical relations of Equations (2) and (3).

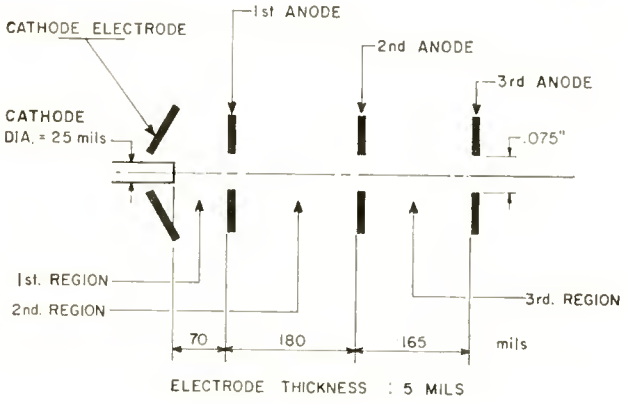

Fig. 2—Three-region low-noise gun.

Several such series of measurements were performed, all leading to similar results. Figure 3 shows one set of noise current measurements; the ordinate Y is a measure of the beam noise current and is defined by

$$Y = 10 \log \frac{I^2}{I^2_{sh}} \tag{5}$$

where $I^2 =$ mean square beam noise current,

$I^2_{sh} = 2eI_0\Delta f =$ mean square shot noise current corresponding to the d-c beam current I_0.

The abscissa z represents the distance along the beam, referred to an arbitrary fixed plane, $z = 0$, located approximately 1.7 inches from the third anode of the gun. Throughout the entire series of measurements,

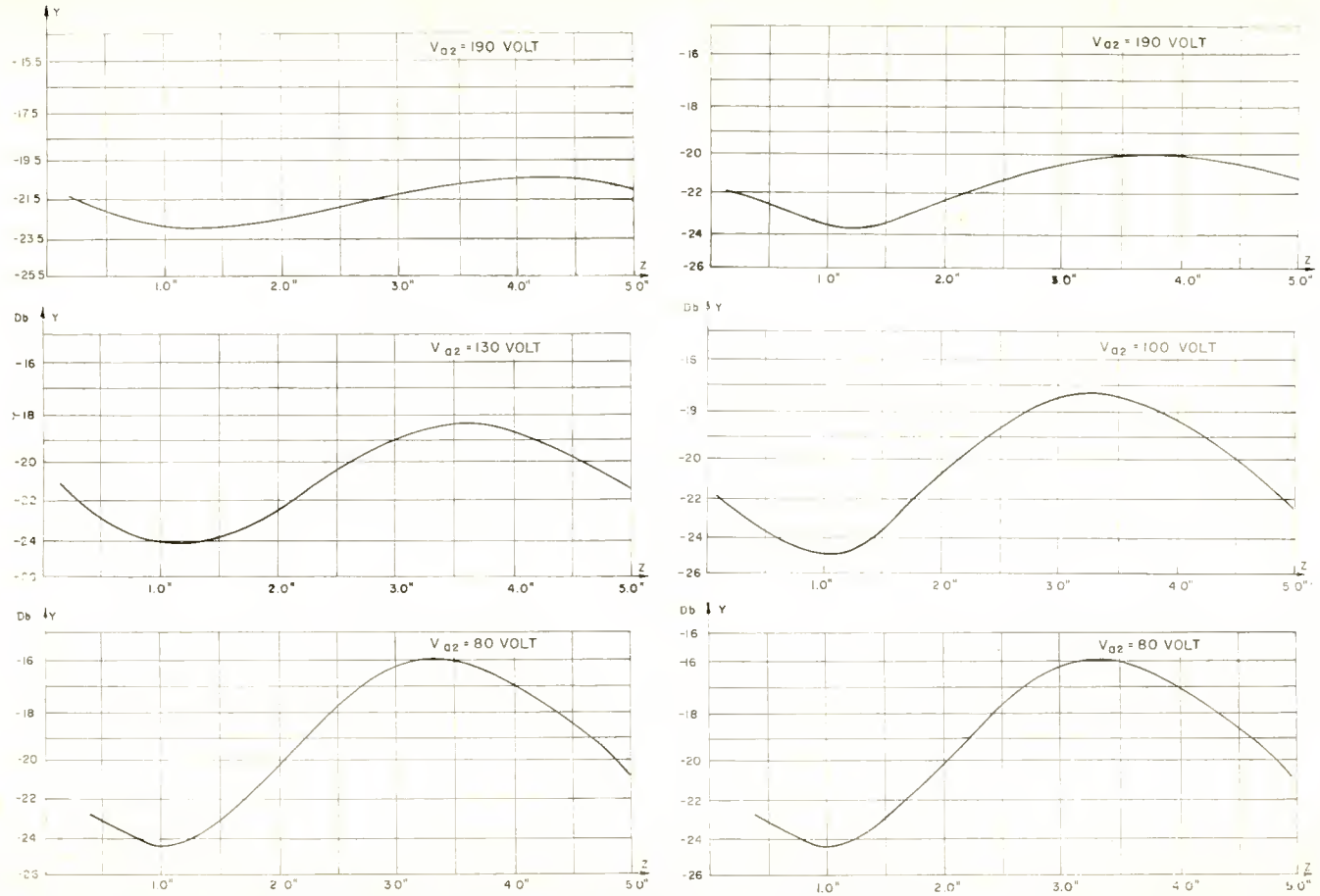

Fig. 3—Noise current measurements: $Y = 10 \log (I^2/I^2_{\text{shot}})$ (db above shot noise), I = beam noise current, Z = distance from reference plane, $V_{a1} = 50$ volts, $V_{a3} = 500$ volts, $I_{\text{beam}} = 300$ microamperes, $V_{\text{drift}} = 650$ volts, $B = 825$ gausses.

the d-c beam current, I_0, was held constant at 300 microamperes, and the d-c beam potential, V_0, in the drift space following the gun, was held constant at 650 volts. The noise current SWR, η, was changed from one run to the next by changing the second-anode potential of the gun, keeping the d-c beam current constant by appropriate (small) changes of cathode electrode potential. First- and third-anode potentials were held constant with $V_{a1} = 50$ volts and $V_{a3} = 500$ volts. The confining magnetic field used to focus the beam corresponded to $B = 825$ gausses. The resonant frequency of the noise-measuring cavity was 3,000 megacycles. The results of the measurements of Figure 3 are summarized more meaningfully in Figures 5 and 6. One observes that Figure 5 is consistent with the analogy between transmission-line transformers and multi-region low-noise guns,[16] while Figure 6 shows the importance of lens effects[7] on noisiness.*

The set of noise figure measurements under conditions corresponding to those of the noise current measurements of Figure 3 is shown in Figure 4. On the curves of Figure 4, the ordinate is the noise figure, F, expressed in decibels. The abscissa, z, is the distance between the input end of the helix and the same fixed reference plane ($z = 0$) defined above. The curves of Figures 3 and 4 are arranged so that the noise-current measurements of Figure 3 correspond to the noise-figure measurements of Figure 4. F was measured at the helix potential corresponding to maximum gain, which was again $V_0 = 650$ volts.

Evaluation of the Measurements

To facilitate the comparison of the theoretical relations, Equations (2) to (4), with the measurements of Figures 3 and 4, it is convenient to define a quantity N which is proportional to the beam noisiness as follows:

$$N = \frac{I_{max} I_{min}}{I^2_{sh}}. \tag{6a}$$

One observes that since W and I^2_{sh} are constant throughout the whole

[16] R. C. Knechtli and W. R. Beam, "Performance and Design of Low-Noise Guns for Traveling-Wave Tubes," *RCA Review*, Vol. XVII, p. 410, September, 1956.

* It should be mentioned that similar measurements of noise current have been performed at M.I.T., prior to this work, by Smullin and Fried; however, no corresponding measurements of noise figure were made.

$$\frac{W I_{max} I_{min}}{kT\Delta f} = 4 \frac{\lambda_e}{\lambda_p} \cdot \frac{eV_0}{kT} \cdot N, \tag{7}$$

where $\lambda_e = \frac{v}{f}$ = electronic wavelength,

v = electron velocity,

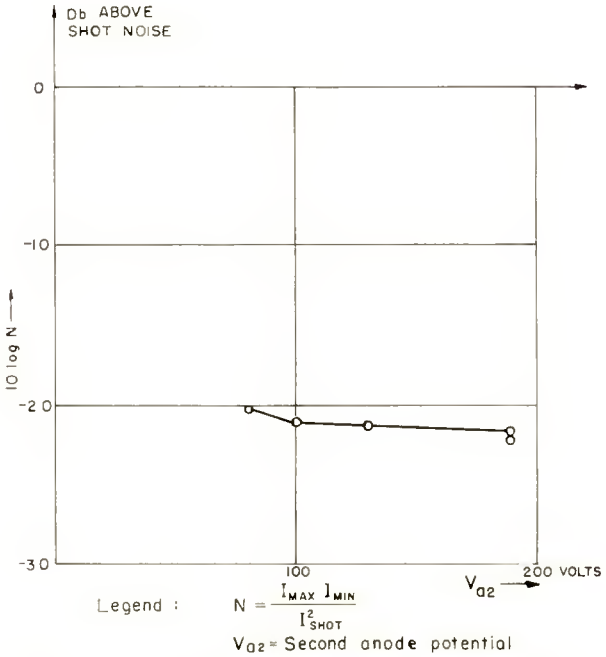

Fig. 6—Noiseness versus second-anode potential.

f = signal frequency,

$\lambda_p = 2\pi \frac{v}{\omega_p}$ = plasma wavelength,

ω_p = reduced plasma frequency,

e = charge of the electron,

k = Boltzmann's constant,

T = absolute temperature (°K),

V_0 = d-c beam potential with respect to cathode, in the drift region, including the helix region.

Equations (2) and (3) now can be rewritten in a form better suited to experimental verification;

$$\frac{F_{\min}-1}{N}=4\frac{\lambda_c}{\lambda_p}\cdot\frac{eV_0}{kT}\sqrt{4QCf_af_i\cdot\frac{\eta^2+\eta^2_{\text{opt}}}{2\eta\eta_{\text{opt}}}}, \tag{2a}$$

$$\frac{F_{\max}-1}{N}=4\frac{\lambda_c}{\lambda_p}\cdot\frac{eV_0}{kT}\sqrt{4QCf_af_i\cdot\frac{1+\eta^2\eta^2_{\text{opt}}}{2\eta\eta_{\text{opt}}}}. \tag{3a}$$

From cold tests it was found that the helix used in these measurements had $d \cong 0.2$. From gain measurements, $QC = 0.17$. For these values of QC and d one has:[5]

$$\sqrt{4QCf_af_i}=0.66,$$

$$\eta_{\text{opt}}=2.$$

From the noise-current measurements of Figure 3, one finds for the plasma wavelength an average value of

$$\lambda_p=240 \text{ millimeters.}$$

The other numerical values from the measurements, to be introduced into Equations (2a) and (3a), are

$$V_0=650 \text{ volts},$$

$$\lambda_c=5.05 \text{ millimeters},$$

$$e/kT=39\ V^{-1} \text{ (corresponding to 25°C room temperature)}.$$

Under these conditions, the theoretical values of $(F_{\min}-1)/N$ and $(F_{\max}-1)/N$ predicted by Equations (2a) and (3a) are represented for the case $\nu=0$ (no correlation) by the theoretical curves shown in Figure 7.

In order to compare the theoretical curves of Figure 7 with the measurements of Figures 3 and 4, the experimental values of $F_{\max}$, $F_{\min}$, N, and η must be found from the data of Figures 3 and 4. At this point, one observes that the noise current and noise figure curves are not perfectly periodic with distance; as a consequence of higher-order modes,[10] a slight increase with distance was found to be added to the sinusoidal variation of these quantities. Inspection of the experimental curves indicates this increase to be rather linear, at least over

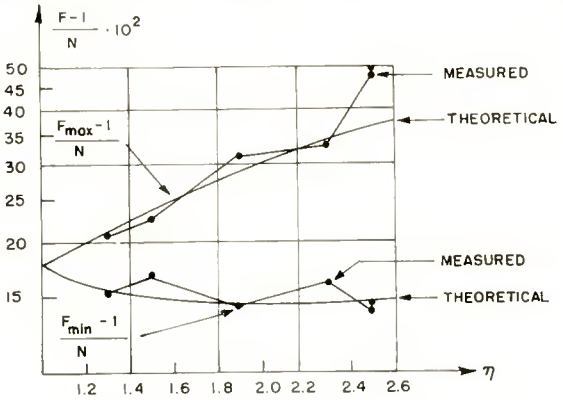

Fig. 7—Noise figure "F" versus noise current SWR, η.

the distances considered. A reasonable means of adjusting the data is as follows:

Let ΔF be the increase of noise figure over a half plasma wavelength (in the absence of higher order effects, $\Delta F = 0$). Let F be the noise figure measured at a plane z; the value of F reduced to the plane z_0 is

$$F_r = F - \Delta F \cdot \frac{z - z_0}{\lambda_{p/2}}. \tag{8}$$

One may notice that ΔF, in all measurements described here, is much smaller than F.

By means of Equation (8), the corrected experimental values of $F_{\max}$ and $F_{\min}$ corresponding to the noise current measurements of Figure 3 are found from the measurements of Figure 4. The reference plane, z_0, is chosen as $z_0 = 1.5$ inches.

The values of $I_{\max}$ and $I_{\min}$ corresponding to the noise current measurements of Figure 3 are reduced in the same manner to the same plane, $z_0 = 1.5$ inches, for the determination of N and of η. By combining the data so obtained from the measurements of Figures 3 and 4, the experimental values of $F_{\max}$, $F_{\min}$, N, and η are found. Thus one obtains the measured values of $(F_{\max} - 1)/N$ and $(F_{\min} - 1)/N$ as functions of η. These are shown as points joined by straight lines on Figure 7.

The theoretical and experimental values of ψ_{opt} may also be compared. The theoretical value of ψ_{opt} given by Equation (4) is found,[5] for the conditions of measurement $QC = 0.17$, $d = 0.2$, to be

$$\psi_{opt} = 34°.$$

This is represented as a horizontal line in Figure 8. The experimental points corresponding to the measurements of Figures 4 and 3 are also shown in Figure 8.

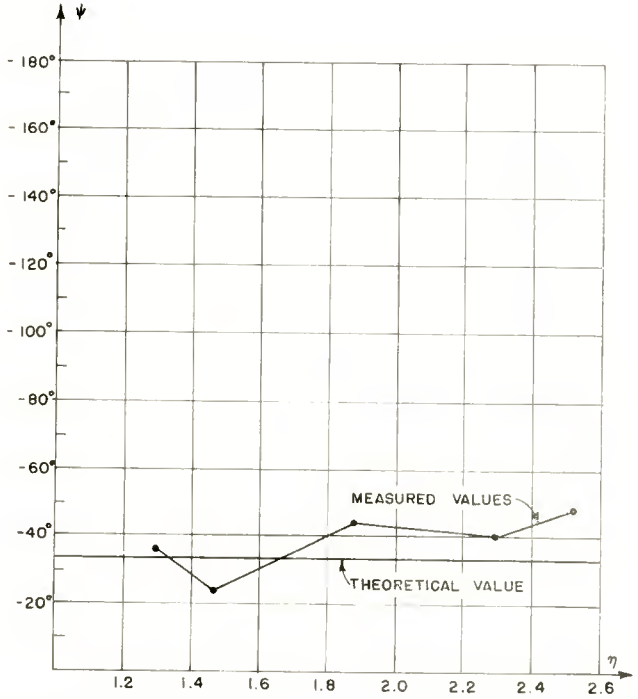

Fig. 8—Optimum helix position versus noise current SWR (ψ_{opt} versus η).

Inspection of Figures 7 and 8 shows that, subject to the corrections described, the first-order theory predicts successfully the relation between noise figure and noisiness (mean beam noise current). Since best fitting between experimental data and theoretical curve was obtained for $\nu = 0$, these measurements also indicate that there was no correlation observable within the limits of measuring accuracy. Taking the limitations of the experimental apparatus into account, this means that, at any rate, $|\nu| \leqslant 0.25$; most probably, actually, one may say that $|\nu| \leqslant 0.1$.*

* The method of "measuring" correlation employed here is probably more meaningful than previous measurements, for it is not from a single measurement, but an entire series of measurements, each one of which adds more weight to our conclusions.

Inspection of Figure 8 shows that the mean square difference between theoretical and measured value of ψ_{opt} (optimum helix positions) is smaller than 10°. This corresponds to a physical distance of 6 millimeters and lies within the probable error of measurement of the position of the minima of the experimental curves.

Conclusions

The noise current and noise figure measurements reported in this paper show that, to a good approximation, the first-order theory of noise in traveling-wave tubes predicts correctly the relation between beam noise current and traveling wave tube noise figure. The noise figure optimization procedure prescribed by the first-order theory is justified by these measurements. Finally, correlation has been established to be immeasurably small, at least for the conditions under which the measurements were performed.

THE DESIGN OF PERIODIC PERMANENT MAGNETS FOR FOCUSING OF ELECTRON BEAMS†

By

F. Sterzer and W. W. Siekanowicz

RCA Tube Division,
Princeton, N. J.

Summary—*In recent papers, Mendel,[1] Pierce,[2] Clogston and Heffner,[3] and Chang[4] have described the focusing of long electron beams by means of permanent magnets producing periodic magnetic fields. Periodic permanent magnets weigh substantially less than both solenoids and permanent magnets producing uniform fields. They also eliminate other problems associated with solenoids, such as power supply, and, in some cases, provision of air or water cooling.*

Previous work on the design of periodic permanent-magnet focusing structures and on the theory of focusing with periodic magnets has been described by Chang.[4,5] This paper extends the theory by consideration of an additional flux path representing the leakage flux between the hubs of the metal shims. The method of analysis is based on the familiar concept of "permeances" of the various flux paths, and results are presented in a manner which facilitates rapid numerical calculation. Design charts for minimum-weight structures are given, and the design of a periodic focusing structure for a specific traveling-wave power amplifier tube is considered in detail.

Calculation of Periodic Focusing Field Requirements From Electron Beam Characteristics

A diagram of a permanent-magnet structure producing a periodic magnetic field is shown in Figure 1. This structure is an assembly of individual ring-shaped magnets, separated by magnetic shims. The ring magnets are axially magnetized, and are

† The work upon which this paper is based was performed for the U. S. Air Force under Contract No. AF33(600)-24400, sponsored by the Wright Air Development Center, Dayton, Ohio.

[1] J. T. Mendel, C. F. Quate, and W. H. Yocum, "Electron Beam Focusing with Periodic Permanent Magnet Fields," *Proc. I.R.E.*, Vol. 42, p. 800, May, 1954.

[2] J. R. Pierce, "Spatially Alternating Magnetic Fields for Focusing Low-Voltage Electron Beams," *Jour. Appl. Phys.*, Vol. 24, p. 1247, September, 1953.

[3] A. M. Clogston and H. Heffner, "Focusing of an Electron Beam by Periodic Fields," *Jour. Appl. Phys.*, Vol. 25, p. 436, April, 1954.

[4] K. K. N. Chang, "Beam Focusing by Periodic and Complementary Fields," *Proc. I.R.E.*, Vol. 43, p. 62, January, 1955.

[5] K. K. N. Chang, "Optimum Design of Periodic Magnet Structures for Electron Beam Focusing," *RCA Review*, Vol. XVI, p. 65, March, 1955.

assembled with faces having the same polarity adjacent. The shims are made of a high-permeability metal, and are used to obtain low-permeance flux paths between the ring magnets and the axis of the magnetic structure. As shown in Figure 1, the variation of the axial component of the magnetic field on the axis of the structure is very nearly sinusoidal.

When purely magnetic means are used for focusing, the required periodic focusing field is a minimum if the beam is launched from a magnetically shielded cathode, larger if it is launched from a partially shielded cathode, and a maximum if the cathode is completely immersed in a magnetic field. Only focusing structures for beams produced by magnetically shielded cathodes are considered in this paper.

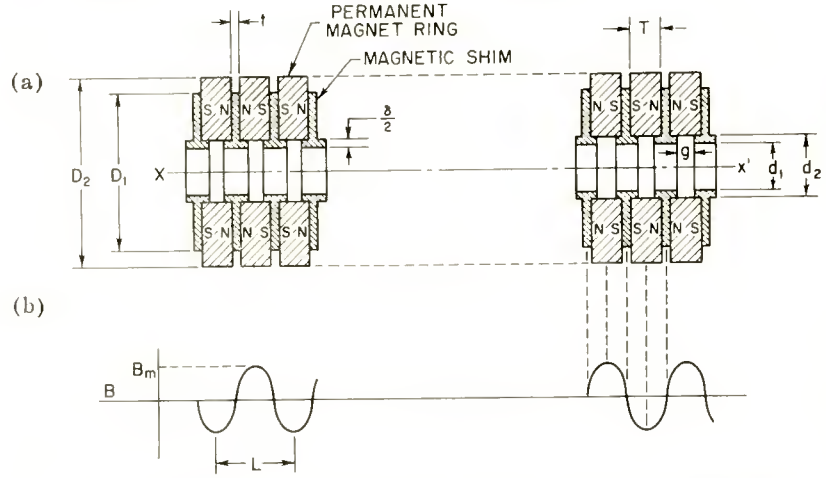

Fig. 1—(a) Diagram of periodic permanent-magnet focusing structure, (b) Plot of axial magnetic-field intensity.

For stable focusing of an electron beam, the period and amplitude of a periodic magnetic field must satisfy certain conditions.[1,6] For a magnetically shielded cathode, the allowable values of the period, L, in inches can be calculated from the expression

$$L = C\frac{V^{\frac{1}{2}}}{B_m}, \tag{1}$$

where V is the beam voltage in volts, B_m is the peak amplitude of the axial magnetic field in gausses, and C is a constant such that

[6] K. K. N. Chang, "On the Stability of Periodic-Field Beam Focusing," *Jour. Appl. Phys.*, December, 1956.

$0 < C < 15.3$ (first pass band).[6] It can be shown theoretically that higher pass bands exist (higher values of C), but their practical value appears limited at present.[1,6]

The use of a periodic focusing field causes a corresponding variation in the diameter of the electron beam. Because this variation, called "scalloping," adversely affects both the r-f and d-c performance of beam-type amplifiers such as traveling-wave tubes, it is desirable that it be kept as small as possible. Theoretical considerations indicate that at a given period length, L, the amplitude of the scalloping is a minimum if the peak magnetic field is given by

$$B_m \text{ (gausses)} = \frac{461\, I^{\frac{1}{2}}}{V^{\frac{1}{4}}\, a}, \tag{2}$$

where I is the beam current in amperes, and a is the average radius of the electron beam in inches. In practice, focusing fields having approximately 1.5 to 2 times the theoretical value indicated in Equation (2) are required.[1] Furthermore, the degree of beam scalloping is reduced as the period of the magnetic field is made smaller.

Given beam voltage, current, and radius, the designer can estimate the field amplitude and period required for stable transmission. The problem then reduces to the design of a magnetic structure which will provide a field having the desired characteristics.

Calculation of The Magnetic Field Produced By A Periodic Structure

As discussed in the Appendix, the maximum field on the axis of an infinitely long magnetic structure of the type shown in Figure 1 is given by

$$B_m = \frac{H_d T}{g} \sum_{n=1}^{\infty} \frac{1}{n} f_1\left(\frac{n d_1}{L}\right) \sin\left(\frac{n\pi g}{L}\right), \tag{3}$$

$$n = 1, 3, 5, 7 \ldots .$$

where T, g, d_1, and L are dimensions shown in Figure 1, and H_d is the magnetic intensity, in oersteds, of the magnetic material used. The function $f_1(nd_1/L)$ versus nd_1/L is plotted in Figure 2. Equation (3) was derived (see Appendix) for the case $D_2 = D_1$ (Figure 1), and on the assumption that the shims are not saturated. For most practical structures the series in Equation (3) converges very rapidly, and it will be sufficient to evaluate only the term for $n = 1$.

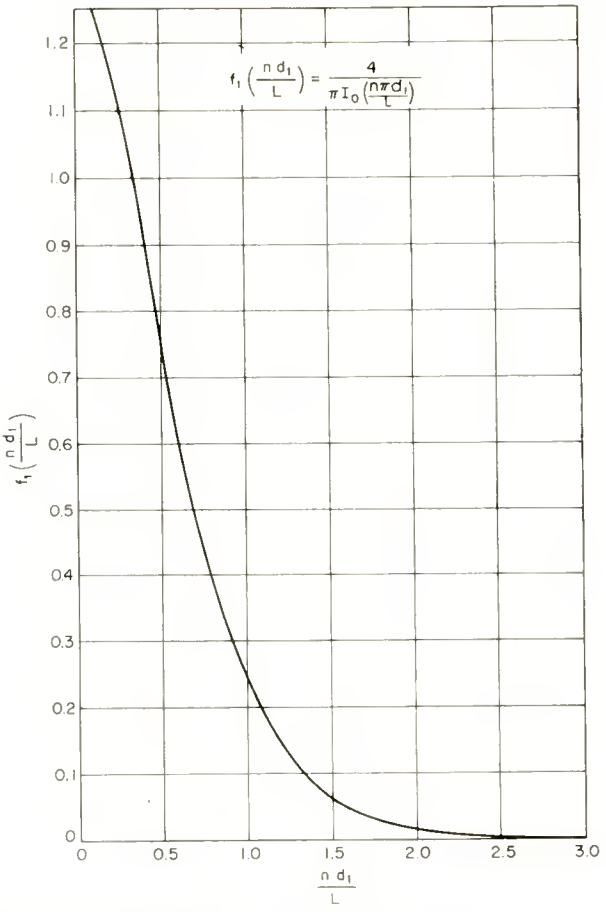

Fig. 2—Plot of $f_1(nd_1/L)$ versus (nd_1/L) as used in Equation (3).

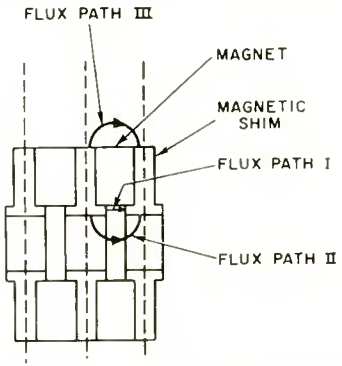

Fig. 3—Manner in which external magnetic circuit is divided into three flux paths for calculation of total permeance.

In order to determine the value of H_d in Equation (3), it is first necessary to evaluate the total permeance, P_T, of the magnetic circuit external to one of the ring magnets.[7] To simplify this evaluation the external magnetic circuit has been divided into three flux paths, as shown in Figure 3. The flux path I, which was not included in previous analyses,[5] represents the leakage flux between the hubs of the shims. The total permeance* (in inches) is

$$P_T = P_1 + P_2 + P_3, \tag{4}$$

where P_1 is the permeance of path I, and is given by

$$P_1 = \frac{0.785\ (d_2^2 - d_1^2)}{g}. \tag{5}$$

P_2 is the permeance of path II, and is given by

$$P_2 = \sum_{n=1}^{\infty} \frac{Ld_1}{n^2 g} f_2\left(\frac{nd_1}{L}\right) \sin\left(\frac{n\pi g}{L}\right), \tag{6}$$
$$n = 1, 3, 5, 7 \ldots .$$

and P_3 is the permeance of path III, and is given by

$$P_3 = \sum_{n=1}^{\infty} \frac{LD_2}{Tn^2} f_3\left(\frac{nD_2}{L}\right) \sin\left(\frac{n\pi T}{L}\right). \tag{7}$$
$$n = 1, 3, 5, 7 \ldots .$$

The functions $f_2(nd_1/L)$ versus nd_1/L, and $f_3(nD_2/L)$ versus nD_2/L are plotted in Figures 4 and 5 respectively. Again, in many practical cases it will be sufficient to calculate only the first term ($n = 1$) in Equations (6) and (7).

From the Appendix

$$-\frac{B_d}{H_d} = \frac{T}{A'} P_T, \tag{8}$$

[7] H. C. Roters, *Electromagnetic Devices*, John Wiley and Sons, New York, N. Y., 1941.

* The units used throughout this paper are gausses, oersteds, and inches. In this system of units the permeability is dimensionless; it follows from the definition of permeance ($P = \mu A/l$) that permeance has the dimensions of length (inches).

where B_d is the flux density in the magnet, $T = L/2 - t$, and A' is the cross-sectional area of the magnet and is equal to $(\pi/4)(D_2^2 - d_2^2)$.

A straight line having a slope $-TP_T/A'$ drawn through the origin of the demagnetization characteristics (B_d versus H_d) of the magnetic material used will intersect the demagnetization curve at the operating point and give H_d. When the air gap, g, is zero, the permeance P_1 is

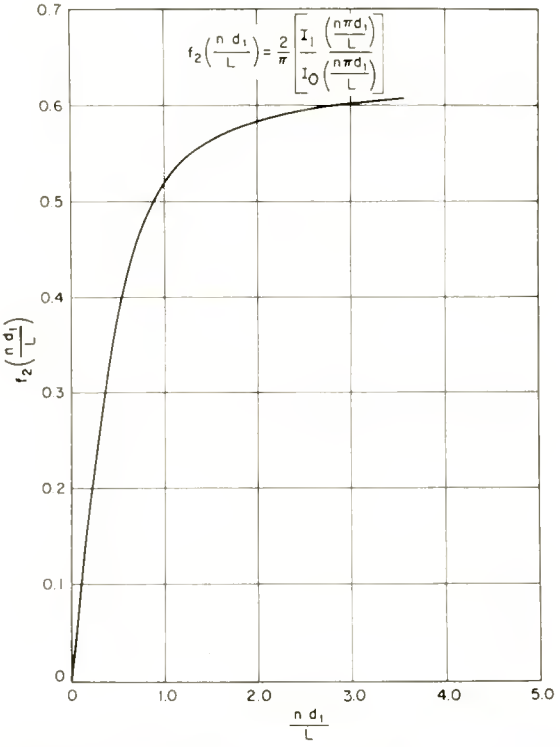

Fig. 4—Plot of $f_2(nd_1/L)$ versus (nd_1/L) as used in Equation (6).

infinite, i.e., the magnet is short-circuited and $H_d = 0$ according to Equation (8), as B_d is finite.

A sample calculation using these equations is given later.

Magnetic Materials Suitable for Periodic Structures

The type of magnetic material most suitable for use in a particular periodic permanent magnet will depend on the amplitude and period requirements of the focusing field. Once these requirements have been estimated, and the inside geometry (d_1, T, and g) fixed, the required

value of H_d can be calculated from Equation (3). Procedures for determining d_1, T, and g are given later. When the value of H_d is known, the required peak field can be obtained in a structure of minimum volume by the use of the magnetic material producing the greatest flux density at this magnetizing force.

Demagnetization and energy product curves for various magnetic materials are shown in Figure 6. Some of the properties of these materials are given in Table I. It can be seen that while the energy

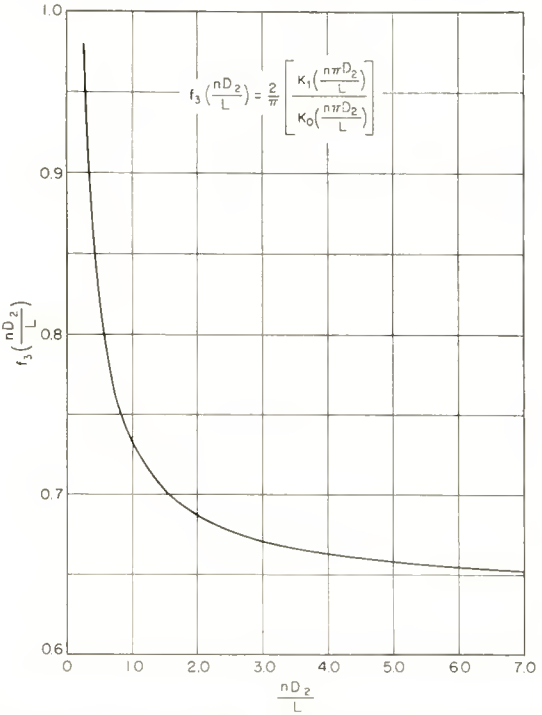

Fig. 5—Plot of $f_3(nD_2/L)$ versus (nD_2/L) as used in Equation (7).

product of Alnico XII* is very high, its coercive force is lower than those of the ceramic materials. Consequently, ceramic magnets are ideally suited for use in periodic focusing structures, particularly those which must produce fields having large amplitude and short period, and which, therefore, require large values of H_d.

Each ring magnet in a periodic structure is subjected to a demagnetizing field from its neighboring ring or rings. In the case of ceramic magnets, the demagnetizing effects of these fields is negligible. Unstabilized Alnico loses magnetism when exposed to demagnetizing

* Trademark of the General Electric Co., Schenectady, N. Y.

fields.[8] Stabilization, however, reduces usable flux density. Therefore, Alnico ring magnets for periodic structures must have the proper size and degree of stabilization to produce a desired flux density in the presence of demagnetizing fields.

Of the ceramic magnetic materials listed in Table I, only that having the approximate composition $BaFe_{12}O_{19}$ and known as Indox I,* Magnadur,† or Ferrimag I,‡ is commercially available at present.

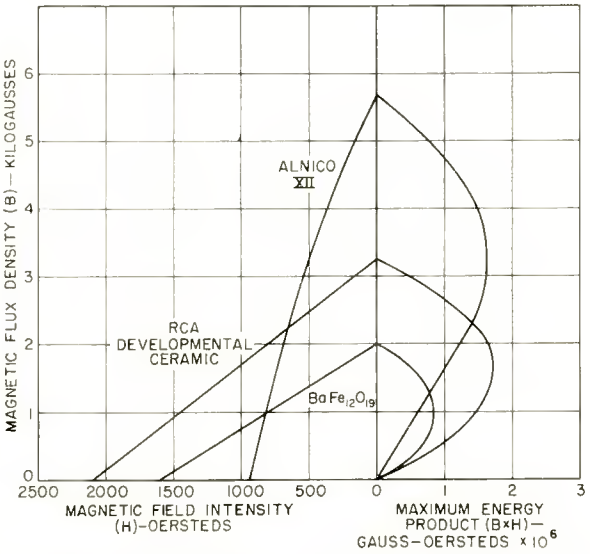

Fig. 6—Demagnetization and energy-product curves for various magnetic materials.

Design Procedure for Periodic Permanent Magnets

Some quantitative conclusions regarding the design of a periodic permanent magnet structure having minimum weight and volume can be drawn from Equations (3)-(8). For example, the inner diameter, d_1, of the shims should be made as small as possible, because (a) function f_1 in Equation (3) increases rapidly as d_1 decreases, as shown in Figure 2; and (b) the permeance P_2 also decreases with d_1, thereby increasing the field. The dimension $\delta = d_2 - d_1$ should also be made

[8] Carboloy Alnico Permanent Magnet Design Manual, PM-101, Carboloy Department of General Electric Company, p. 9.

* Trademark of the Indiana Steel Corporation, Valparaiso, Indiana.

† Trademark of the Ferroxcube Corporation of America, Saugerties, New York.

‡ Trademark of the Crucible Steel Company of America, Pittsburgh, Pennsylvania.

small so as to minimize the leakage flux between the hubs of the shims, but not so small as to permit magnetic saturation of the shim material. The thickness, t, of the shims should also be kept small to allow maximum T for a given period, and to reduce P_3. The shims, therefore, should be made of a metal which has high magnetic permeability at high flux densities.

Inspection of Equations (3) and (6) also indicates that for a given structure there is a specific air gap which will produce maximum field strength.

Table I

	Maximum Energy Product (B_dH_d) Max $\times 10^6$	Coercive Force H_c (Oersteds)	Ability to Withstand Strong Demagnetizing Fields	Specific Gravity	Temperature Coefficient	Commercially Available
Alnico IV Cast	1.3	700	Fair	7.0	<—.03%/C°	Yes
Alnico V Cast	5.0	575	Poor	7.3	<—.03%/C°	Yes
Alnico VI Cast	3.5	750	Fair	7.4	<—.03%/C°	Yes
Alnico XII Cast	1.6	950	Good	7.3	<—.03%/C°	Yes
Indox I* Magnadur† Ferrimag 1‡ $BaFe_{12}O_{19}$	0.8	1600	Superior	4.5	—.16%/C°	Yes
RCA Developmental Ceramic	1.8	2100	Superior	5.7		No

It is apparent from the preceding considerations that the following quantities can be either calculated or estimated:

(a) the magnetic field strength and period (from the space-charge conditions);

(b) the inside diameter of the shims (from the radial dimensions of the tube);

(c) the parameter δ and t (from the magnetic properties of the shim material).

It is then necessary to determine the optimum values for the air gap and the outside diameter, D_2, for a required field strength B_m.

In general, the optimum value for the air gap can be determined by trial and error from the demagnetization characteristic of the material employed. In the case of a ceramic magnetic material, the demagnetization curve is very nearly a straight line, so that both the optimum air gap and the magnetic field strength can be determined analytically.

The analytic expression for the demagnetization characteristic of a ceramic material is

$$B_d = KH_c + KH_d, \tag{9}$$

where H_c is the magnitude of the coercive force in oersteds and K is the slope of the demagnetization curve. Combining Equations (4), (8), and (9) with Equations (16), (21), (23), and (25) of the Appendix, the peak magnetic field strength on the axis is

$$B_m = \frac{\dfrac{4H_cT}{\pi g}\displaystyle\sum_{n=1}^{\infty}\frac{\sin\left(\dfrac{n\pi g}{L}\right)}{nI_0\left(n\dfrac{\pi d_1}{L}\right)}}{1+\dfrac{c}{g}+\displaystyle\sum_{n=1}^{\infty}b_n\frac{\sin\left(\dfrac{n\pi g}{L}\right)}{\dfrac{g}{L}}+\frac{S_n}{K}}, \tag{10}$$

$$n = 1, 3, 5, 7, 9 \ldots .$$

where

$$c = \frac{T\,(d_2^2 - d_1^2)}{K\,(D_2^2 - d_2^2)},$$

$$b_n = \frac{8Td_1\,I_1\left(\dfrac{n\pi d_1}{L}\right)}{\pi^2 K\,(D_2^2 - d_2^2)\,n^2\,I_0\left(\dfrac{n\pi d_1}{L}\right)},$$

$$S_n = \frac{8D_2L}{\pi^2 (D_2^2 - d_2^2)} \sum_{n=1}^{\infty} \frac{K_1\left(\frac{n\pi D_2}{L}\right)}{K_0\left(\frac{n\pi D_2}{L}\right)} \frac{\sin\left(\frac{n\pi T}{L}\right)}{n^2}.$$

$$n = 1, 3, 5, 7, 9 \ldots .$$

Here, K_0 and K_1 are the modified Bessel Functions of the second kind and of zero and first order, respectively. It can be seen that the inclusion of the additional flux path I changes the dependence of B_m (Equation (10)) on the air gap from the result obtained by Chang (Equation (27) of Reference (5)), particularly for very small values of g.

The optimum air gap can be obtained by setting

$$\frac{\partial B_m}{\partial g} = 0.$$

Taking only the first term in the numerator of Equation (10), i.e., obtaining the maximum for the fundamental,

$$\left\{1 + \frac{\pi}{1 + \frac{S_n}{K}} \sum_{n=1}^{\infty} b_n \left[n \cos n\left(\frac{\pi g}{L}\right) - \frac{\sin\left(\frac{n\pi g}{L}\right)}{\tan\left(\frac{\pi g}{L}\right)}\right]\right\} \tan\left(\pi \frac{g}{L}\right) - \frac{\pi g}{L} = \frac{\pi \frac{c}{L}}{\left(1 + \frac{S_n}{K}\right)}. \qquad (11)$$

$$n = 1, 3, 5, 7, 9 \ldots .$$

For most practical purposes, it will be sufficient to consider only the first terms of the series in both the numerator and denominator of Equation (10), and the first term of the series in Equation (11). Using these approximations, Equations (10) and (11) simplify to:

$$B_m = \frac{\dfrac{4H_c T \sin\left(\dfrac{\pi g}{L}\right)}{\pi g I_0\left(\dfrac{\pi d_1}{L}\right)}}{1 + \dfrac{1}{g}\left[c + L\, b_1 \sin\left(\dfrac{\pi g}{L}\right)\right] + \dfrac{S_1}{K}}, \tag{12}$$

and

$$\tan\left(\frac{\pi g}{L}\right) - \frac{\pi g}{L} = \frac{\pi \dfrac{c}{L}}{1 + \dfrac{S_1}{K}}. \tag{13}$$

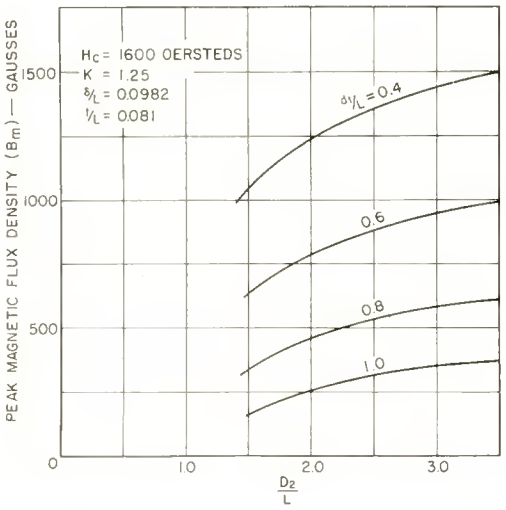

Fig. 7—Maximum field at optimum gap length as a function of D_2/L and d_1/L.

The maximum field intensity is not a critical function of g/L.

Design charts based on Equations (12) and (13) are given in Figures 7 and 8. These curves were computed for the ceramic material having the approximate composition $BaFe_{12}O_{19}$, for which $H_c = 1{,}600$ oersteds, and $K = 1.25$. Figure 7 shows the maximum field obtained with optimum gap length, g/L, as a function of D_2/L and d_1/L. Optimum gap length as a function of D_2/L, with d_1/L as a parameter,

is plotted in Figure 8. Values of $\delta/L = 0.0982$ and $t/L = 0.081$ were assumed for the shims. These values are fairly typical. For most structures $0 < t/L < 0.1$ and the dependence of B_m on δ/L is not very critical.

The efficiency of the structure can be improved slightly by two minor modifications: (a) the leakage flux P_3 (path III of Figure 3) can be reduced somewhat by making D_1 slightly less than D_2. If D_1 is made too small, however, the field at the axis will decrease; (b) because most of the leakage flux (path II in Figure 3) traverses only part of the hub of the shim, the hubs can be tapered slightly towards

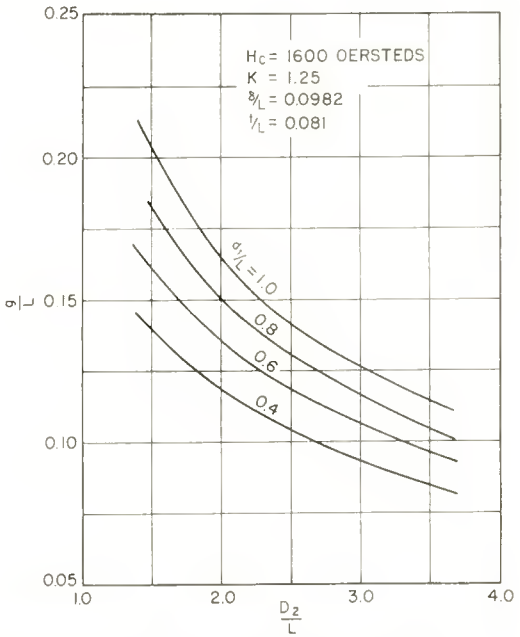

Fig. 8—Optimum value of g/L as a function of D_2/L and d_1/L.

the air gap (keeping d_1 constant) without saturating the shims. The effect of this taper is to reduce somewhat the leakage flux (path I of Figure 3).

Numerical Example

As a numerical example, consider a requirement for a periodic magnetic focusing field having a peak strength of 700 gausses, and a period of less than 1.9 inches for operation in the first pass band. In the design of the tube, the radial dimensions of that part of the tube which fit inside the permanent magnet should be made as small as

possible. Let the magnetic material employed in the focusing structure be Indox I. Assume the inside diameter of the shims to be 0.525 inch, and the period to be 0.764 inch. The latter value was chosen for the period as a compromise between

(a) a very small period which would produce an electron beam having a negligible degree of scalloping, but which would require the use of a very bulky magnetic structure (large D_2); and

(b) a period very close to the allowable maximum which could be obtained from a light magnetic structure (D_2 small), but which would result in a large degree of scalloping.

Values of $\delta/L = 0.0982$, and $t/L = 0.081$ were chosen for the shims, to insure that the shims would not be saturated. The length of the air gap was made 0.07 inch, which, as can be easily verified by trying different values of g in Equations (12) and (13), is close to the optimum. Only the first terms of the series were used in the following computations. Equation (3) yielded

$$B_m = 0.65\ H_d.$$

Consequently, for the required B_m of 700 gausses,

$$H_d = \frac{700}{0.65} = 1{,}090 \text{ oersteds.}$$

A value of 2 inches was chosen for D_2, the outside diameter of the ring magnets.

From Equations (5), (6), and (7),

$$P_1 = 0.94 \text{ inch},$$

$$P_2 = 0.74 \text{ inch},$$

$$P_3 = 3.1 \text{ inches}.$$

The total permeance was, therefore, 4.8 inches. The area of the ring magnet was $A' = (\pi/4)\,(D_2^2 - d_2^2) = 2.9$ square inches. Substitution of these values in Equation (8) yields

$$\frac{B_d}{H_d} = \frac{T}{A'} P_T = 0.53.$$

A straight line having a slope of —0.53 drawn from the origin of the demagnetization characteristic for Indox I intersected the demagnetization curve at point $H_d = 1{,}120$ oersteds. Since this value was very close to that required (1,090 oersteds), the choice of 2 inches for D_2 was substantially correct. A periodic permanent magnet structure having the determined dimensions was built. The measured flux distribution on the axis of this structure is shown in Figure 9. It can be seen that the measured field is in excellent agreement with the calculated value of 700 gausses. The desired "launching field" for the electron beam was obtained by the use of a magnetic shield in the region near the electron-gun end of the tube, and by modification of the first shim.

The charts given in Figures 7 and 8 considerably simplify the design procedure. Figure 7, for example, shows that for $B_m = 700$

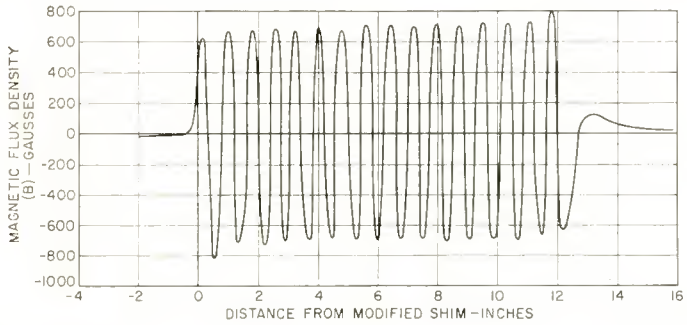

Fig. 9—Measured axial flux distribution on the axis of the magnetic structure discussed in the numerical example.

gausses and $d_1/L = 0.687$, $D_2 = 2.4\ L = 1.84$ inches, and Figure 8 shows that the optimum air gap $g = 0.126\ L = 0.096$ inch.

In order to check the results obtained by the use of Equations (12) and (13), the preceding example was also worked out using the first four terms of the series in the denominator in Equation (10) and the first three terms of the series in Equation (11).

The results of both calculations are compared in Table II. These results show that the terms of the series in Equations (10) and (11) vary in such a manner that the final result for B_m is nearly the same as that obtained using the simplified Equations (12) and (13). For many practical purposes, therefore, the charts of Figures 7 and 8 will provide sufficient accuracy. The use of these charts is further justified by the agreement between the results obtained from the simplified Equations (12) and (13) and those obtained experimentally.

The same design problem was also worked out for the developmental

ceramic material listed in Table I. For this material, H_c was 2,100 gausses and K was 1.55. In this case the required outside diameter, D_2, was only 1.13 inches, and the optimum air gap was 0.125 inch.

Sections of periodic permanent magnet structures using the two types of magnetic material discussed above are shown in Figure 10.

"Packaged" Assembly of a Traveling-Wave Amplifier Tube Using Periodic Permanent Magnets

A "packaged" traveling-wave power amplifier tube[9] using a periodic

Table II

	Results obtained using simplified Equations (12) and/or (13)	Results Obtained using Equations (10) and/or (11)
Optimum gap length g	$0.161\,L$	$0.207\,L$
A. $\frac{c}{g}$	0.151	0.117
B. Series $\frac{S_n}{K}$	$\frac{S_1}{K} = 0.589$	$\frac{1}{K}(S_1 + S_3 + S_5 + S_7) = 0.549$
C. Series U_n	$U_1 = 0.188$	$U_1 + U_2 + U_3 + U_4 = 0.215$
Denominator = 1+A+B+C of Equation (12) or (10)	1.928	1.881
Numerator of Equation (12) or (10)	1217	1184
B_m (gausses)	631	629

$$U_n = \sum_{n=1}^{r} b_n \frac{\sin\left(\frac{n\pi g}{L}\right)}{\frac{g}{L}}.$$

permanent-magnet structure for focusing is shown in Figure 11. The tube operates in the S band, and has a power output of 100 watts at the specified minimum gain of 20 decibels. The inside diameter of the tube helix is 0.216 inch. The r-f and d-c performance of this amplifier is as good as that obtained with a uniform magnetic focusing field. At the beam voltage of 3,700 volts and collector current of 250 milli-

[9] W. W. Siekanowicz and F. Sterzer, "A Developmental Wide-Band, 100-Watt, 20-DB S-Band Traveling-Wave Amplifier Utilizing Periodic Permanent Magnets," *Proc. I.R.E.*, Vol. 44, p. 55, January, 1956.

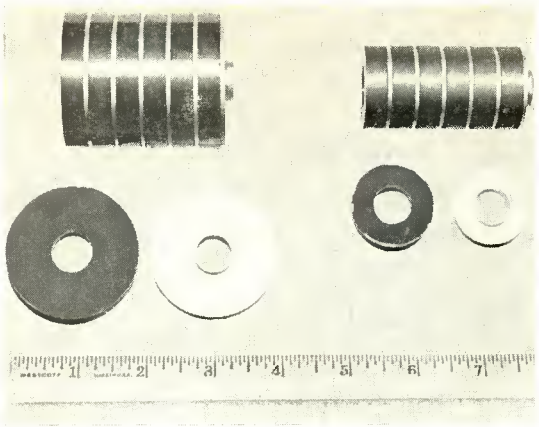

Fig. 10—Sections of typical periodic permanent-magnet focusing structures.

amperes required to provide the desired r-f performance, the current intercepted by the helix is less than 2.5 milliamperes. The magnetic structure used in conjunction with the tube is made of Indox I ($BaFe_{12}O_{19}$) and has the dimensions $T = 0.300$, $L = 0.724$, $d_1 = 0.525$, $d_2 = 0.600$, $D_1 = 1.9$, and $D_2 = 2.0$ inches. The entire magnet structure is 13⅞ inches long, and weighs 7.1 pounds. The peak magnetic field is about 620 gausses. This structure replaced a solenoid weighing 55 pounds and consuming about 400 watts of power.

R-F energy is fed into and removed from the tube by means of "coupled-helix" transducers.[10-12] Transducers of this type are well suited for use with periodic permanent-magnet structures because their radial dimensions can be made small. The coaxial input and output lines are brought out of the assembly through radial openings formed by slots in the mgnetic shims and semicircular grooves in the adjoining

Fig. 11—"Packaged" traveling-wave power amplifier using periodic permanent-magnet focusing structure.

[10] O. G. Owens, "Coupled Helix Attenuators for Traveling-Wave Tubes," Technical Report No. 68, Stanford University, California, August, 1953.

[11] R. Kompfner, "Some Theory and Experiments on Coupled Helices," paper presented at the Conference on Electron Tube Research, Palo Alto, Calif., June 19, 1953.

[12] J. S. Cook, R. Kompfner, and C. F. Quate, "Coupled Helices," *Bell Sys. Tech. Jour.*, Vol. 35, p. 127, January, 1956.

ring magnets. These modifications of the magnetic circuit have negligible effect on the axial component of the magnetic field.

Appendix—Calculation of Field in the Region of the Electron Beam

It can be shown[1,5] that the magnetic field in the region $0 \leq r \leq d_1/2$ (see Figure 1) is given by

$$B\ (z,r) = \sum_{n=1}^{\infty} \frac{4B_g \sin\left(\frac{n\pi g}{L}\right)}{I_0\left(\frac{n\pi d_1}{L}\right) n\pi} I_0\left(\frac{2n\pi r}{L}\right) \cos\left(\frac{2n\pi z}{L}\right), \qquad (14)$$

where B_g is the flux density in the air gap. B_g is given approximately by

$$B_g = \frac{F}{g} = \frac{H_d T}{g}, \qquad (15)$$

where F is the magnetomotive force produced by one magnet, and T is the length of the magnet in the direction of magnetization. Therefore, the maximum magnetic field on the axis of the magnet is given by

$$B_m = \frac{H_d T}{g} \sum_{n=1}^{\infty} \frac{1}{n} f_1\left(\frac{nd_1}{L}\right) \sin\left(\frac{n\pi g}{L}\right), \qquad (16)$$

$$n = 1, 3, 5 \ldots .$$

where

$$f_1\left(\frac{nd_1}{L}\right) = \frac{4}{\pi I_0\left(\frac{\pi n d_1}{L}\right)}.$$

The function $f_1(nd_1/L)$ versus nd_1/L is plotted in Figure 2. For most structures of practical importance, terms for $n > 1$ are small on the axis compared to the term for $n = 1$, so that the field distribution at the axis is nearly sinusoidal, and it is usually sufficient to calculate just the first term in Equation (16).

Evaluation of H_d in Equation (16) follows. The magnetomotive force produced by one magnet is

$$F = H_d T. \tag{17}$$

The total flux, ϕ, produced by a magnet is given approximately by

$$\phi = B_d A', \tag{18}$$

where A' is the area of the magnet perpendicular to the direction of magnetization.

The permeance, P, of a magnetic circuit is

$$P = \frac{\phi}{F}. \tag{19}$$

For a given permanent-magnet structure

$$\frac{\phi}{F} = \frac{B_d A'}{H_d T} = P_T. \tag{20}$$

Here P_T is the total permeance of the magnetic circuit external to the magnet. Once P_T is known, the ratio B_d/H_d can be calculated from Equation (20). The value of H_d is then determined by the point at which a straight line having a slope of $-TP_T/A'$ intersects the B-H curve in the second quadrant.

To simplify evaluation of the total permeance, P_T, the external magnetic circuit for each magnet has been divided into three flux paths, I, II, and III, as shown in Figure 3, so that

$$P_T = P_1 + P_2 + P_3.$$

The permeance of path I, in inches, is

$$P_1 \approx \frac{\pi\,(d_2^2 - d_1^2)}{4g}$$

$$\approx \frac{0.785\,(d_2^2 - d_1^2)}{g}. \tag{21}$$

In order to determine P_2, the permeance of path II, it is first necessary to find the total flux emanating from the shims which passes through the region $(0 < r < d_1/2)$. To find this flux, B_z is integrated over a plane perpendicular to the axis of the structure. The integration is carried out at a value of Z where B_z is a maximum.

From Reference (5), this flux is given by

$$\phi_2 = \sum_{n=1}^{\infty} \frac{2TLd_1 I_1\left(\frac{n\pi d_1}{L}\right) \sin\left(\frac{n\pi g}{L}\right)}{\pi n^2 g I_0\left(\frac{n\pi d_1}{L}\right)} H_d, \qquad (22)$$

$$n = 1, 3, 5, 7 \ldots .$$

Therefore,

$$P_2 = \frac{\phi_2}{F} = \frac{\phi_2}{H_d T} = \sum_{n=1}^{\infty} \frac{Ld_1 f_2\left(\frac{nd_1}{L}\right) \sin\left(\frac{n\pi g}{L}\right)}{n^2 g}, \qquad (23)$$

$$n = 1, 3, 5, 7 \ldots .$$

where

$$f_2\left(\frac{nd_1}{L}\right) = \frac{2I_1\left(\frac{n\pi d_1}{L}\right)}{\pi I_0\left(\frac{n\pi d_1}{L}\right)}.$$

The function $f_2(nd_1/L)$ versus nd_1/L is plotted in Figure 4. Computation of P_3, the permeance of flux path III in Figure 3, requires evaluation of ϕ_3, the total flux, in the region external to the periodic structure $(r > D_2)$. This quantity has been evaluated in Reference (5) and is given by

$$\phi_3 = \sum_{n=1}^{\infty} \phi'_n = \sum_{n=1}^{\infty} \frac{2LD_2}{n^2\pi} \cdot \frac{K_1\left(\frac{n\pi D_2}{L}\right)}{K_0\left(\frac{n\pi D_2}{L}\right)} \cdot \sin\left(\frac{n\pi T}{L}\right) H_d, \qquad (24)$$

$$n = 1, 3, 5, 7 \ldots .$$

where K_0 and K_1 are the modified Bessel functions of the second kind, of zero and first order, respectively.

Now

$$P_3 = \frac{\phi_3}{H_d T} = \sum_{n=1}^{\infty} \frac{LD_2 \sin\left(\frac{n\pi T}{L}\right)}{Tn^2} f_3\left(\frac{nD_2}{L}\right) \qquad (25)$$

$$n = 1, 3, 5, 7 \ldots .$$

where

$$f_3\left(\frac{nD_2}{L}\right) = \frac{2K_1\left(\frac{n\pi D_2}{L}\right)}{\pi K_0\left(\frac{n\pi D_2}{L}\right)}.$$

The function $f_3(nD_2/L)$ versus nD_2/L is plotted in Figure 5.

ACKNOWLEDGMENT

The authors wish to thank B. B. Brown for his guidance and many helpful suggestions, and Miss R. Pekarowitz, who made the numerical computations. They also wish to express their appreciation for the assistance given by W. J. Dodds, formerly of the RCA Tube Division, and now with Varian Associates, Palo Alto, California.

ANALYSIS AND SYNTHESIS OF TRANSITIONAL BUTTERWORTH-THOMSON FILTERS AND BANDPASS AMPLIFIERS*

By

YONA PELESS† AND T. MURAKAMI‡

Summary—In this paper a new family of networks is introduced. These networks have steady-state and transient characteristics which vary smoothly from the Butterworth characteristic (maximally flat amplitude) to that for the Thomson characteristics (maximally flat envelope delay). For this reason they will be called transitional Butterworth–Thomson networks. The synthesis of the transitional Butterworth–Thomson filter is based on the location of the poles of the transfer function in the complex frequency plane. The use of the resulting characteristics for low-pass filters or stagger-tuned bandpass amplifiers is given.

INTRODUCTION

THE theory of networks with maximally flat amplitude (MFA) characteristics was treated by S. Butterworth[1] and V. D. Landon.[2] H. Wallman[3] extended this theory to the bandpass amplifier and also calculated the transient response of an n-stage amplifier. Wallman shows that the Butterworth characteristic leads to excessive transient overshoot when many stages are cascaded.

A class of ladder networks with maximally flat envelope delay (MFED), or linear phase characteristics was investigated by W. E. Thomson.[4] The transient response of this type of network shows that although the overshoot is small (less than 1 per cent) the rise time is relatively slow when compared to that for the Butterworth-type networks.

---

* A substantial part of this paper was presented by Y. Peless as a thesis in partial fulfillment of the requirement of a Masters Degree at the Moore School of Electrical Engineering, University of Pennsylvania.

† Formerly RCA Victor Television Division, Camden, N. J.; now at the University of Pennsylvania, Philadelphia, Pa.

‡ RCA Victor Television Division, Camden, N. J.

[1] S. Butterworth, "On the Theory of Filter-Amplifiers," *Exp. Wireless and Wireless Eng.*, Vol. 7, p. 536, October, 1930.

[2] V. D. Landon, "Cascade Amplifiers With Maximal Flatness," *RCA Review*, Vol. V, p. 347, January, 1941.

[3] G. E. Valley and H. Wallman, *Vacuum Tube Amplifiers*, McGraw-Hill Book Company, Inc., New York, 1948, p. 176.

[4] W. E. Thomson, "Networks with Maximally-Flat Delay," *Wireless Engineer*, Vol. 29, p. 255, October, 1952.

In the present work, networks having characteristics lying between the Butterworth- and Thomson-type filters are investigated. They will be called transitional Butterworth–Thomson filters (TBT). This class of networks is studied in order to obtain a more favorable transient characteristic than that of either the Butterworth- or Thomson-type filters.

The method used to achieve these results is based on the study of the pole locations of the transfer function in the complex frequency plane. The final results are in the form of tables and curves which give design data for various order low-pass filters. The application of the result to stagger-tuned bandpass amplifiers is also given.

Before proceeding with the study of the TBT filter, a brief review will be made of the characteristics of the MFA and MFED networks.

Filters with Maximally Flat Amplitude or Butterworth Response

The definition of an MFA low pass network with n reactive elements is that the first n-1 derivatives of the amplitude function $T(\omega)$ with respect to ω^2 are zero at zero frequency. A particular property of the network with a maximally flat response is that the zeros of the normalized transfer admittance function, $Y(p)$, lie symmetrically on the left half of a unit circle in the complex frequency plane. Since the steady-state and transient characteristics of the MFA filter are quite well known, only a summary of the transient response data is given below in Table I. The equations for the steady-state characteristics of the MFA networks are given, for reference purposes, in Table XVI.

Table I shows the overshoot and 10-90 per cent rise time for MFA filters of orders 1 to 7.

It is seen from this table that the overshoot and rise time increase with the order of the filter. This is not a very desirable condition for

Table I—Rise Time and Overshoot of Maximally Flat n Pole Networks.

n	*Overshoot %*	*Rise Time*
1	0	2.20
2	4.3	2.15
3	8.15	2.29
4	10.9	2.43
5	12.8	2.56
6	14.3	2.67
7	15.4	2.80

faithful reproduction of a given signal. A very complete table of design constants for the Butterworth filter is given in a paper by Weinberg.[5] Both the current and voltage drive cases are treated for different source and load impedances.

Ladder Networks with Maximally Flat Envelope Delay

Networks with linear phase or maximally flat envelope delay have been studied by several authors. Laplume,[6] Thomson,[4] and Storch[7] give a good background in this area. A summary of the steady-state

Table II—Rise Time and Overshoot of Maximally Flat Envelope Delay Networks.

n	*Overshoot %*	*Rise Time*
1	0	2.20
2	.43	2.73
3	.75	3.07
4	.83	3.36
5	.76	3.58

equations which will be of use in this paper is given in Table XVI. In the investigation of the TBT filter, the transient response of the MFED filter is of interest since it will be used for comparison purposes.

The amount of overshoot and the rise times for the first five MFED ladder networks are given in Table II. The transient response of the MFED filter is quite symmetrical and the overshoot is small—characteristic of a network with flat delay or linear phase response. The amount of overshoot decreases after $n = 4$ and tends to zero for large values of n. A table of design constants for the MFED filter is given by Weinberg[8] for various order ladder networks.

---

[5] L. Weinberg, "Modern Synthesis Network Design from Tables — I," *Electrical Design*, Vol. 4, p. 22, September, 1956.

[6] J. Laplume, "Amplificateurs Moyenne Frequence a Distortion de Phase Reduite," *L'Onde Electrique*, Vol. 31, p. 357, August-September, 1951.

[7] L. Storch, "An Application of Modern Network Synthesis to the Design of Constant-Time-Delay Networks With Low-Q Elements," Convention Record I.R.E. 1954 National Convention. Part II, Circuit Theory, pp. 105-117.

[8] L. Weinberg, "Modern Synthesis Network Design From Tables," *Electrical Design*, Vol. 4, No. 20, p. 46, October, 1956.

Transitional Butterworth–Thomson Filters

A comparison of the results for the MFA and MFED filters shows that the overshoots of the unit step response for the Butterworth (MFA) filters are considerably greater than that for the Thomson (MFED) filters. It will be shown that the TBT filters will have steady-state and transient characteristics which will vary smoothly from the Butterworth- to the Thomson-type filters as the parameter controlling the pole positions is varied. From the data given it will be possible to design low-pass and bandpass filters with steady-state and transient characteristics intermediate between the Butterworth and Thomson filters.

Amplitude and Frequency Normalization

In this analysis all the transfer functions will be normalized so that the product of the pole distances from the origin and the response at zero frequency will be equal to unity. The transfer function of the MFA filter has this property since the poles are all located on a unit circle. In order that the MFED filter have this property we must normalize the transfer function of this filter. A ladder transfer function may be written as

$$Z(p) = \frac{1}{(p-p_1)(p-p_2)\cdots(p-p_n)}, \tag{1}$$

where $p = j\omega RC$, R is the terminating resistance of the ladder, and C is a capacitance so adjusted as to make the normalized bandwidth of the Butterworth filter unity. In Equation (1), the poles of the transfer function are given by $p_1, p_2 \cdots p_n$. In order that the product of the pole distances from the origin be equal to unity, the poles must satisfy the relation.

$$\prod_{k=1}^{n} |p_k| = 1. \tag{2}$$

The transfer impedance of the MFED filter can be written as (see Table XVI)

$$Z_n(\underline{p}) = \frac{{}_nd_0}{\underline{p}^n + {}_nd_{n-1}\,\underline{p}^{n-1} + \cdots + {}_nd_1\,\underline{p} + {}_nd_0}, \tag{3}$$

where $${}_nd_k = \frac{(2n-k)!}{2^{n-k}\,(n-k)!\,k!},$$

$$\underline{p} = j\omega R \Sigma C_i.$$

R is the terminating resistance of the ladder network, and ΣC_i is the sum of the shunt capacitances of the ladder. Equation (3) can be rewritten as

$$Z_n(\underline{p}) = \frac{1}{\frac{1}{{}_nd_0}\underline{p}^n + \frac{{}_nd_{n-1}}{{}_nd_0}\underline{p}^{n-1} + \cdots + \frac{{}_nd_1}{{}_nd_0}\underline{p} + 1}. \tag{4}$$

In order that Equation (4) will equal Equation (1) and satisfy the conditions given by Equation (2), we find that

$$p^n = \frac{1}{{}_nd_0}\underline{p}^n,$$

or

$$p = \frac{1}{({}_nd_0)^{1/n}}\underline{p}. \tag{5}$$

Using Equation (5) the transfer function given by Equation (4) becomes

$$Z_n(p) = \frac{1}{p^n + c_{n-1}p^{n-1} + c_{n-2}p^{n-2} + \cdots + c_1p + 1}, \tag{6}$$

where $$c_{n-1} = ({}_nd_{n-1})\,({}_nd_0)^{-1/n},$$

$$c_{n-2} = ({}_nd_{n-2})\,({}_nd_0)^{-2/n},$$

$$c_1 = ({}_nd_1)\,({}_nd_0)^{-(1-1/n)}.$$

The zeros of the denominator of Equation (6) give the pole locations of the MFED impedance function in the complex frequency plane. The normalization is such that the pole plots for the MFA and MFED transfer function have the same scale in the p-plane.

Pole Location for the MFA and MFED Filters

Table III gives the location of poles for the Butterworth[2] (MFA) and the Thomson (MFED) n[th] order transfer functions normalized

Table III—Location of Poles for MFA and MFED Filters of Orders 1 to 5.

	Poles of MFA Filters			*Poles of MFED Filters*		
n	p	r	$\phi°$	p	r	$\phi°$
1	-1	1	0	-1	1	0
2	$-0.7071 \pm j\,0.7071$	1	± 45	$-0.8660 \pm j\,0.5000$	1	± 30
3	-1	1	0	-0.9416	0.9416	0
	$-0.500 \pm j\,0.8660$	1	± 60	$-0.7456 \pm j\,0.7114$	1.0306	± 43.65
4	$-0.9239 \pm j\,0.3827$	1	± 22.5	$-0.9047 \pm j\,0.2709$	0.9444	± 16.67
	$-0.3827 \pm j\,0.9239$	1	± 67.5	$-0.6572 \pm j\,0.8301$	1.0588	± 51.63
5	-1	1	0	-0.9265	0.9265	0
	$-0.8090 \pm j\,0.5878$	1	± 36	$-0.8516 \pm j\,0.4427$	0.9598	± 27.47
	$-0.3090 \pm j\,0.9511$	1	± 72	$-0.5906 \pm j\,0.9072$	1.0825	± 56.93

as explained above. Figure 1 shows the meaning of notations used in the table.

Path Determining the Pole Position in the Complex Frequency Plane of TBT Filters

Path for One Pair of Poles

We now want to find a suitable path passing through the Butterworth and Thomson poles. Figure 2 shows one Butterworth pole $p_B(r_B,\phi_B)$ and one Thomson pole $p_T(r_T,\phi_T)$ and the path passing through these two poles.

The path will be defined by:

$$p = re^{j(\pi-\phi)} = -re^{-j\phi}, \tag{7}$$

where

$$r = r_T{}^m, \tag{8}$$

$$\phi = \phi_B - m\,(\phi_B - \phi_T), \tag{9}$$

m = variable parameter.

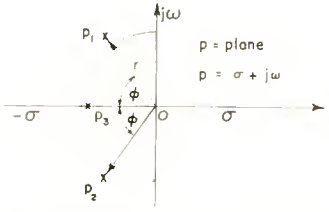

Fig. 1—Pole location of third-order MFED filter.

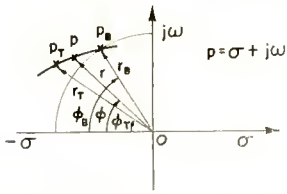

Fig. 2—Path passing through a Butterworth and a Thomson pole.

The parameter m provides a linear variation in the phasor angle of p. It will be presently shown that the value of r as given by Equation (8) will satisfy the normalization Equation (2). When $m = 0$, the pole position is that for the Butterworth case where $p = p_B$, and when $m = 1$, $p = p_T$, giving the pole location for the Thomson case. The value $m = 0.5$ denotes a pole which is the geometric mean between the two given cases. If the value of m is confined to $0 < m < 1$, all the poles on the path between p_B and p_T will be included. We shall deal in this section with these poles and with poles lying on the defined path outside the region $0 < m < 1$. The path shown in Figure 2 and defined by Equations (7), (8), and (9) joins poles located in the second quadrant. Since the poles always occur in conjugate complex pairs, a similar path will be found in the third quadrant.

Path for the n^{th}-Order Filter

In the example given above, the path was determined between one Butterworth and one Thomson pole. If the transfer function is of the n^{th} order, n Butterworth and n Thomson poles will be found in the complex frequency plane. For each pair of Butterworth and Thomson poles $p_{B,k}(r_{B,k}, \phi_{B,k})$ and $p_{T,k}(r_{T,k}, \phi_{T,k})$ as shown in Figure 3, a path $(r_{m,k}, \phi_{m,k})$ may be found defined by Equations (7), (8), and (9). For a specified value of the parameter m, n new poles may be found with $r_{m,k}$ as the distances from the origin. The product of these distances is

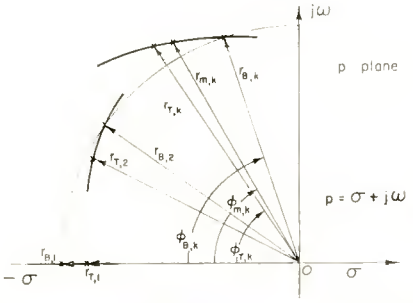

Fig. 3—Paths for n^{th} order TBT filter in the second quadrant (n odd).

$$r_{m,1} \cdot r_{m,2} \cdots r_{m,n} = r_{T,1}{}^{m} \cdot r_{T,2}{}^{m} \cdots r_{T,2}{}^{m} \cdots r_{T,n}{}^{m}$$

$$= \prod_{k=1}^{n} r_{T,k}{}^{m} = \left(\prod_{k=1}^{n} r_{T,k} \right)^{m} = 1 \tag{10}$$

by Equation (2).

Since the magnitude of the transfer function at the origin was defined to be independent of the continuous variable m, the n^{th} order transfer function can be written as

$$Z(p) = \frac{1}{p^n + b_{n-1}\, p^{n-1} + \cdots + b_1\, p + 1},$$

$$= \frac{1}{(p - p_{m,1})\ (p - p_{m,2}) \cdots (p - p_{m,n})}, \tag{11}$$

where

$$\prod_{k=1}^{n} |p_{m,k}| = \prod_{k=1}^{n} r_{m,k} = 1.$$

The steady-state and transient characteristics can be found using the standard techniques.

We shall next discuss the steady-state and transient characteristics of TBT filters of orders 2 to 5, to show their particular properties.

Second-Order TBT Transfer Functions

It is seen from Table III that for $n = 2$, both the MFA and the MFED poles are located on a circle with unit radius. The TBT path is obviously the circle itself for this case. The phase ϕ varies linearly with the parameter m as given by Equation (9). The bandwidth and the amount of overshoot for this case may be solved analytically as functions of ϕ or m. The rise time of the second and higher order filters involves the solution of a transcendental equation and therefore we shall solve this case and others by solving for discrete points on the path namely; $m = -0.2$; 0; 0.2; 0.4; 0.6; 0.8; 1.0; 1.2. The angle for the second-order case, is found from Equation (9) and Table III.

$$\phi = 45° - 15°m. \tag{12}$$

Poles of the Transfer Function

The poles on the second-order TBT transfer function are given by

$$p_{m,1}, p_{m,2} = -e^{\mp j\phi} = -\cos(45° - 15°m) \pm j \sin(45° - 15°m). \quad (13)$$

The second-order TBT transfer function is given by

$$\begin{aligned} Z(p) &= \frac{1}{(p-p_1)(p-p_2)} = \frac{1}{p^2 - 2\,\mathrm{Re}(p_1) + 1}, \\ &= \frac{1}{p^2 + 2\cos(45° - 15°m) + 1} = \frac{1}{p^2 + b_1 p + 1}, \end{aligned} \quad (14)$$

where Re means the real part of the quantity, and

$$b_1 = 2\cos(45° - 15°m),$$

and m has been omitted from the subscripts. The coefficient b_1 is found in Table IV.

Table IV—Location of Poles and the Coefficients of the Second-Order TBT Transfer Functions.

m	−0.2	0	0.2	0.4	0.6	0.8	1.0	1.2
$\phi°$	48	45	42	39	36	33	30	27
b_1	1.3382	1.4142	1.4862	1.5542	1.6180	1.6774	1.7321	1.7820
p_1, p_2	−.6691 ±j.7431	−.7071 ±j.7071	−.7431 ±j.6691	−.7771 ±j.6293	−.8090 ±j.5878	−.8387 ±j.5446	−.8660 ±j.5000	−.8910 ±j.4540

Steady-State and Transient Characteristics

The steady-state characteristics of the second order TBT filters are given in Figures 4 and 5. It is seen from Figure 4 that the 3-decibel bandwidth goes up for decreasing values of the parameter m. The phase, on the other hand, is most linear (or the envelope delay maximally flat) for $m = 1.0$ and becomes less linear for lower values of m. The transient response given in Figure 6 shows that the rise time becomes longer and the overshoots smaller when the parameter m is increased.

Bandwidth, Rise Time, and Overshoots

Table V and Figure 7 summarize the normalized 3-decibel bandwidth, B, the rise time, τ, and the percentage of overshoot, γ, as functions of the parameter m. It may be noticed in Figure 7 that the decrease of the overshoot is much faster than the decrease of the bandwidth. This data may be used for the design of a filter or an amplifier for a specified amount of overshoot, as will be shown later.

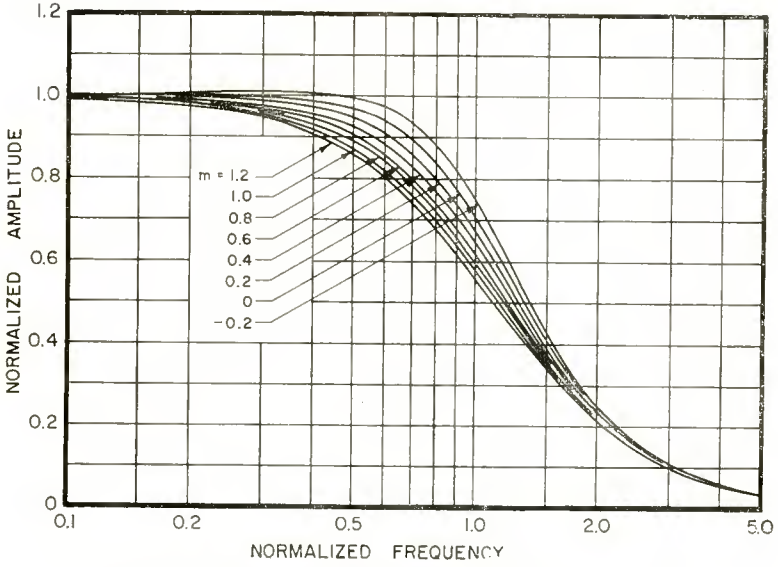

Fig. 4—Amplitude response of second-order filters.

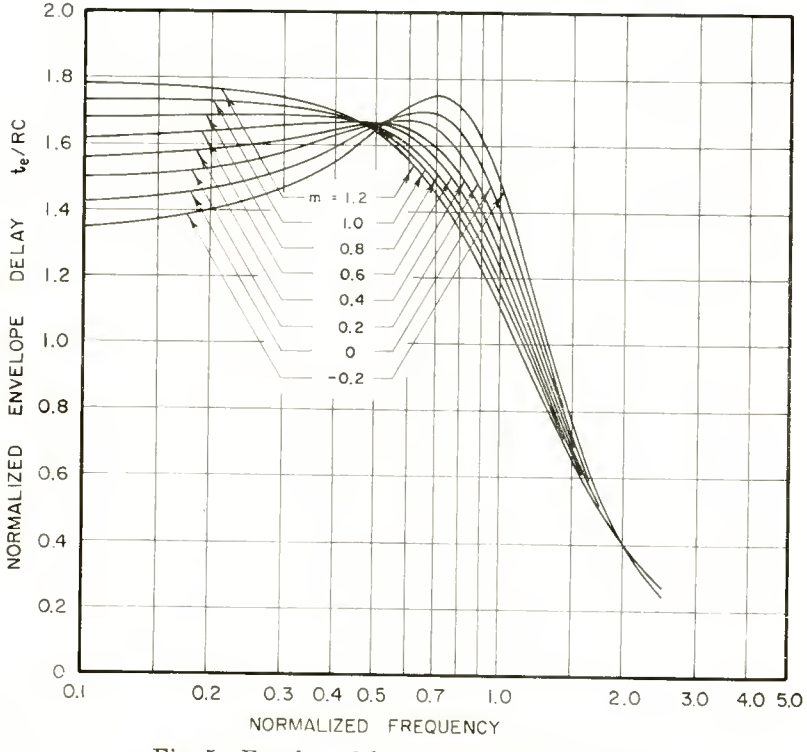

Fig. 5—Envelope delay of second-order filters.

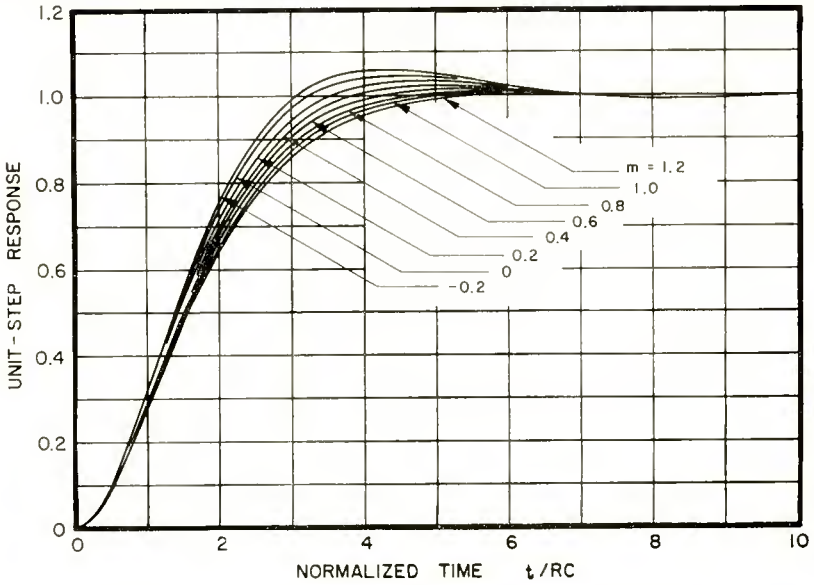

Fig. 6—Unit-step response of second-order filters.

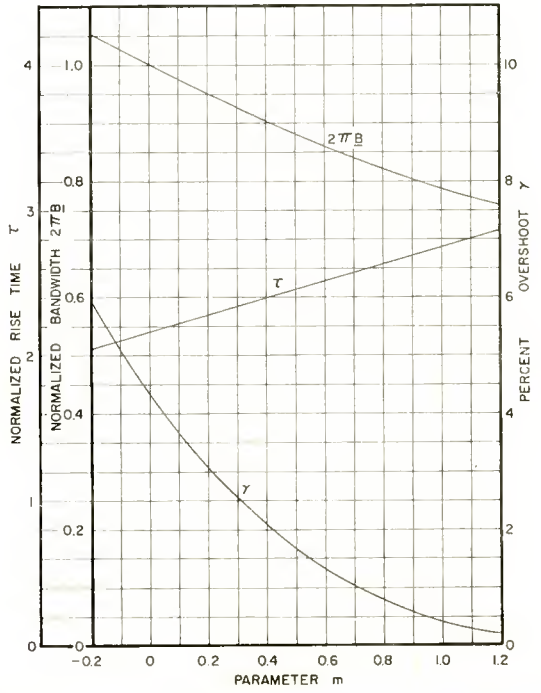

Fig. 7—Bandwidth, rise-time and overshoot of second-order TBT filters.

Table V—Variation of Bandwidth, Rise Time, and Overshoot With the Parameter m.

m	$2\pi B$ (normalized)	τ (normalized)	$\gamma\%$
−0.2	1.054	2.04	5.91
0	1	2.15	4.3
0.2	0.949	2.27	3.04
0.4	0.902	2.39	2.07
0.6	0.859	2.50	1.32
0.8	0.820	2.62	0.79
1.0	0.786	2.73	0.43
1.2	0.756	2.84	0.21

Third-Order TBT Transfer Functions

The third-order transfer function has one pole on the negative real axis and two complex conjugate poles. For the real poles the path will be the real axis. As seen from Table III the Thomson pole on the real p axis is $p_{T1} = -0.9416$. From Equations (7), (8), and (9) the path on the σ axis is defined by

$$p_{m,1} = -0.9416^m. \tag{15}$$

The Butterworth pole in the second quadrant is $p_{B,2} = -e^{-j60^\circ}$ and the corresponding Thomson pole in the same quadrant is $p_{T,2} = -1.0306e^{-j43.65^\circ}$ as seen from Table III. The path connecting these poles is

$$p_{m,2} = -1.0306^m \cdot e^{-j(60^\circ - 16.35^\circ m)}. \tag{16}$$

The pole $p_{m,3}$ on the path in the third quadrant will be the complex conjugate of $p_{m,2}$. The TBT transfer function may now be written

$$Z(p) = \frac{1}{(p-p_1)(p-p_2)(p-p_3)} = \frac{1}{(p-p_1)[p^2 - 2\mathrm{Re}(p_2)\,p + |p_2|^2]}$$

$$= \frac{1}{p^3 - [p_1 + 2\mathrm{Re}(p_2)]\,p^2 + [|p_2|^2 + 2p_1\mathrm{Re}(p_2)]\,p - p_1|p_2|^2}, \tag{17}$$

where m has been omitted from the subscript. Since p_1 is negative real and $|p_2| = |p_3|$,

$$-p_1|p_2|^2 = |p_1| \cdot |p_2| \cdot |p_3| = 1. \tag{18}$$

The last equality is found by Equation (2). We now substitute Equations (15), (16) and (18) into Equation (17) and find

$$Z(p) = \frac{1}{\{p^3 + [0.9416^m + 2 \cdot 1.0306^m \cos(60° - 16.35°m)]\, p^2 + [1.0306^{2m} + 2 \cdot 0.9416^m \cdot 1.0306^m \cos(60° - 16.35°m)]\, p + 1\}}$$

$$= \frac{1}{p^3 + b_2 p^2 + b_1 p + 1}, \tag{19}$$

where

$$b_1 = 1.0306^{2m} + 2\,(0.9416^m)\,(1.0306^m)\cos(60° - 16.35°m),$$

and

$$b_2 = 0.9416^m + 2\,(1.0306^m)\cos(60° - 16.35°m).$$

Table VI gives the location of the poles and the coefficients of the TBT transfer functions for discrete values of m.

Table VI—Location of Poles and the Coefficients of Third-Order TBT Transfer Functions.

m	−0.2	0	0.2	0.4	0.6	0.8	1.0	1.2
p_1	−1.0121	−1	−0.9880	−0.9764	−0.9645	−0.9530	−0.9416	−0.9304
$\|p_2\|$	0.9940	1	1.0060	1.0121	1.0183	1.0244	1.0306	1.0369
$\phi_2°$	63.27	60	56.73	53.46	50.19	46.92	43.65	40.38
p_2, p_3	−.4471 ±j.8877	−.5000 ±j.8660	−.5519 ±j.8411	−.6026 ±j.8131	−.6515 ±j.7823	−.6997 ±j.7481	−.7456 ±j.7114	−.7899 ±j.6717
b_1	1.893	2	2.103	2.201	2.294	2.383	2.466	2.547
b_2	1.906	2	2.092	2.182	2.268	2.352	2.433	2.510

Steady-State and Transient Response

Figures 8 and 9 show the steady-state characteristics of the third-order TBT filters. Figure 10 shows the transient response of these filters.

Bandwidth, Rise Time, and Overshoots

The normalized bandwidth, normalized rise time and the overshoots of the third-order TBT filters are given in Table VII and Figure 11 as functions of the parameter m. This figure and table is used in the next section for the design of a low-pass filter or a stagger-tuned bandpass amplifier.

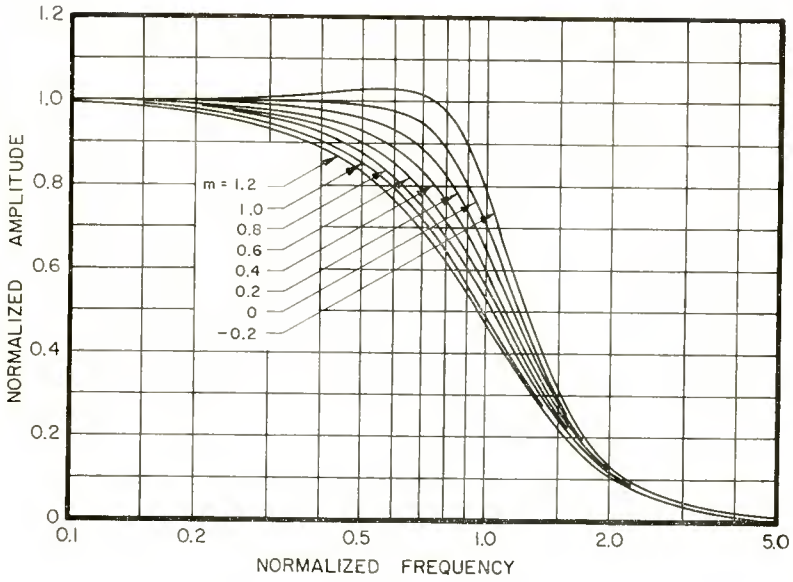

Fig. 8—Amplitude response of third-order filters.

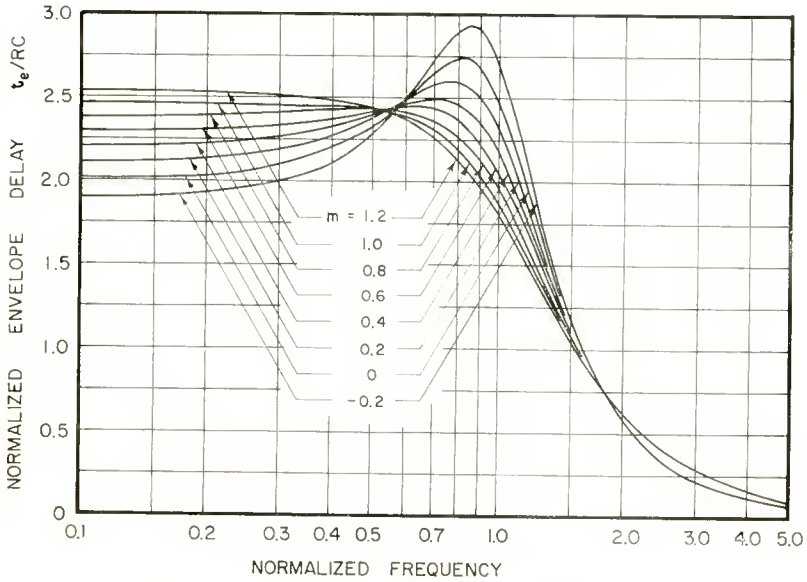

Fig. 9—Envelope delay of third-order filters.

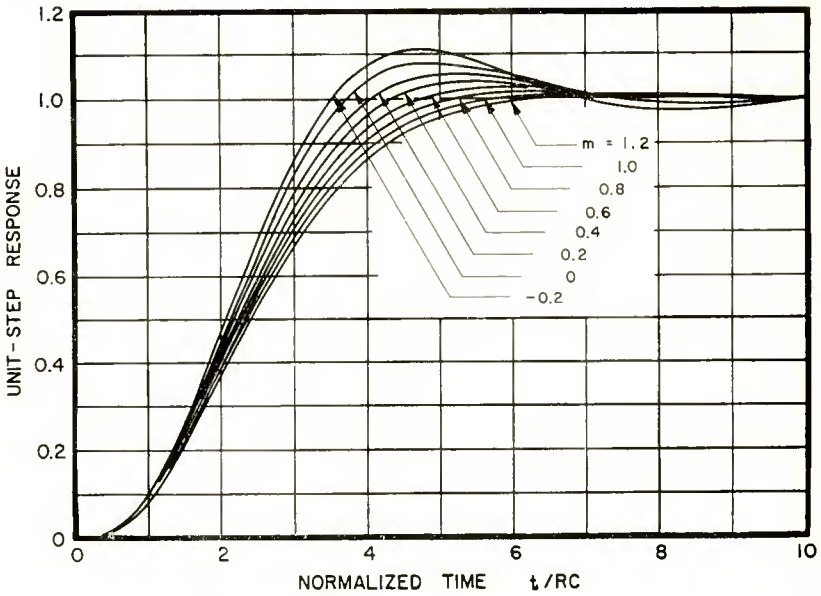

Fig. 10—Unit-step response of third-order filters.

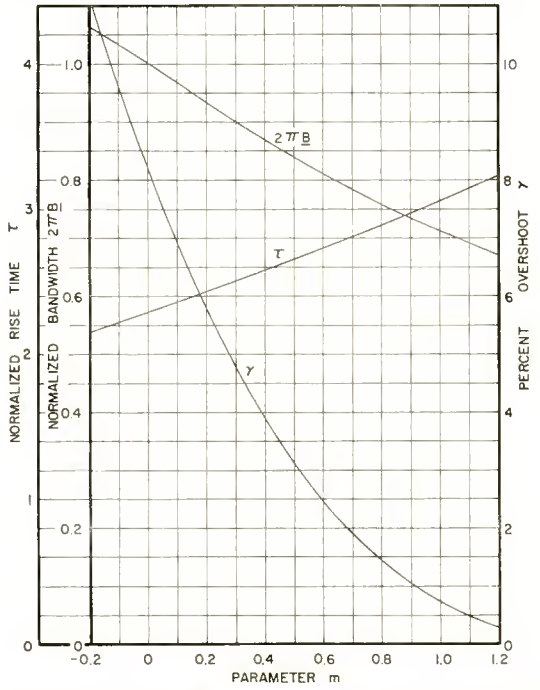

Fig. 11—Bandwidth, rise time and overshoot of third-order TBT filters.

Table VII—Variation of Bandwidth, Rise Time, and Overshoot With the Parameter m.

m	$2\pi B$ (normalized)	τ (normalized)	$\gamma\%$
−0.2	1.064	2.16	11.1
0	1	2.29	8.15
0.2	0.933	2.44	5.74
0.4	0.868	2.59	3.87
0.6	0.810	2.74	2.45
0.8	0.756	2.90	1.43
1.0	0.712	3.07	0.75
1.2	0.671	3.23	0.30

Fourth-Order TBT Transfer Functions

The fourth-order TBT transfer function has two pairs of complex conjugate poles given in Table III for the MFA and MFED cases. The transfer function may be found in a manner similar to that used for the third-order case, and is given by

$$Z(p) = \frac{1}{p^4 + b_3p^3 + b_2p^2 + b_1p + 1}, \tag{20}$$

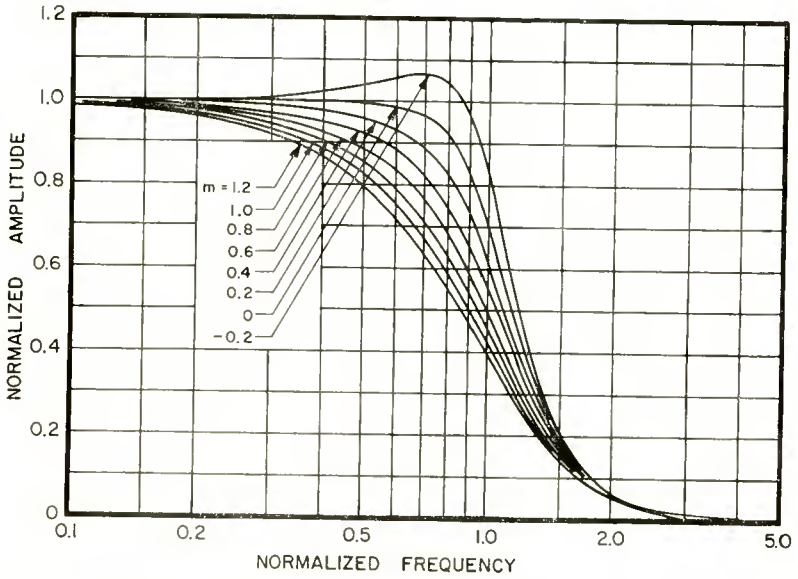

Fig. 12—Amplitude response of fourth-order filters.

where

$$b_1 = 2\,[\,|p_1|^2\,\mathrm{Re}\,(p_3) + |p_3|^2\,\mathrm{Re}\,(p_1)\,],$$
$$b_2 = |p_1|^2 + |p_3|^2 + 4\,\mathrm{Re}\,(p_1)\,\mathrm{Re}\,(p_3),$$
$$b_3 = -2\,[\mathrm{Re}\,(p_1) + \mathrm{Re}\,(p_3)\,],$$
$$p_1 = -1.0588^m\, e^{-j(67.5^\circ - 15.87^\circ m)},$$
$$p_3 = -0.9444^m\, e^{-j(22.5^\circ - 5.83^\circ m)}.$$

The coefficients b_1, b_2 and b_3 are shown in Table VIII.

Steady-State and Transient Response

Figures 12 and 13 show the steady-state characteristics of the fourth-order TBT filters. Figure 14 gives the transient response of these filters.

Bandwidth, Rise Time, and Overshoots

The normalized bandwidth, normalized rise time, and the overshoots of the fourth-order TBT filters are given in Table IX and Figure 15 as functions of the parameter m.

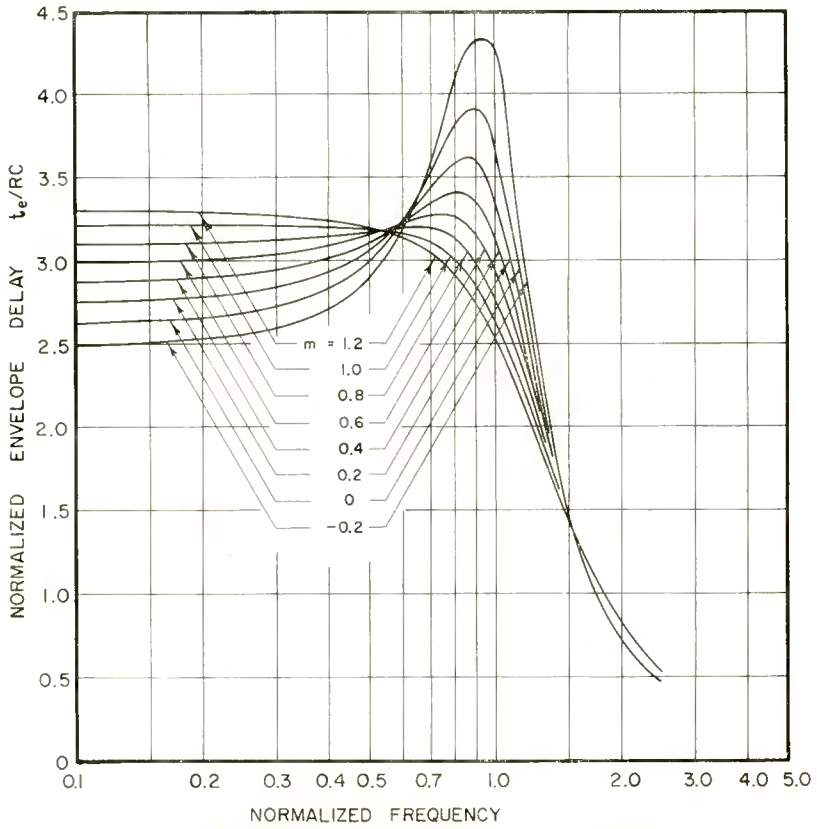

Fig. 13—Envelope delay of fourth-order filters.

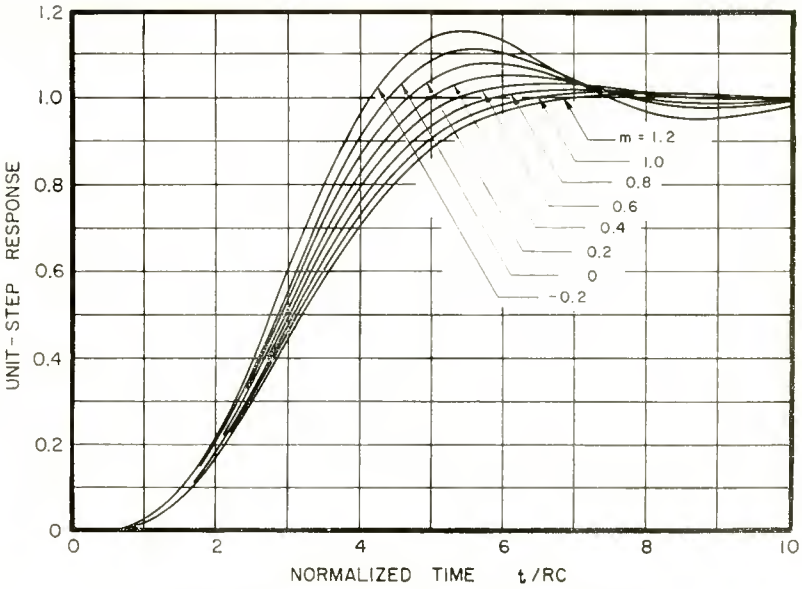

Fig. 14—Unit-step response of fourth-order filters.

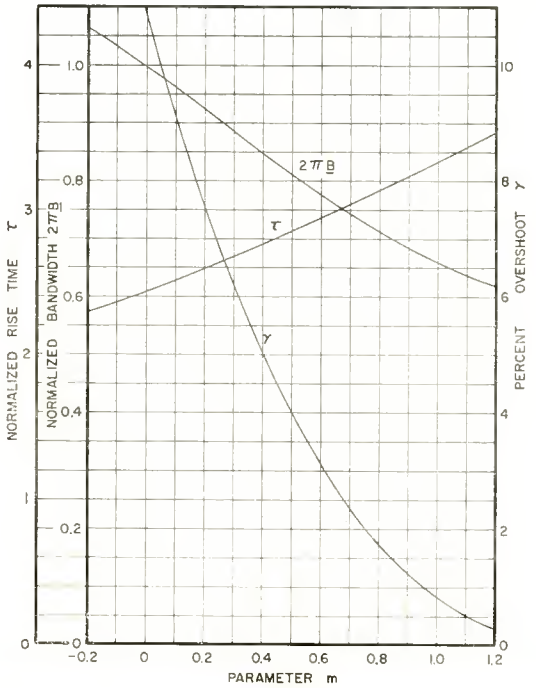

Fig. 15—Bandwidth, rise time and overshoot of fourth-order TBT filters.

Table VIII—Location of Poles and the Coefficients of Fourth-Order TBT Transfer Functions.

m	−0.2	0	0.2	0.4	0.6	0.8	1.0	1.2
$\lvert p_1 \rvert$	0.9886	1	1.0115	1.0231	1.0349	1.0468	1.0588	1.0710
$\phi_1°$	70.67	67.50	64.33	61.15	57.98	54.80	51.63	48.46
p_1, p_2	−.3273 ±j.9328	−.3827 ±j.9239	−.4381 ±j.9117	−.4937 ±j.8961	−.5488 ±j.8775	−.6034 ±j.8553	−.6572 ±j.8301	−.7101 ±j.8017
$\lvert p_3 \rvert$	1.0115	1	0.9886	0.9774	0.9663	0.9553	0.9444	0.9337
$\phi_2°$	23.67	22.50	21.33	20.17	19.00	17.84	16.67	15.50
p_3, p_4	−.9264 ±j.4060	−.9239 ±j.3827	−.9209 ±j.3596	−.9175 ±j.3369	−.9136 ±j.3146	−.9094 ±j.2925	−.9047 ±j.2709	−.8998 ±j.2495
b_1	2.4808	2.6131	2.7408	2.8641	2.9818	3.0943	3.2010	3.3023
b_2	3.2133	3.4142	3.6143	3.8139	4.0102	4.2033	4.3916	4.5746
b_3	2.5074	2.6131	2.7180	2.8223	2.9248	3.0256	3.1240	3.2198

Table IX—Variation of Bandwidth, Rise Time, and Overshoot with Parameter m.

m	$2\pi B$ (normalized)	τ (normalized)	$\gamma\%$
−0.2	1.064	2.29	14.9
0	1	2.43	10.9
0.2	0.924	2.59	7.58
0.4	0.845	2.77	5.01
0.6	0.774	2.95	3.12
0.8	0.712	3.14	1.75
1.0	0.659	3.36	0.83
1.2	0.617	3.53	0.29

Fifth-Order TBT Transfer Functions

The fifth-order TBT transfer function has one real pole and two pairs of complex conjugate poles as given in Table III for the MFA and MFED cases. The fifth-order transfer function may be found in the same way as in the previous cases and can be expressed as

$$Z(p) = \frac{1}{p^5 + b_4 p^4 + b_3 p^3 + b_2 p^2 + b_1 p + 1}, \tag{21}$$

where

$$b_1 = |p_2|^2 \cdot |p_4|^2 - 2\,|p_1| \cdot [\,|p_2|^2\,\mathrm{Re}(p_4) + |p_4|^2\,\mathrm{Re}(p_2)\,],$$

$$b_2 = |p_1| \cdot [\,|p_2|^2 + |p_4|^2 + 4\mathrm{Re}(p_2)\,\mathrm{Re}(p_4)\,] - 2\,[\,|p_2|^2\,\mathrm{Re}(p_4) + |p_4|^2\,\mathrm{Re}(p_2)\,],$$

$$b_3 = |p_2|^2 + |p_4|^2 + 4\mathrm{Re}(p_2) \cdot \mathrm{Re}(p_4) + 2\,p_1 \cdot [\mathrm{Re}(p_2) + \mathrm{Re}(p_4)],$$

$$b_4 = |p_1| - 2\,[\mathrm{Re}(p_2) + \mathrm{Re}(p_4)],$$

$$p_1 = -0.9265^m,$$

$$p_2 = -0.9598^m\, e^{-j(36^\circ - 8.53^\circ m)},$$

$$p_4 = -1.0825^m\, e^{-j(72^\circ - 15.07^\circ m)}.$$

The calculated values of the coefficients b_1, b_2, b_3, and b_4 of the transfer function are given in Table X.

Table X—Location of Poles and the Coefficients of Fifth-Order TBT Transfer Functions.

m	−0.2	0	0.2	0.4	0.6	0.8	1.0	1.2
$-p_1$	1.0154	1	0.9848	0.9699	0.9552	0.9408	0.9265	0.9125
$\lvert p_2\rvert$	1.0082	1	0.9918	0.9837	0.9757	0.9677	0.9598	0.9520
$\phi_2{}^\circ$	37.71	36	34.29	32.59	30.88	29.18	27.47	25.76
p_2, p_3	−.7975 ±j.6168	−.8090 ±j.5878	−.8195 ±j.5587	−.8289 ±j.5297	−.8373 ±j.5008	−.8449 ±j.4718	−.8516 ±j.4427	−.8574 ±j.4138
$\lvert p_4\rvert$	0.9843	1	1.0160	1.0323	1.0488	1.0655	1.0825	1.0998
$\phi_4{}^\circ$	75.01	72	68.99	65.97	62.96	59.95	56.93	53.92
p_4, p_5	−.2544 ±j.9507	−.3090 ±j.9511	−.3641 ±j.9485	−.4205 ±j.9428	−.4767 ±j.9342	−.5338 ±j.9221	−.5906 ±j.9072	−.6478 ±j.8888
b_1	3.079	3.236	3.387	3.534	3.673	3.808	3.936	4.060
b_2	4.902	5.236	5.569	4.905	6.235	6.564	6.888	7.206
b_3	4.933	5.236	5.541	5.851	6.159	6.470	6.778	7.085
b_4	3.119	3.236	3.352	3.469	3.583	3.698	3.811	3.923

Steady-State and Transient Response

Figures 16 and 17 show the steady-state characteristics of the fifth-order TBT filters. Figure 18 gives the transient response of these filters.

Bandwidth, Rise Time, and Overshoots

The normalized bandwidth, normalized rise time, and the overshoots of the fifth order TBT filters are given in Table XI and Figure 19, as a function of the parameter m.

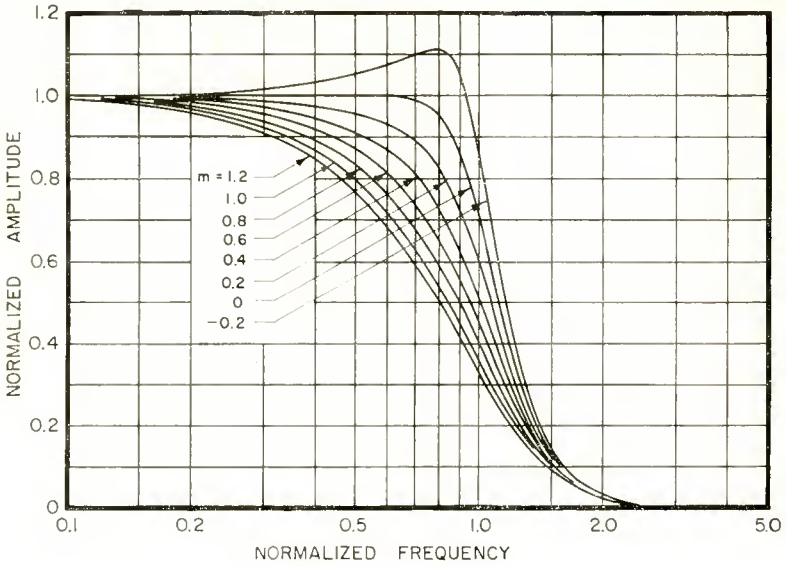

Fig. 16—Amplitude response of fifth-order filters.

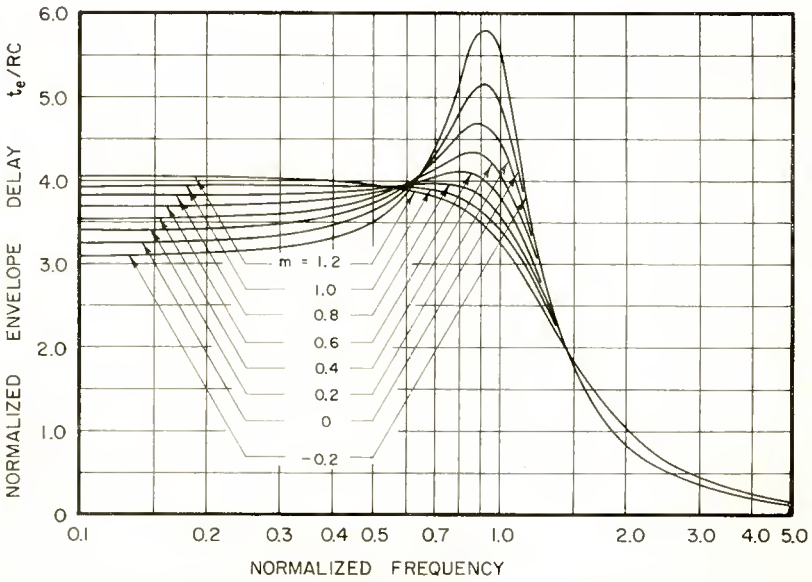

Fig. 17—Envelope delay of fifth-order filters.

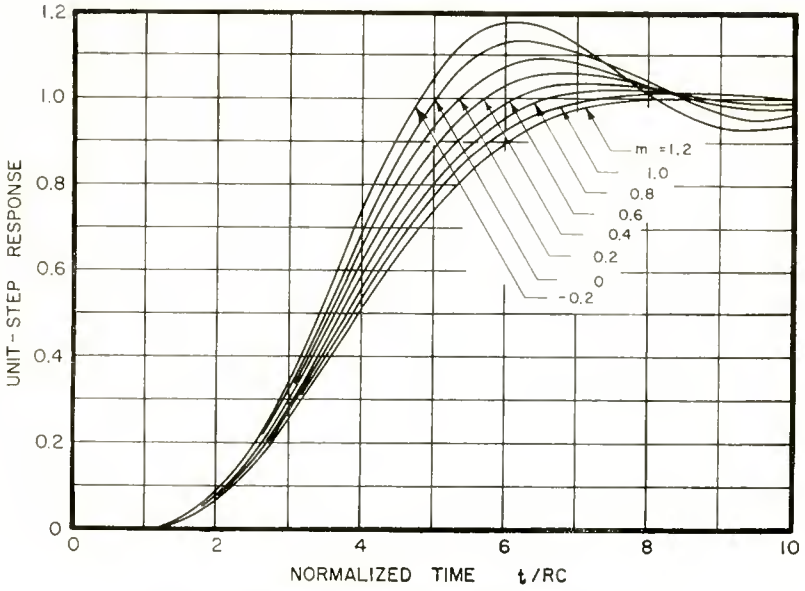

Fig. 18—Unit-step response of fifth-order filters.

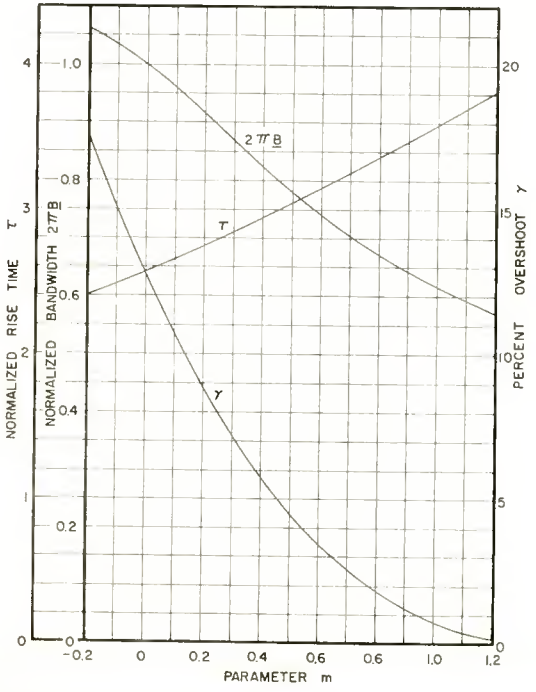

Fig. 19—Bandwidth, rise-time and overshoot of fifth-order TBT filters.

Table XI—Variation of Bandwidth, Rise Time, and Overshoot with Parameter m.

m	$2\pi B$ (normalized)	τ (normalized)	$\gamma\%$
−0.2	1.064	2.40	17.6
0	1	2.56	12.8
0.2	0.916	2.74	8.82
0.4	0.824	2.94	5.71
0.6	0.740	3.15	3.46
0.8	0.671	3.36	1.83
1.0	0.617	3.58	0.75
1.2	0.572	3.81	0.18

Summary of TBT Filters

From the study of the various order TBT filters given in this section it is seen that a smooth transition in the steady-state and transient characteristics can be obtained between the Butterworth (MFA) and the Thomson type (MFED) filters. It is noted that in the design of filters or amplifiers with little or no overshoot, values of m greater than unity may be used. The actual design procedure for filters and filter amplifiers based on the results of this section is given next.

Synthesis of the Ladder Network From a Given Transfer Function

The process of synthesizing a network from its known transfer function is well known. It will be given here as applied to the ladder networks discussed in this paper.

Cauer's method[9] as described in Guillemin's article[10] leads to a simple solution for the lossless ladder. Consider an n^{th} order ladder network which has n reactive elements as shown in Figure 20.
In this analysis it is assumed that if n is even, $C_1 = 0$. The n^{th} order transfer function case has n poles and no zeros, and may be written as

[9] W. Cauer, "Ausgangsseitig Leerlaufende Filter," *Eleck. Nachrichten Tech.*, Vol. 16, p. 161, June, 1939.

[10] E. A. Guillemin, "A Summary of Modern Methods of Network Synthesis," *Advances in Electronics*, Academic Press, New York, New York, Vol. 3, p. 261, 1951.

$$Z(p) = \frac{1}{b_n p^n + b_{n-1} p^{n-1} + \cdots + b_2 p^2 + b_1 p + 1}. \tag{22}$$

The driving-point impedance, Z_{22}, looking from terminals 3 and 4 of Figure 20 into the network, may be found by dividing the even part of the denominator of the transfer function, given by Equation (22) by its odd part.[11] Z_{22} is therefore given by

$$Z_{22} = \frac{b_n p^n + b_{n-2} p^{n-2} + \cdots + b_2 p^2 + 1}{b_{n-1} p^{n-1} + \cdots + b_3 p^3 + b_1 p} \tag{23}$$

when n is even, and by,

$$Z_{22} = \frac{b_{n-1} p^{n-1} + b_{n-3} p^{n-3} + \cdots + b_2 p^2 + 1}{b_n p^n + \cdots + b_3 p^3 + b_1 p} \tag{24}$$

for odd values of n.

In order to carry out the synthesis of the network, Equations (23) and (24) are expanded into continued fractions given by

$$Z_{22} = k_1 p + \cfrac{1}{k_2 p + \cfrac{1}{k_3 p + \cdots + \cfrac{1}{k_n p}}} \tag{25}$$

when n is even, and

$$Z_{22} = \cfrac{1}{g_1 p + \cfrac{1}{g_2 p + \cdots + \cfrac{1}{g_n p}}} \tag{26}$$

for odd values of n.

All k's and g's must be positive if Z_{22} is physically realizable

[11] Reference (10), p. 277.

(Hurwitz Criterion). The driving-point impedance, Z_{22}, of the n^{th} order ladder network shown in Figure 20 may be written in terms of the circuit elements as

$$Z_{22} = \cfrac{1}{pC_1 + \cfrac{1}{pL_1 + \cfrac{1}{pC_2 + \cfrac{1}{pL_2 + \cdots}}}} \tag{27}$$

when n is odd. If n is even, $C_1 = 0$ and Equation (27) becomes

$$Z_{22} = pL_1 + \cfrac{1}{pC_2 + \cfrac{1}{pL_2 + \cdots}}. \tag{28}$$

Comparing Equation (25) with Equation (28) and Equation (26) with Equation (27), the inductances and capacitances of the ladder network are easily found.

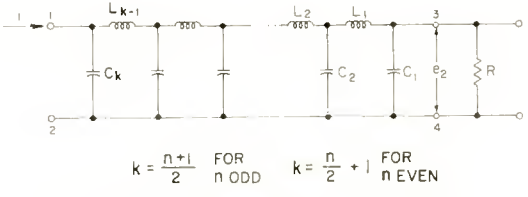

Fig. 20—n^{th} order ladder network.

Design of Lossless Low-Pass Filters

Tables XII to XV give the normalized inductances and capacitances for the various ladder networks shown in Figures 21 to 24, respectively. The normalized inductances and capacitances given in the tables are for the values of m used previously. The circuit constants for other values of m between $-.2$ and 1.2 may be found by means of graphical interpolation.

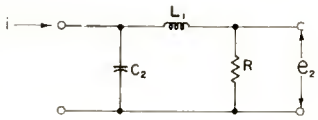

Fig. 21—Second-order ladder network.

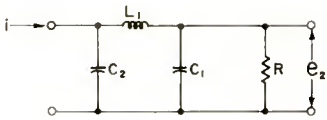

Fig. 22—Third-order ladder network.

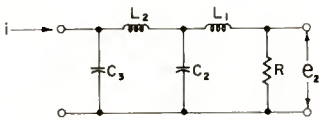

Fig. 23—Fourth-order ladder network.

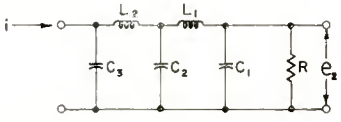

Fig. 24—Fifth-order ladder network.

Table XII—Coefficients of Second-Order TBT Transfer Functions and the Corresponding Circuit Constants.

m	−0.2	0	0.2	0.4	0.6	0.8	1.0	1.2
$b_1 = \frac{C_2}{C}$	1.338	1.414	1.486	1.554	1.618	1.677	1.732	1.782
$\frac{L_1}{R^2C} = \frac{1}{b_1}$	0.747	0.707	0.673	0.643	0.618	0.596	0.577	0.561

Table XIII—Coefficients of Third-Order TBT Transfer Functions and the Corresponding Circuit Constants.

m	−0.2	0	0.2	0.4	0.6	0.8	1.0	1.2
b_1	1.893	2	2.103	2.201	2.294	2.383	2.466	2.547
b_2	1.906	2	2.092	2.182	2.268	2.352	2.433	2.510
$\frac{C_1}{C} = \frac{1}{b_2}$	0.525	0.500	0.478	0.458	0.441	0.425	0.411	0.398
$\frac{C_2}{C} = b_1 - \frac{1}{b_2}$	1.368	1.500	1.624	1.743	1.854	1.958	2.055	2.148
$\frac{L_1}{R^2C} = \frac{b_2}{b_1 - \frac{1}{b_2}}$	1.393	1.333	1.287	1.252	1.224	1.201	1.184	1.168

Table XIV—Coefficients of Fourth-Order TBT Transfer Functions and the Corresponding Circuit Constants.

m	-0.2	0	0.2	0.4	0.6	0.8	1.0	1.2
b_1	2.481	2.613	2.741	2.864	2.982	3.094	3.201	3.302
b_2	3.213	3.414	3.614	3.814	4.010	4.203	4.392	4.575
b_3	2.507	2.613	2.718	2.822	2.925	3.026	3.124	3.220
$\frac{L_1}{R^2C} = \frac{1}{b_3}$	0.399	0.383	0.368	0.354	0.342	0.330	0.320	0.311
$\frac{C_2}{C} = \frac{b_3}{b_2 - \frac{b_1}{b_2}}$	1.127	1.082	1.043	1.008	0.978	0.951	0.928	0.907
$\frac{C_3}{C} = b_1 - \frac{b_2}{b_2 - \frac{b_1}{b_2}}$	1.353	1.531	1.698	1.856	2.004	2.143	2.273	2.395
$\frac{L_2}{R^2C} = \frac{b_2 - \frac{b_1}{b_3}}{b_1 - \frac{b_3}{b_2 - \frac{b_1}{b_2}}}$	1.643	1.577	1.535	1.508	1.492	1.484	1.481	1.482

Table XV—Coefficients of Fifth-Order TBT Transfer Functions and the Corresponding Circuit Constants.

m	-0.2	0	0.2	0.4	0.6	0.8	1.0	1.2
b_1	3.079	3.236	3.387	3.534	3.673	3.808	3.937	4.060
b_2	4.902	5.236	5.569	5.905	6.235	6.564	6.888	7.206
b_3	4.933	5.236	5.541	5.851	6.159	6.470	6.778	7.085
b_4	3.119	3.236	3.352	3.469	3.583	3.698	3.811	3.923
C_1/C	0.321	0.309	0.298	0.288	0.279	0.270	0.262	0.255
L_1/R^2C	0.928	0.894	0.864	0.836	0.811	0.788	0.767	0.747
C_2/C	1.435	1.382	1.338	1.300	1.269	1.243	1.221	1.203
L_2/R^2C	1.770	1.695	1.656	1.640	1.638	1.646	1.659	1.676
C_3/C	1.323	1.545	1.751	1.945	2.125	2.295	2.453	2.602

The use of Tables XII to XV and Figures 7, 11, 15, and 19 enables one to design a current-driven low-pass filter, interstage network, or a delay line filter. These may be designed for prescribed bandwidth, rise time, overshoot, etc., using high-Q elements. If low-Q circuit elements must be used, the TBT transfer functions may be transformed into new transfer functions by means of the substitution[12] $S = p + d$ where d determines the dissipation in the circuit elements. The synthesis may then be carried out in a manner similar to that shown previously. Storch[13] applied this method for the synthesis of the MFED network with low-Q elements and shows the design procedure for a ninth-order filter.

Stagger-Tuned Band-Pass Amplifiers

Consider now the design of a staggered tuned amplifier with n single-tuned stages designed for a given amount of overshoot. The stagger-tuned amplifier may be designed by use of the data given above. This data may be also used for the design of staggered damped double-tuned circuits.[14,15] Once the location of the poles in the complex frequency plane is known the interstage network may be easily found. The discussion here will be limited to the narrow-band case.

Single-Tuned Stage

The transfer impedance, Z_t, of a current-driven circuit shown in Figure 25 is given by

$$\frac{e_2}{i} = Z_t(p) = \frac{1}{\frac{1}{R} + pC + \frac{1}{pL}} = \frac{1}{C} \cdot \frac{p}{p^2 + \frac{1}{RC}p + \frac{1}{LC}} \tag{29}$$

$$= \frac{1}{C} \cdot \frac{p}{(p - p_1)(p - p_2)},$$

---

[12] S. Darlington, "Synthesis of Reactance Four Poles," *Jour. of Math. and Physics*, Vol. 18, p. 335, September, 1939.

[13] Reference (7), p. 111.

[14] Reference (3), p. 221.

[15] M. M. McWharter and J. M. Pettit, "The Design of Stagger-Tuned Double-Tuned Amplifiers for Arbitrarily Large Bandwidth," *Proc. I.R.E.*, Vol. 43, p. 923, August, 1955.

where $p = j\omega$

$$p_1 = -\frac{1}{2RC} + j\sqrt{\frac{1}{LC} - \left(\frac{1}{2RC}\right)^2} = -\sigma_1 + j\sqrt{\omega_0^2 - \sigma_1^2},$$

$$p_2 = -\frac{1}{2RC} - j\sqrt{\frac{1}{LC} - \left(\frac{1}{2RC}\right)^2} = -\sigma_1 - j\sqrt{\omega_0^2 - \sigma_1^2}. \tag{30}$$

It is seen from Equation (29) that the single-tuned circuit given in Figure 25 has one zero at the origin and two complex conjugate poles given by Equation (30). If this circuit is driven by a pentode having the transconductance g_m, the gain g of the stage will be

$$g = g_m Z_t = \frac{g_m}{C} \cdot \frac{p}{(p - p_1)(p - p_2)}. \tag{31}$$

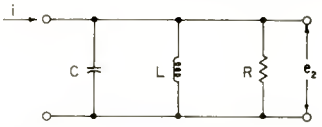

Fig. 25—Single-tuned shunt-loaded circuit.

For circuits having moderate or high Q, the variation of the gain in the pass band near the critical frequency ω_0 of the pole p_1, for all practical purposes, is not affected by the existence of the conjugate pole and the zero at the origin. For the narrow-band approximation, the absolute value of the gain may be written as

$$|g| = \frac{g_m}{C} \cdot \frac{|p|}{|p - p_1| \cdot |p - p_2|} \approx \frac{g_m}{C} \cdot \frac{\omega_0}{|p - p_1| \cdot 2\omega_0} = \frac{g_m}{2C} \cdot \frac{1}{|p - p_1|}, \tag{32}$$

where the following approximations have been made:

$$|p| \approx |j\omega_0| = \omega_0 = \frac{1}{\sqrt{LC}}$$

and

$$|p - p_2| \approx |2j\omega_0| = 2\omega_0,$$

since $\omega_0 \gg \sigma_1$.

Figure 26 shows the location of the poles and zero.

It is seen from Equation (32) that the behavior of the gain in the

pass band may be approximated by considering only a single pole p_1 in the second quadrant. The 3-decibel bandwidth b of the single-tuned stage is[16]

$$b = \frac{1}{2\pi RC}, \tag{33}$$

the center frequency f_0 is given by

$$f_0 = \frac{1}{2\pi \sqrt{LC}}, \tag{34}$$

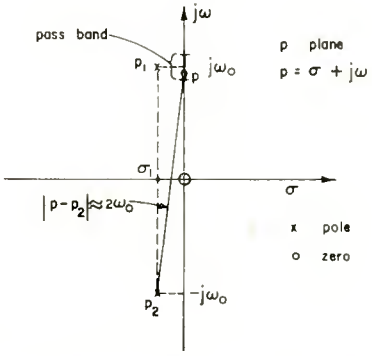

Fig. 26—Location of poles and zero of single-tuned circuit.

and the Q of the tuned circuit is

$$Q = \frac{R}{\omega_0 L} = \frac{f_0}{b} = R\sqrt{\frac{C}{L}}. \tag{35}$$

The "gain–bandwidth" of a single tuned circuit is found by multiplying the center frequency gain g_0 times the bandwidth b as defined in Equation (33).

The center frequency gain is

$$g_0 = |g|_{p=j\omega_0} = \frac{g_m}{2C} \cdot \frac{1}{|j\omega_0 - \sigma - j\omega_0|} = \frac{g_m}{2C} \cdot \frac{1}{\frac{1}{2RC}} = g_m R, \tag{36}$$

[16] Reference (3), p. 168.

so that the gain–bandwidth product is

$$g_0 b = g_m R \cdot \frac{1}{2\pi RC} = \frac{g_m}{2\pi C}. \tag{37}$$

n Cascaded Stages

If n stages are cascaded, each having the same transconductance g_m and shunt capacity C, the absolute value of the total gain G is given by

$$|G| = \prod_{k=1}^{n} |g_k| = \left(\frac{g_m}{2C}\right)^n \prod_{k=1}^{n} \frac{1}{|p - p_k|}. \tag{38}$$

The poles may now be arranged in the p plane to give the desired response.

If we drive a narrow-band-pass amplifier by a unit stepped carrier at the center frequency of the amplifier, f_0, the envelope of the output will be the same as the unit step response of the low-pass analog.[17] The transfer function of the low-pass analog of the band-pass filter will have the same pole arrangement around the origin as the transfer function of the band-pass system has about the center frequency, f_0. It is this relationship between the low-pass and band-pass systems that enables us to use the low-pass data given for the design of band-pass amplifiers.

Gain–Bandwidth Factor

The gain–bandwidth factor (GBF) of an amplifier is defined as

$$\text{GBF} = \frac{(\text{over-all gain})^{1/n} \times \text{over-all bandwidth}}{g_m/2\pi C}. \tag{39}$$

It has been shown[18] that the GBF of a stagger-tuned maximally flat (Butterworth poles distribution) n-uple is 1. After giving the design procedure it will be proved that the GBF of a staggered tuned n-uple having TBT pole distribution is $2\pi\underline{B}$, the normalized 3-decibel bandwidth.

Design Procedure

Let g_m, C, total center frequency gain G_0, and the bandwidth B of the desired amplifier be given, and the amount of overshoot restricted

[17] Reference (3), chapter 7.
[18] Reference (3), p. 179.

to $\gamma/100$ or less. The over-all center-frequency gain is found from Equation (39) to be

$$G_0 = \left(\frac{g_m}{2\pi C} \cdot \frac{\text{GBF}}{B} \right)^n = \left(\frac{g_m}{2\pi C} \cdot \frac{2\pi \underline{B}}{B} \right)^n. \tag{40}$$

Equation (40) involves two unknown variables $\underline{B}$ and n. For a given overshoot, $\underline{B}$ does not vary appreciably with the number of stages (see Figures 7, 11, 15 and 19). After n is chosen, m and $\underline{B}$ are found from these figures for a given amount of overshoot.

With a chosen value n, different values of m and $\underline{B}$ may be found for the n^{th} order filter, depending on the amount of overshoot selected. Since n is an integer, the chosen value of n may result in too large an over-all gain, whereas the next smaller value of n may give too low a gain for the specified design criteria. In this case the value of n resulting in the larger gain is chosen and a smaller overshoot is selected so that the gain requirement is satisfied.

We next find the location of the poles in the normalized p plane by use of Tables IV, VI, VII, and X. These poles satisfy the relation given by Equation (2) which can be written as

$$\prod_{k=1}^{n} |p_k| = \prod_{k=1}^{n} |\sigma_k + j\omega_k| = 1 \tag{41}$$

where σ_k and ω_k are normalized values and are found in the tables as the real and imaginary parts of p_k.

The 3-decibel bandwidth of this pole arrangement is $\underline{B}$. In order to make the angular bandwidth unity as for the Butterworth case we multiply the poles by $1/2\pi\underline{B}$. A Butterworth pole distribution will have the bandwidth B if the poles are located on a circle of radius πB. To make the center frequency of the amplifier f_0, all the poles are shifted to the upper half of p plane by the amount $j\omega_0$. The location of the poles will therefore be

$$p_k = 2\pi \frac{B}{2} (\sigma_k + j\omega_k) \cdot \frac{1}{2\pi \underline{B}} + j2\pi f_0 \tag{42}$$

where σ_k and ω_k are as specified in Equation (41). Each pole represents a single-tuned circuit which has a center frequency f_k given by

$$f_k = f_0 + \frac{B}{2} \omega_k \cdot \frac{1}{2\pi \underline{B}}. \tag{43}$$

The 3-decibel bandwidth of each tuned circuit is

$$b_k = \frac{B}{2\pi \underline{B}} (-\sigma_k) \tag{44}$$

since the real part of Equation (42) is equal to π/Q.

To find L_k and R_k we use Equations (34) and (35) which give

$$L_k = \frac{1}{(2\pi f_k)^2 C}, \tag{45}$$

where C is the total interstage shunt capacity.

The resistance is given by

$$R_k = 2\pi f_k L_k \cdot \frac{f_k}{b_k} = \frac{4\pi^2 f_k^2 L_k \underline{B}}{(-\sigma_k) B}, \tag{46}$$

where f_0 in Equation (35) has been replaced by the center frequency of the k^{th} stage, f_k.

GBF of the Amplifier

In the above design procedure, use was made of the equation GBF $= 2\pi \underline{B}$. We shall now prove this equality. The over-all gain at the center frequency as seen from Equation (38) is

$$|G_0| = \left(\frac{g_m}{2C}\right)^n \prod_{k=1}^{n} \frac{1}{|j2\pi f_0 - p_k|} = \left(\frac{g_m}{2C}\right)^n \prod_{k=1}^{n} \frac{1}{\left|\frac{B}{2} \cdot \frac{1}{\underline{B}} (\sigma_k + j\omega_k)\right|} \tag{47}$$

$$= \left[\frac{g_m}{2C} \cdot \frac{1}{\frac{B}{2} \cdot \frac{1}{\underline{B}}}\right]^n \prod_{k=1}^{n} \frac{1}{|\sigma_k + j\omega_k|} = \left[\frac{g_m}{2C} \cdot \frac{\underline{B}}{\frac{B}{2}}\right]^n,$$

where use was made of Equations (42) and (43).

The gain-bandwidth factor from Equations (39) and (47) is

$$GBF = \frac{|G_0|^{\frac{1}{n}} B}{\frac{g_m}{2\pi C}} = \frac{\frac{g_m}{2C} \cdot \frac{\underline{B}}{\frac{B}{2}} B}{\frac{g_m}{2\pi C}} = 2\pi \underline{B}. \tag{48}$$

The gain–bandwidth factor of a staggered TBT amplifier with n single-tuned stages is seen to equal $2\pi\underline{B}$ given in Figures 7, 12, 15, and 19.

Table XVI—Steady State Equations for MFA and MFED Networks.

CHARACTERISTIC	MFA NETWORK	MFED NETWORK
NORMALIZED TRANSFER ADMITTANCE	$\left[Z(p)\right]^{-1} =$ $\prod_{k=0}^{\frac{n}{2}-1} \left[p - \exp\, j(1 \pm \frac{2k+1}{2n})\pi\right]$, n even; $\prod_{k=1}^{\frac{n-1}{2}} \left[p - \exp\, j(1 \pm \frac{k}{n})\pi\right]$, n odd	$\left[Z(\underline{p})\right]^{-1} =$ $\frac{2^n n!}{(2n)!} \sum_{k=0}^{n} {}_nd_k\, \underline{p}^k$ where ${}_nd_k = \frac{(2n-k)!}{2^{n-k}\,(n-k)!\,k!}$
NORMALIZED AMPLITUDE RESPONSE	$T(\omega) = \left\lvert\left[Z(p)\right]^{-1}\right\rvert = (1+\omega^{2n})^{-\frac{1}{2}}$	$T(\underline{\omega}) = \left[\frac{{}_nh_0}{\sum_{k=0}^{n} {}_nh_k\, \underline{\omega}^{2k}}\right]^{\frac{1}{2}}$ where ${}_nh_k = \frac{(2n-k)!\,(2n-2k)!}{k!\left[(n-k)!\right]^2 2^{2(n-k)}}$
NORMALIZED PHASE ANGLE	$\theta(\omega) =$ $-\sum_{k=0}^{\frac{n}{2}-1} \tan^{-1} \frac{\omega - \sin(1 \pm \frac{2k+1}{2n})\pi}{-\cos(1 \pm \frac{2k+1}{2n})\pi}$, n even; $-\sum_{k=0}^{\frac{n-1}{2}} \tan^{-1} \frac{\omega - \sin(1 \pm \frac{k}{n})\pi}{-\cos(1 \pm \frac{k}{n})\pi}$, n odd	$\theta(\underline{\omega}) =$ $\sum_{k=0}^{\frac{n-1}{2}} {}_nd_{2k+1}\, \underline{\omega}^{2k+1} \Big/ \sum_{k=0}^{\frac{n-1}{2}} {}_nd_{2k}\, \underline{\omega}^{2k}$, n odd; $\sum_{k=0}^{\frac{n}{2}-1} {}_nd_{2k+1}\, \underline{\omega}^{2k+1} \Big/ \sum_{k=0}^{\frac{n}{2}-1} {}_nd_{2(k+1)}\, \underline{\omega}^{2(k+1)}$, n even
NORMALIZED ENVELOPE DELAY	$t_e =$ $\sum_{k=0}^{\frac{n}{2}-1} \frac{-\cos(1 \pm \frac{2k+1}{2n})\pi}{\omega^2 - 2\omega \sin(1 \pm \frac{2k+1}{2n})\pi + 1}$, n even; $\sum_{k=0}^{\frac{n-1}{2}} \frac{-\cos(1 \pm \frac{k}{n})\pi}{\omega^2 - 2\omega \sin(1 \pm \frac{k}{n})\pi + 1}$, n odd	$\underline{t}_e = \left[1 + \frac{1}{\sum_{k=0}^{n} {}_nh_k\, \underline{\omega}^{2k}}\right]^{-1}$

n = order of network.
$p = j\omega RC$, C is adjusted to make normalized MFA bandwidth unity.
$\underline{p} = j\underline{\omega} = j\omega R\Sigma C_t$, ΣC_t = sum of all shunt capacitances in ladder network.

Conclusion

It has been shown that a TBT filter has a unit-step response with less overshoot than that for the MFA filter of the same order when the parameter m is greater than zero. The rise time is less than that for the corresponding MFED filter when m is less than unity. In general, the TBT networks have steady-state and transient characteristics which lie between those for the MFA and MFED networks. All

possible characteristics between those for the MFA and MFED networks can be obtained by making the variable parameter m continuous. With the parameter m equal to zero, the MFA characteristic is obtained; and when m is unity, the MFED characteristic results. When the value of m is less than zero, the corresponding filter has a greater bandwidth and overshoot than the MFA network. With the parameter m greater than unity, filters with little or no overshoot result. Design data has been given which enables one to synthesize a low-pass filter or a staggered-tuned band-pass amplifier with the TBT characteristic.

Acknowledgments

The work embodied in this paper was conducted under the guidance of Professor W. H. Boghosian of the University of Pennsylvania and M. S. Corrington of the RCA Victor Television Division. The authors also wish to acknowledge the excellent work done by Mrs. R. Johnson who programmed and carried out the computations on the IBM "650" computer.

A LINEAR-LOGARITHMIC AMPLIFIER FOR ULTRA-SHORT PULSES

By

Harry Kihn and William E. Barnette

RCA Laboratories,
Princeton, N. J.

Summary—*This paper describes a compact five-stage logarithmic–linear amplifier having an over-all bandwidth of 180 megacycles centered at 180 megacycles and a total dynamic range of 67 decibels. The input signal required for 0.2 volt output from the last stage detector in the linear mode is approximately 700 microvolts of 100 per cent modulated carrier at 180 megacycles. The amplifier input impedance is matched to a 170-ohm line to within ±1 decibel over a 200-megacycle bandwidth to allow operation from a remote wide-band preamplifier. Additionally, a video amplifier of 90 megacycles bandwidth and 28 decibels gain feeding two parallel matched 170-ohm transmission lines and driven by the "log-lin" amplifier is described. Means are included for i-f amplifier gating and for various blanking signals into the video amplifier. A novel method of continuous signal detection and wide-band video time delay have been incorporated in the amplifier system. Furthermore, descriptions of developmental wide-band frequency sweep, video, and ultra-short-pulse generators are included. The amplifier system may be useful in airborne millimicrosecond pulse radar, multiple channel television, and for nuclear pulse amplification.*

Introduction

With the increasing importance of high-resolution systems, the need arose for high-gain, low-noise, wide-band amplifiers for both i-f and video amplification in a superheterodyne receiver. The effectiveness of performance of these amplifiers in faithfully reproducing pulses as short as 10 millimicroseconds, with a dynamic range extending from signals of the order of fluctuation noise to 50 or 60 decibels greater, determined to a large extent the usefulness of the system.

Although there is considerable literature dealing with the design of amplifier systems of large dynamic range, these designs did not venture beyond the use of .1 microsecond wide pulses. If the pulse width is decreased by an order of magnitude, a number of new problems appear. Tubes, techniques, nonlinear devices, and center frequencies which can be successfully applied in narow-bandwidth systems, no longer are applicable or must be considerably modified. The gain–bandwidth criterion decrees low-impedance, low-Q circuits which limit the effective dynamic range of nonlinear devices such as crystal diodes.

More complex circuit configurations must be used to optimize the gain for a given bandwidth. Provision must also be made to insure adequate r-f filtering of the second-detector load circuit without deteriorating the video amplifier response.

A previously published paper[1] described a lightweight wide-band amplifier capable of amplifying 10-millimicrosecond pulsed signals on a 170-megacycle carrier, having 130-megacycle bandwidth, 80 decibels gain, and a noise factor of 5.5 when operating from a crystal mixer of 360-ohm source impedance. This amplifier used a "cascade chain" configuration of high G_m triodes with a stagger-damped circuit arrangement incorporating permeability-tuned elements. This also included a 75-megacycle wide video amplifier of 28 decibels gain which fed two high-mu sharp-cutoff developmental cathode-ray tubes. This amplifier served as the starting point of the logarithmic amplifier described here.

The basic limitation in the above linear amplifier was that if the gain control was set to see pulses of the order of fluctuation noise, pulses greater than 25 decibels above this level were limited and clipped thus severely deteriorating the "highlight" or strong-signal resolution. Furthermore, the minimum time constant in the grid circuit was not low enough to prevent masking of weak signal following extremely strong ones. These shortcomings plus the extra circuit complexity and poorer signal/noise performance inherent in a high-resolution system tended to severely limit the utility of such a high-resolution system.

A survey was made of the several known means of increasing the dynamic range of the amplifier system with the provision that the system response would allow receiver recovery 20 millimicroseconds after the cessation of a very strong pulse to allow proper amplification of weak pulses immediately following strong ones. The three most promising are

1. Instantaneous automatic gain control;
2. Prescribed time varying gain control;
3. Logarithmic, or the constant incremental system.

In the instantaneous a-g-c, which is similar to the commonly used carier a-g-c, an attempt is made to maintain individual pulses or groups of pulses at the same level at the second detector, independent of input signal level. Because of the 20-millimicrosecond recovery requirement, the feedback circuit to control gain would require bandwidths of the order of 50 megacycles, thereby severely aggravating the filtering

[1] Harry Kihn, "A Wide Band Low Noise Amplifier for Millimicrosecond Pulses," presented at Aerborne Electronics Conference, Dayton, Ohio, May 9, 1955.

problem of the feedback control voltage with consequent amplifier instability. Although this method is very useful in narrow-band systems, it was not deemed feasible in high-gain amplifiers for 10-millimicrosecond pulses.

Prescribed time varying gain control may be used in applications where the target signal return amplitude varies in a known manner as a function of time. A gain control voltage having the inverse function of time compared to the above may be applied to one or more amplifier grids to maintain, on the average, a constant signal at the second detector. In radar this is the well known sensitivity–time control which tends to equalize the disparity in signal strength from nearby and distant objects. This does *not*, however, solve the problem of variable target scattering cross section at a given range which may have a variation of 50 decibels. Since there is no precise means of predicting the nature of reflecting objects, no useful method is available to present saturation of strong signals adjacent in time to weak ones. This method therefore may aid in reducing the dynamic range required but does not basically solve the problem.

The most desirable signal input–output characteristic is one that never completely saturates on strong signals, yet allows weak signals to be seen in noise. This is attained by the use of an amplifier whose output approximates the logarithm of the input. In this case the incremental amplification at any signal level is inversely proportional to the signal level. This implies that the same percentage fluctuation can be seen at all signal levels. This may be expressed as:

$$dE_{\text{out}} = \frac{K\, dE_{\text{in}}}{E_{\text{in}}},$$

therefore,

$$E_{\text{out}} = K \ln E_{\text{in}} + E_0.$$

This type of amplifier therefore allows the instantaneous compression of large pulses while simultaneously providing the gain necessary for amplifying signals of the order of fluctuation noise. This is the amplifier type described in this paper.

Types of Logarithmic Amplifiers

The three most useful methods of providing a log characteristic in an amplifier will now be examined.

The Impedance Variation Method

This uses nonlinear impedances, Z, as circuit loading in tandem

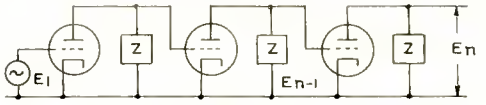

Fig. 1—Amplifier chain using nonlinear plate circuit impedances as the logarithmatizing elements.

amplifier stages, a method which has been extensively used.[2] These impedances have a general expression $Z_k = f(K/E_{in})$ and are adjusted by d-c bias and padded by linear resistance to result in a logarithmic characteristic over a considerable dynamic range.

Figure 1 shows an amplifier chain using nonlinear plate circuit impedances as the logarithmatizing elements. Figure 2 shows the impedance variation as a function of voltage. If it is assumed that $Z = Z_0/(1 + E_s/E_0)$ is the law of variation of nonlinear dynamic impedance, where Z is the average impedance over an r-f cycle, Z_o is the impedance at zero or small signal amplitudes, and E_s is the instantaneous signal amplitude across Z, the following relationships may be derived:

$$E_n = E_{n-1}\, G_m\, Z = E_{n-1}\, G_m \frac{Z_o}{1 + \dfrac{E_{n-1}}{E_0}}.$$

Since only low values of Z are being considered because of the great bandwidth, the tube gain may be expressed as $G_m Z$ even for triodes. It is evident that as $E_{n-1}/E_0 \rightarrow 0$, $E_n = G_m\, Z_0$, which is the normal linear amplifier gain. However as E_{n-1}/E_0 becomes greater than 1 and approaches the value of $G_m\, Z_0$ (which may have values of 3 to 10 in many wide-band amplifiers), then $E_n \rightarrow E_{n-1}$ and the gain of the last stage approaches 1.

Figure 3 shows a family of input–output curves for a varying

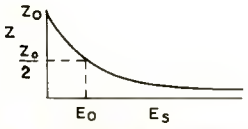

Fig. 2—Impedance variation as a function of voltage for the nonlinear impedances of Figure 1.

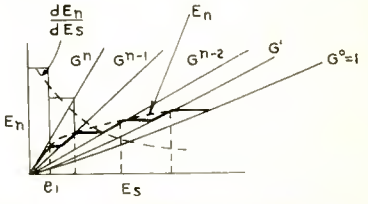

Fig. 3 — Input-output curves for various numbers of stages using the impedance-variation method.

[2] R. V. Alred and A. Reiss, "An Anti-Clutter Radio Receiver," *Jour. Elec. Engrg.*, Vol. 95-3, p. 459, November, 1948.

number of stages from 1 to n. For small signals of the order of r-m-s noise, the over-all receiver gain is G^n where G is the small-signal stage gain and n is the number of stages. From the above discussion it is evident that as E_s, the input signal, increases from thermal noise to e_1 at which the last-stage gain approaches 1, the input–output relationship shifts to the G^{n-1} curve as shown by the solid line. As E_s further increases, the shift continues to G^{n-2}, etc., until the amplifier has an over-all gain of 1. Since the variation in Z is not in discrete steps but is quite gradual, the E_n versus E_s curve is more like the dotted curve. By suitably adjusting the Z versus E_s law by bias and resistive padding, the gain slope may be made to approach the relation:

$$\frac{dE_n}{dE_s} = \frac{K}{E_s}, \quad \text{(shown in Figure 3)}$$

and

$$E_n = K \ln E_s + E_0$$

which is the desired relationship.

Continuous Detection and Addition Method

In this system the amplified r-f signal is detected in every stage or sequence of stages, each of which has a well-defined limiting level, and the filtered video signals are summed up with suitable time delay to produce an output which approximates the desired law.

Figures 4a and 4b show typical amplifier chains using the above principle. In Figure 4a, the voltage at the plate or grid circuit of each stage is limited, detected, and fed into a common R_0 by suitable delay networks such that the delay of the detected signal as it passes from stage l to stage n just compensates the i-f band-pass stage delay. This insures that all the detected pulses will coincide to produce one composite pulse approximating in shape the original pulse. It should be noted that not only must the average phase slope (time delay) be the same for the i-f and video channels, but also their variation in time delay with frequency. The latter condition insures that all components of the pulse will add up properly to produce the desired result. This becomes a serious problem for very wide bandwidths as will be shown later in the discussion of the time-delay requirements. In Figure 4a, grid leak detection and limiting may be used in place of separate detectors and limiters. Plate detection in an auxiliary tube and crystal or thermionic diodes may similarly serve the purpose of limiting and detection.

Figure 4b shows an alternative scheme in which the tubes V_i to V_n are back biased to provide automatic limiting and plate detection, with

the detected output taken across Z_k, the cathode impedance.[3] In a similar fashion to the above, the detected signal is delayed sequentially to insure complete superposition of the pulses from all the stages.

Figure 5 shows a plot of the detection characteristic of a typical 5-stage continuous-detection log amplifier. It is evident that amplifier input signals of the order of noise, e_0, will produce output only in stage 5, signals near e_a will produce output from stages 4 and 5, etc.,

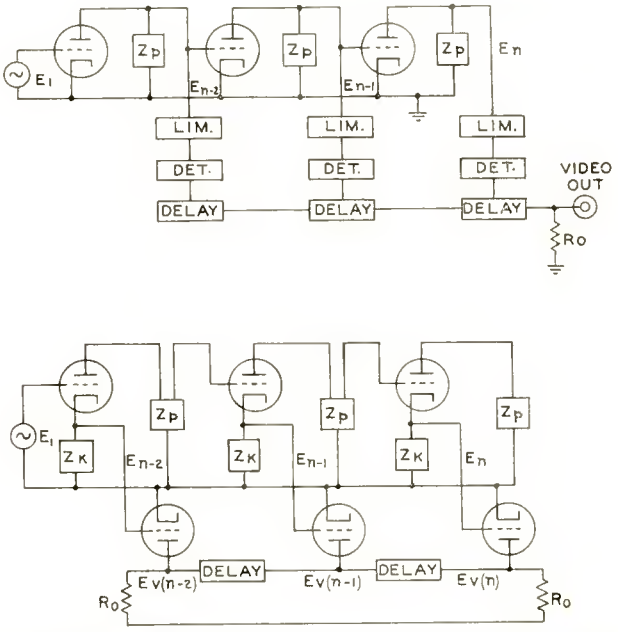

Fig. 4—Amplifier chains using the continuous-detection and addition method.

until at e_d all five stages are feeding signals across R_0. This is illustrated in Figure 6 for a cosinusoidal shaped pulse.

Referring to Figures 5 and 6, input signals of the order of e_0 have the full gain of the amplifier $E_n = G^n e_0$, but at e_a the output is E_L, the limiting level per stage, plus $G^{n-1} \Delta e_a$, where Δe_a is the increment of e_a beyond the $(n-1)$ stage intercept. It is evident that for input signals of the order of e_d, the output is

$$E_n = nE_L + G\Delta e_d.$$

If we let $E_L = e_L G$, then $E_{n(\log)} = NGe_L + G\Delta e_d$, the output of the nth

[3] T. H. Chambers and I. H. Page, "The High Accuracy Logarithmic Receiver," *Proc. I.R.E.*, Vol. 42, p. 1307, August, 1954.

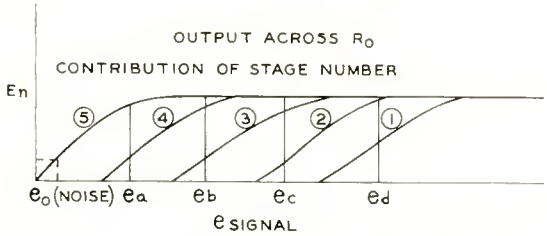

Fig. 5—Detection characteristics of a typical 5-stage continuous-detection log amplifier.

stage. If we had a linear amplifier in place of the above and fed an input signal $e_L + \Delta e_d$ into the amplifier, then $E_{n(\text{lin})} = (e_L + \Delta e_d)G^n$. If the number of stages become large for a given over-all gain, and the limiting levels are identical in each stage, then the linear and continuous-detection amplifier gains may be written

$$\frac{E_n}{e_L}(\text{lin}) = KG^n,$$

$$\frac{E_n}{e_L}(\log) = nG + K.$$

It is evident that the expression of the latter is the logarithm of the former. For the amplifier described here, $n = 5$ which value is somewhat low for true logarithmic amplification to be attained. Due to slight nonlinearities between limiting levels, the resulting characteristic is quite adequate for purposes of instantaneous a-g-c of a 10-millimicrosecond amplifier. The added complexity of a larger number of stages was proved to be unnecessary.

Nonlinear Feedback Method

This method uses the nonlinear characteristic of crystals or diodes to control the feedback factor of an amplifier, and may take the form

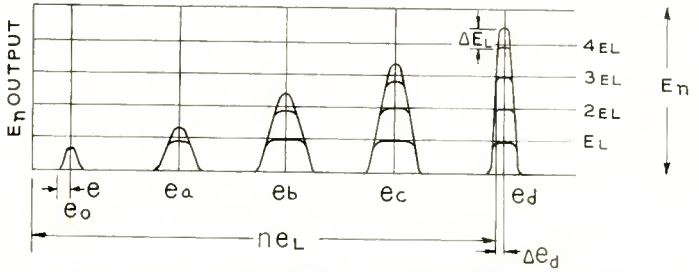

Fig. 6—Signal addition for a cosinusoidal-shaped pulse.

of either variable cathode degeneration or nonlinear plate-to-grid feedback. This method is primarily useful for low-frequency narrow-band-pass amplifiers and video amplifiers, but is not suited for the 180-megacycle bandwidth required per stage. Figure 7a shows a possible arrangement of the cathode feedback[4] and Figure 7b of a plate-feedback amplifier. In the former, the effective cathode degeneration is controlled by signal level such that the cathode impedance increases with signal, hence reducing the effective gain. In the latter

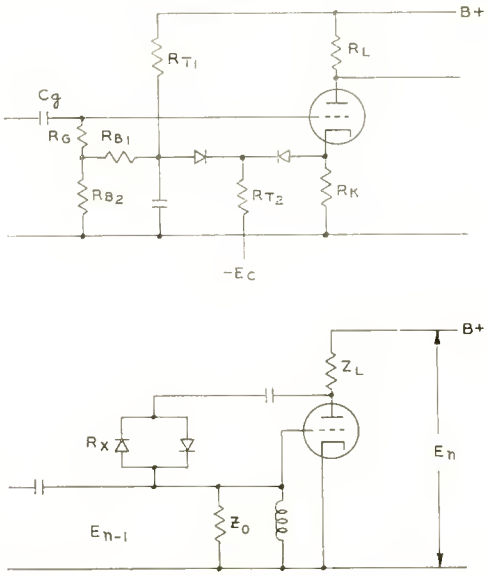

Fig. 7 (a)—Cathode-feedback system for the nonlinear feedback method; (b)—Plate-feedback system for the nonlinear feedback method.

the negative feedback ratio $(-Z_0/[R_x + Z_0])$ is increased by the reduction of R_x with increasing signal level. When $R_x >> Z_0$ (low signal) the feedback is essentially zero. When $R_x << Z_0$ then the feedback provides a unity stage gain. The result is therefore similar to that of the two methods previously described.

Wide-Band Prototype Amplifier

Figure 8 shows a spectrum plot of the pulse to be used in the system. This is approximately a cosine-shaped pulse as shown by the points plotted according to a cosine law. From an analysis of the pulse

[4] W. E. Ayer, "Video Amplifiers With Instantaneous AGC," Electronic Research Laboratories, TR No. 4, Stanford University, Calif.

shape and the system noise bandwidth it was concluded that 130 megacycles was the optimum over-all bandwidth for the best signal-to-noise ratio. To further optimize the S/N ratio the amplifier input circuit should be the limiting parameter in bandwidth consideration, since this would allow maximum mixer crystal impedance transformation into the first tube grid circuit. All subsequent circuits must be wide enough not to materially reduce this bandwidth. From a consideration of the bandwidth shrinkage factor, S for n stagger-damped pairs of circuits $S = [2^{1/n} - 1]^{1/8}$ and the need of six or seven

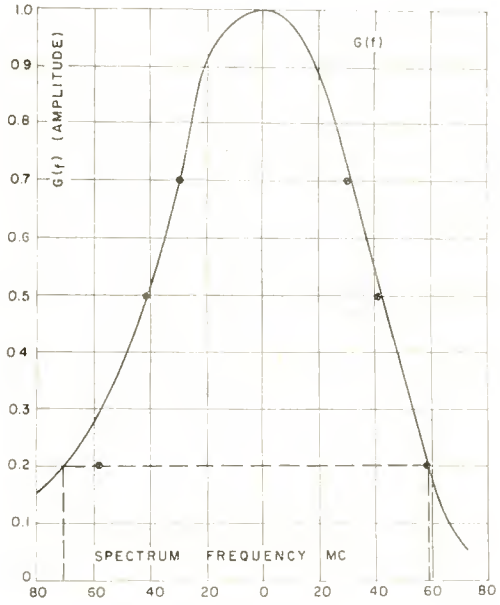

Fig. 8—Spectrum plot of a pulse for the system.

pairs ($n = 6$ or 7) to produce the 75-decibel gain required, a single-stage bandwidth of 180 megacycles or greater was deemed necessary. The 75-decibel gain is needed to amplify crystal mixer noise to approximately 0.2 volt r-m-s for efficient second-detector operation.

The success of the linear "cascade-chain" amplifier[1] in providing maximum gain–bandwidth of all the practical lightweight amplifier arrangements investigated, led to the use of a modification of this amplifier for the equipment described herein. For this reason a brief description of this linear prototype is included. Figure 9 shows an early version of a stagger-damped, multiple tuned, cascade-chain circuit

incorporating cathode inductance compensation. The advantage of single-loaded stagger-damped circuits over single-tuned synchronous circuits and even transitionally coupled stages may be realized by the comparison of the gain–bandwidth factors shown below.[5]

	Gain–Bandwidth
(1) m synchronous single-tuned circuits	$(2^{1/m} - 1)^{1/2}$
(2) m transitionally coupled double-tuned circuits with equal Q's	$\sqrt{2}\,(2^{1/m} - 1)^{1/4}$
(3) m transitionally coupled double-tuned circuits, one-side loading	$2\,(2^{1/m} - 1)^{1/4}$
(4) m stagger-damped doubles with single-loaded double-tuned circuits	$2\,(2^{1/m} - 1)^{1/8}$

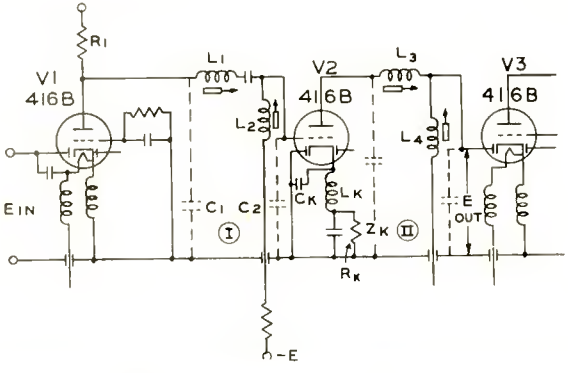

Fig. 9—Early version of a stagger-damped, multiple-tuned cascade-chain circuit incorporating cathode-inductance compensation.

If $m = 1$ (for a single stage) then (3) and (4) have a 6-decibel improvement and (2) affords a 3-decibel improvement over single-tuned circuits. It is evident too that (4), the stagger-damped circuit, although having the same gain–bandwidth factor as (3), has a lesser bandwidth compression than the transitionally coupled case for large values of m. The price paid for these desirable features in (4) is the greater circuit complexity and more critical adjustments required. In Figure 9, circuit I was used as the overcoupled stage since R_1, which is the only loading on the circuit, could be adjusted to produce the required Q. Circuit II is loaded by the input impedance of the grounded grid tube, $V3$, which is approximately 20 ohms, $(Z_i = (Z_L + R_p)/$

[5] G. E. Valley, Jr. and H. Wallman, *Vacuum Tube Amplifiers*, Radiation Laboratory Series, Vol. 18.

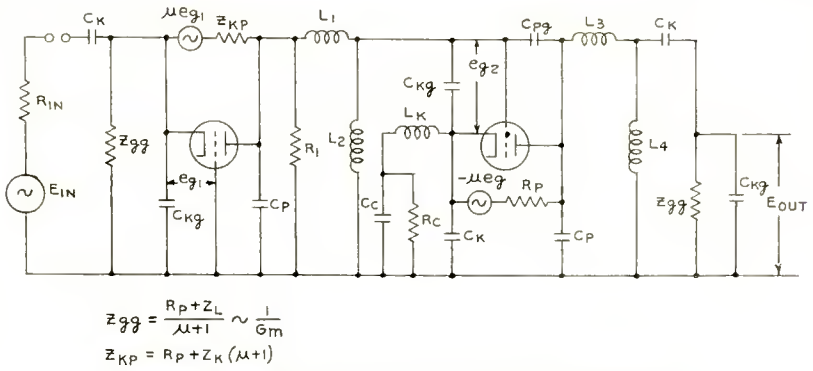

Fig. 10—Equivalent circuit of prototype amplifier.

$(\mu + 1) \approx 1/g_m$) hence is inherently a low-Q circuit. The equivalent circuit of Figure 9 is shown in Figure 10.

Because the shell-to-cathode capacitance C_k of the 416B triode used resonates within the pass band with the cathode lead inductance, L_k, thus seriously deteriorating the response due to cathode degeneration, a compensation circuit L_k, C_k, R_k has been included. The equivalent circuit and response are shown in Figure 11. The gain of this circuit is

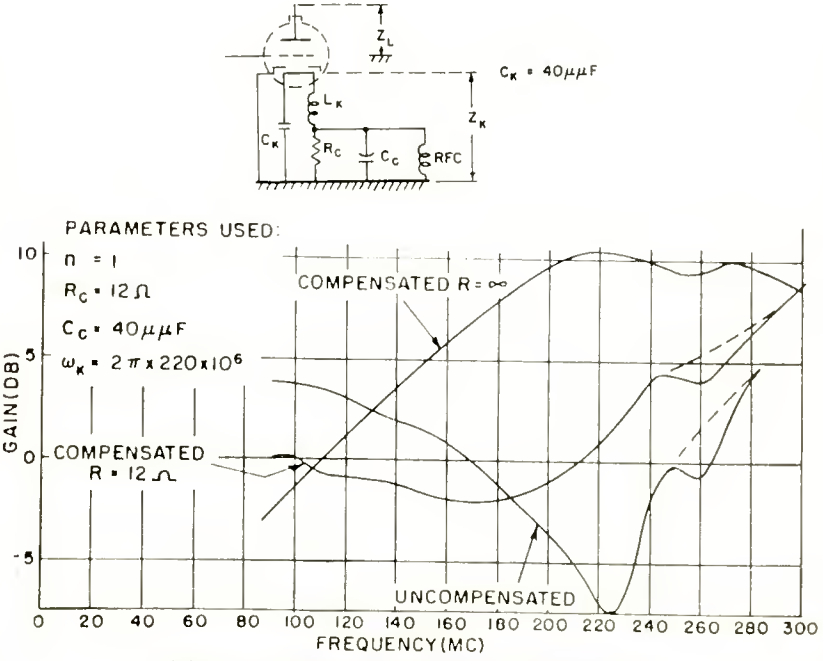

Fig. 11—Cathode inductance compensation.

$$\text{gain} = \frac{G_m Z_L}{1 + G_m Z_k},$$

where

$$Z_k = \frac{R_c - j\left\{p^5 naR_c - p^3\left[(2+n)\,aR_c - x_k\right] + p\left[\left(\frac{1+n}{n}\right)aR_c - x_k\right]\right\}}{p^6a^2 + p^4\left[1 - 2\left(\frac{1+n}{n}\right)a^2\right] + p^2\left[\left(\frac{1+n}{n}\right)^2 a^2 - 2\right] + 1},$$

$$n = \frac{C_c}{C_k},$$

$$p = \frac{\omega}{\omega_k},$$

$$\omega_k = \frac{1}{[L_k C_k]^{1/2}},$$

$$a = R_c C_c \omega_k,$$

$$x_k = \omega_k L_k.$$

C_k and R_k have been selected to produce a slightly rising gain-versus-frequency characteristic which compensates for increased input loading to produce an over-all response which is quite flat over the pass band. The responses of several stages are shown in Figure 12. However, due to the considerable variation in 416B triode characteristics, a modification of the circuit of Figure 9 was used in the log amplifier prototype circuit. This is shown in Figure 13.

From a comparison of Figures 9 and 13 it is seen that R_1 has been moved to the grid side of L_1 in circuit I and C_3 and C_4 have been added in circuit II. With R_1 directly *across* the grid of V_2, the possibility of V_2 oscillating (caused by positive feedback through C_{pg}) when L_1 and L_2 are detuned, has been eliminated. This change also places the low-Q circuit on the grid side so that circuit variations due to grid input loading for changes in 416B tubes are minimized. The addition of a small amount of damping, R_4, across L_1 produces a flatter over-all response. C_3 is a vernier primary tuning means, while C_4 allows the adjustment of secondary Q in circuit II with varying input impedance and shell capacity of the 416B. This secondary circuit is effectively a series resonant circuit in this modification, such that with 416B input resistances of the order of 20 ohms, Q's of one or

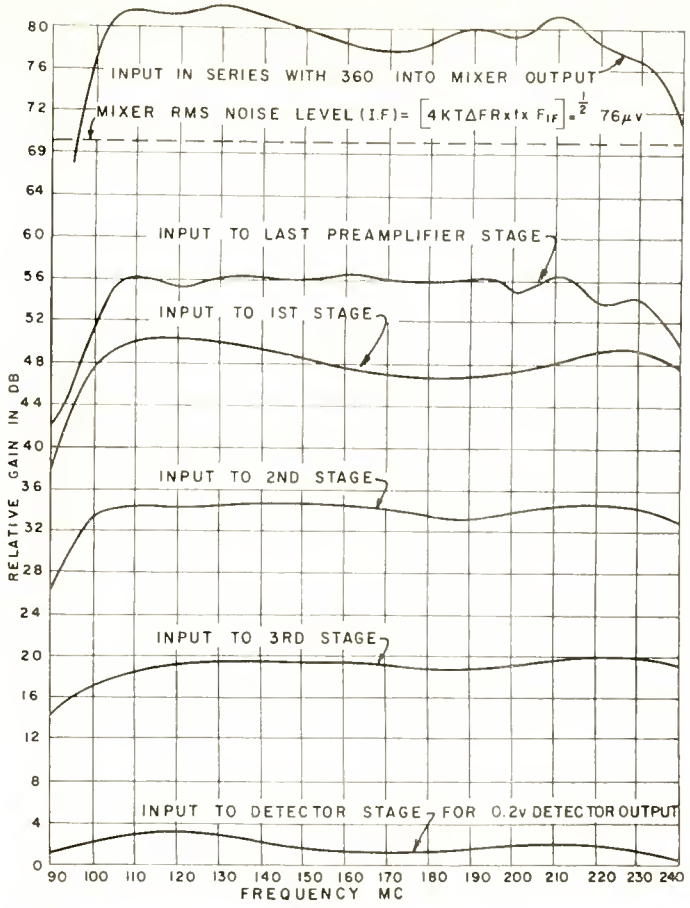

Fig. 12—Response of cascade-chain amplifier using prototype stages of Figure 9.

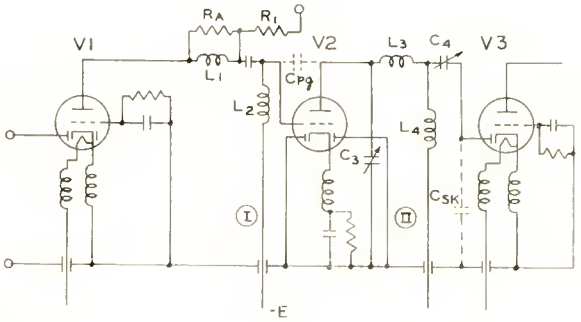

Fig. 13—Modified cascade-chain amplifier stage.

more can be attained. The effective shunt Q for C_{sk} in parallel with $1/g_m$ is of the order of 1/4 to 1/2, which is too low for effective staggered damping circuitry.

Figure 14 shows the frequency responses for several stages of the prototype logarithmic amplifier. The insertion gain per stage varies from 13 to 15 decibels with replacement of 416B tubes. The bandwidth is at least 180 megacycles and can be aligned to 200 megacycles with normal care.

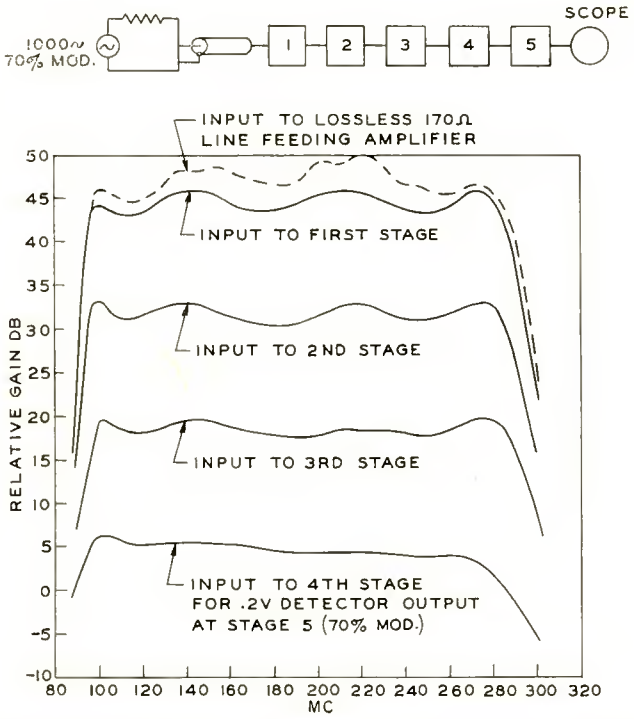

Fig. 14—Frequency responses for several stages of the prototype amplifier (linear mode).

As indicated previously, several methods of logarithmatizing were considered. The earliest and simplest was the impedance variation method using two stages of grounded-grid amplification, synchronously tuned, using back-to-back 1N72 germanium crystals. Compression ratios of up to 10 decibels were attained, but the gain–bandwidth was poor as is characteristic of synchronous single-tuned stages. This illustrated, however, that the 1N72 was a useful nonlinear element in the UHF region and was suitable for use in the log amplifier. For band-

widths under 100 megacycles, this configuration might be useful. By using double-tuned circuitry in the above amplifier, a small-signal gain of 5 decibels gain and 160 megacycles bandwidth per tube were attained. To maintain proper band-pass shape at all levels of signals required not only equal Q circuits in the primary and secondary but also two pairs of back-to-back crystals which must have quite well-defined laws of resistance variation. This arrangement was found to depend too critically on crystal and tube parameters, hence other avenues were investigated. Figure 15 shows a schematic diagram and the response of a single-tuned test circuit using back-to-back 1N72 germanium crystal diodes. Figure 16 shows a schematic circuit diagram of a double-tuned grounded-grid circuit and oscillograms of the output voltage for various circuit parameters. The latter tests were made by simulated resistance to simplify the observed frequency characteristic variation to attain 10 decibels or more of amplitude compression. It may be noted that oscillogram A would represent weak-signal and oscillogram I, strong-signal operation. To maintain suitable band pass for intermediate values of R_1 and R_2 required very precise control of these values. Since the 416B tube input impedance is low (20 ohms), placing realizable nonlinear resistance across this element is useless for amplitude control.

Attempts to secure increased gain–bandwidth with cascade-chain circuits resulted in 14-decibel, 160-megacycle amplifiers, but again the tracking problem was formidable. The use of the above as a bandwidth-determining element and a separate single-tuned crystal-loaded nonlinear element showed some promise, but required additional tubes with only 10-decibel compression ratios per 3 tubes.

The use of feedback nonlinear amplifiers was then briefly considered. Available crystal diodes are too high impedance even at strong signals to be placed directly in the cathode circuit, and experience with the cathode compensation circuit for the 416B showed that oscillation would result from the presence of leads as short as 1/2 inch in the cathode circuit if the grid circuit were suitably tuned. Since oscillation might damage a tube beyond repair, this approach was not further investigated.

The use of feedback from plate to grid by means of back-to-back crystals results in the addition of at least 3 to 5 micromicrofarads which, at 280 megacycles, is sufficient to cause oscillation unless heavy grid damping is used with consequent reduction in gain–bandwidth. The difficulty of controlling the phase of the feedback over such a wide frequency range mitigated against the use of this type of logarithmatizing.

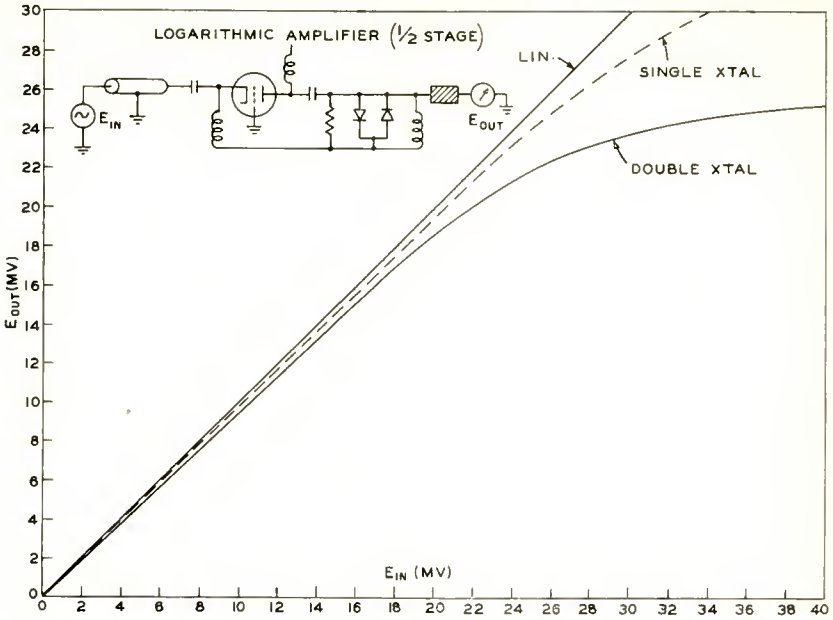

Fig. 15—Schematic and response of a single-tuned circuit for testing 1N72 germanium crystal diodes.

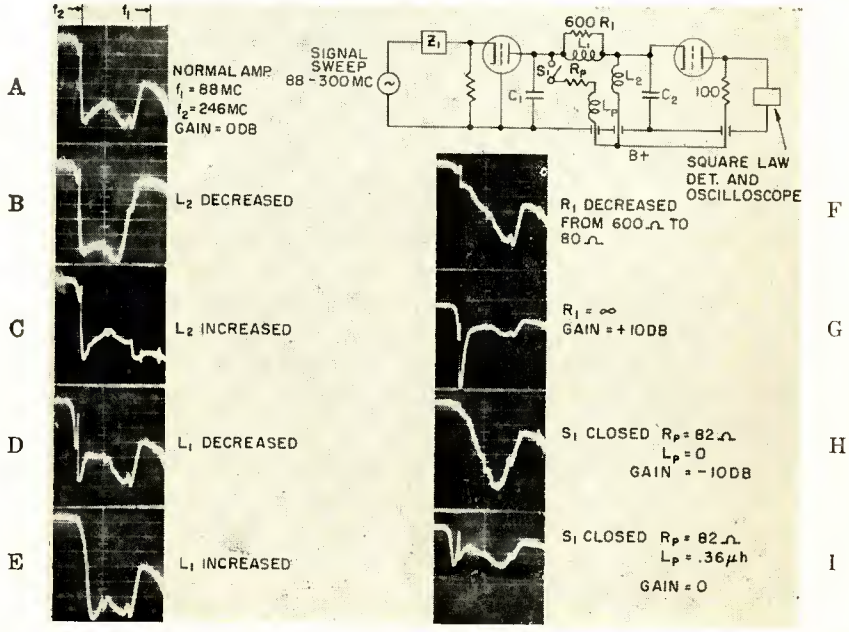

Fig. 16—Schematic and oscillograms of a double-tuned grounded-grid circuit (oscilloscope gain settings are shown).

As a result of the above considerations the continuous detection method was deemed most practical for the wide-band amplifier described here. The method of back-biased tube detection was considered first since this results in the simplest type of amplifier. Because the grid bias of each stage must be adjusted for optimum detection as well as straight-through gain, this results in a stage loss of about 5 to 6 decibels over optimum biasing for gain alone. Since in the system considered amplification of signals of the order of fluctuation noise was important and since gains per stage of only 14 decibels could be realized at the extremely wide bandwidth needed, this loss was a serious drawback. Furthermore there were no pentodes available with a gain–bandwidth factor comparable to that of the 416B triode, so that grounded-grid stages or cascade-chain stages must be used. Because the input impedance of the grounded-grid tube varies with grid voltage, double-tuned circuits become asymmetric with strong signals and indeed the cascade-chain amplifier may oscillate if the loading effect of the grounded-grid tube in its plate circuit were reduced. In addition, placing a broad-band impedance in the cathode circuit of the 416B operating over the range of frequencies required, leads to amplifier instability.

Grid-leak detection was also considered, but this involves too long time constants and poor video response if efficient detection is desired. The system finally evolved was the continuous detection method using 1N82 crystals as detectors which feed a nonlinear load consisting of two 1N72 crystals in parallel as shown in Figure 17. This is seen to consist of a modified wide-band cascade-chain amplifier prototype with a 1N82 crystal detector capacitatively coupled to the shell of V_2 and feeding two 1N72 crystals in parallel with a band-stop filter. These are directly coupled to the grid of a 6AK5 isolation amplifier which is connected to a lumped-circuit negative mutual delay line described later. The virtue of this arrangement lies in that the detector is connected across the low input impedance of V_2, and hence has a negligible effect on the band-pass characteristic. Therefore signals passing directly through the amplifier are not distorted, regardless of their level. The 68-micromicrofarad capacitor tends to equalize the slight difference between the straight-through response and the detector circuit branch response shown in Figure 18. The 1N82 is biased for optimum detection sensitivity and the 1N72's are biased both for minimum compression threshold and best compression ratio. These settings are not very critical and hence only one set of controls are used for all five channels. Smoother logarithmic response would, however, result if all channels were individually controlled.

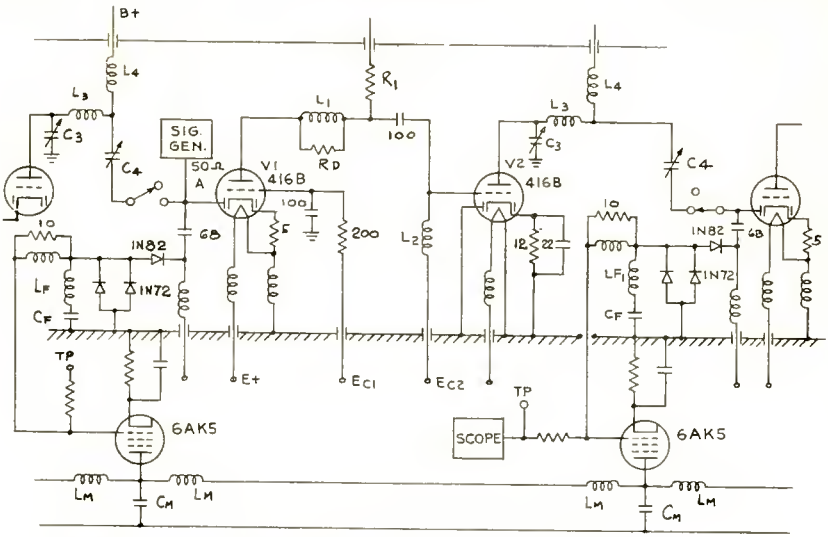

Fig. 17—Continuous-detection-method log amplifier prototype.

Several circuit configurations were tried before arriving at that shown in Figure 17. The first was the use of back-to-back 1N72 crystals capacitance-coupled to the 1N82 detector to simulate an a-c nonlinear load for the detector with short time constant decay. This was found to produce only about 5 decibels of compression and required relatively large signals for threshold of operation. By removing the coupling

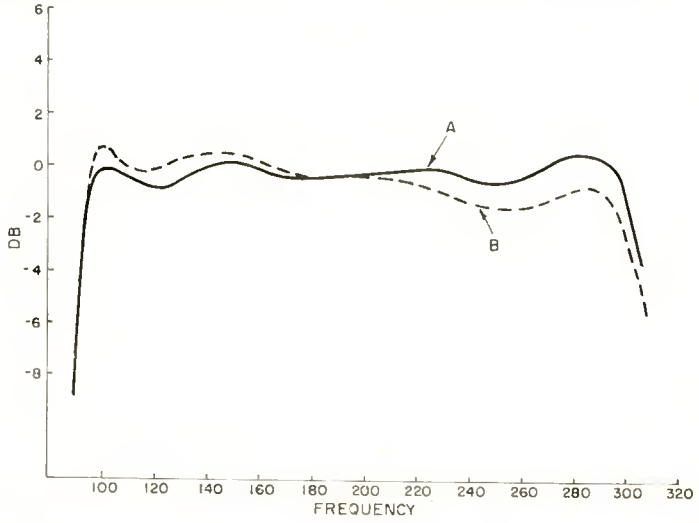

Fig. 18—Normalized response of straight-through circuit (A) and branch circuit (B) (linear mode).

condenser, the average component of the detected pulse increased the effective change in crystal impedance and resulted in a 12-decibel compression. It was seen that under this condition the back-to-back arrangement was only effective as a symmetrical load for weak signals, since the d-c component which reduced the crystal resistance in one direction, raised the resistance of the other crystal to the point where

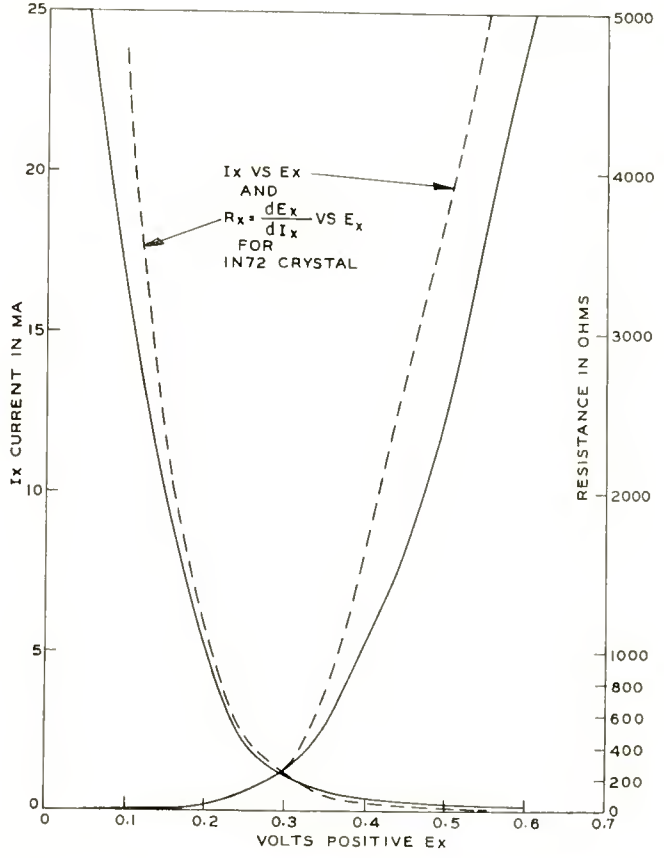

Fig. 19—Current–voltage and resistance–voltage characteristics for two representative 1N72 crystals.

it was nonconducting. To further increase the range of compression the two crystals were paralleled and compression ratios of 16-20 decibels were attained with available signal drive. Figure 19 shows a plot of I_x and $R_x = dE_x/dI_x$ versus E_x for two representative 1N72 crystals. It is evident that dR_x/dE_x, or resistance slope, is greatest for the higher values of R_x. However, from considerations of video bandwidth require-

ments, the maximum allowable value of R_x was 300 ohms for the given circuit capacitance. The use of two crystals each biased to produce $R_{x_0} = 600$ ohms will produce a greater change with a given ΔE_x than a single crystal as biased at 300 ohms because of the greater slope at high values of R_x. Since it is desired to initiate and attain maximum compression at the lowest signal possible, two crystals were paralleled and biased to result in a 300-ohm dynamic resistance as mentioned above.

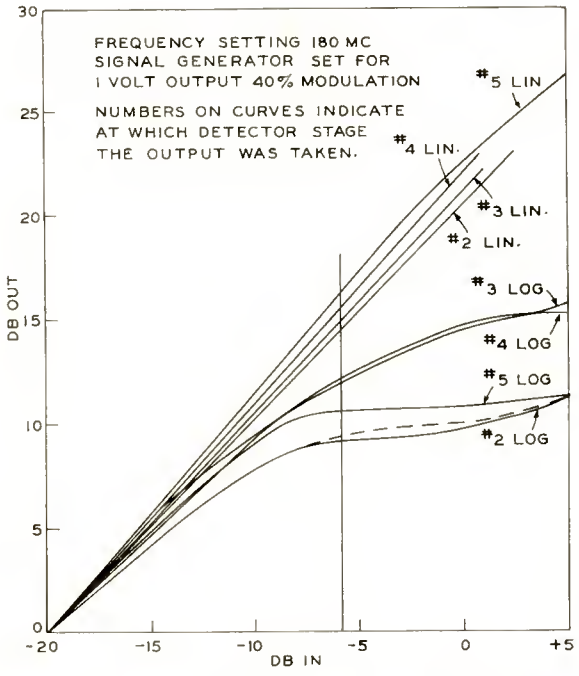

Fig. 20—Saturation characteristics of the log amplifier.

Several curves of linear (resistive detector load) and compressive (nonlinear crystal load) operation for various channels of the amplifier are shown in Figure 20. These curves were taken with the circuit of Figure 17 using a 40 per cent sine-wave-modulated 180-megacycle signal input at A and a calibrated scope at B for the maximum available input range. It may be seen that channel 5 produces 16 decibels compression which is limited only by the amplitude of the available signal. Care was taken that, with these steady-state strong signals, the delicate grids of the 416B were not permanently damaged. Subsequent results (Figures 38-40) show a 20-decibel compression ratio by the

use of pulsed test signals which simulate the basic function of the amplifier more realistically without danger of tube burnout.

The lesser compression ratio of channels 3 and 4 are primarily due to poorer 1N72 crystals. Proper selection and distribution of crystals and individual bias controls among the several channels could be advantageously used to produce a desired output–input relationship. Only limited crystal selection was deemed necessary in this amplifier, which produced about 2 decibels spread of the knee of the saturation curve with a median value of 15 decibels compression. It is desirable that the knee occur after conduction has begun in the previous stage so as to produce a smooth transition with increasing input signals. Since the stage gain is about 14 or 15 decibels, this criterion is barely attained. It would be desirable to have more stages of logarithmatizing if extreme logarithmic accuracy were desired. The added complexity and increased number of crystals and vacuum tubes mitigated against their use in the amplifier. Dynamic tests showed that the addition of all the sequential stage pulses produced a smooth over-all pulse as shown in Figure 40.

An interesting phenomenon was observed during the saturation tests. In Figure 21, if the shunt filter $L_f C_f$ were removed, increased compression resulted, so much so that at very strong signals the saturation curve had a negative slope as shown by the dashed curves. This produces a slight valley in the output pulse. The cause of this is the detection of the residual r-f pulse at the detector output by the 1N72 crystals with reversed polarity, which tends to cancel the video pulse resulting from detection by the 1N82 detector crystal. This accounted for some unusually large compression ratios which had been measured with inadequate bypassing. A slight amount of back detection is evident in the curve of Figure 20, but this is insignificant in determining the over-all appearance of the pulse. It does serve to insure that the saturation curve does not continue to rise with signal level.

Since the bypass filter is a one-pole network with a resonant frequency at 180 megacycles, frequencies at the edges of the amplifier pass band would tend to produce a back-detection effect. As is evident from the pulse spectrum of Figure 8, frequencies around 180 megacycles predominate, and upon detection in the proper (1N82) crystal tend to instantaneously shift the operating point of the 1N72 to a lower impedance condition, which is also a poorer operating point for detection. Hence in a practical embodiment of pulse amplification, no downward droop of the saturation characteristic was observed. A separate test involving a 180-megacycle carrier and a smaller-amplitude 120-mega-

cycle side-band frequency showed greatly reduced back detection in the presence of the 180-megacycle signal.

This effect could have been completely eliminated by the use of a 2- or 3-pole filter or by the use of a balanced detector feeding the 1N72 crystals. Since the effect was not apparent under any conceivable operating condition, the added complexity was not warranted.

Referring to Figure 17, it may be noted that the 1N72 crystal non-

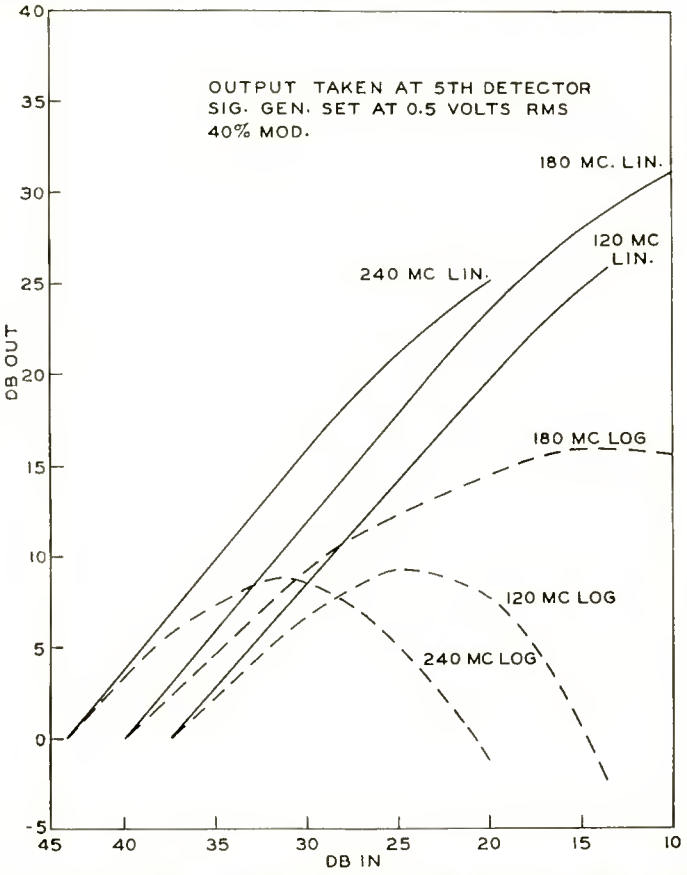

Fig. 21—Saturation characteristics of the log amplifier with L_f and C_f removed.

linear load is d-c coupled to the grid of the 6AK5. Had a large enough capacitor been used for a-c coupling to provide good-low frequency video response (1,000 cycles), the time constant of the grid circuit would have been too great for pulse-to-pulse instantaneous compression particularly if the possibility of drawing grid current on a very strong pulse signal were considered. By using d-c coupling, the instantaneous

detection currents which serve to cause 1N72 crystal load-impedance compression may operate within one pulse duration after the incidence of a strong pulse. No stretching of the pulse trailing edge has been observed in simulated dynamic tests.

Wide-Band Delay System

As described previously, the detected signals from the several stages must be added into a common load so as to form a single composite pulse. The requirements for the summation circuit are two-fold. First it must have adequate bandwidth so as to reproduce faithfully all the pulse spectral components, and secondly the delay between stages must be identical to that of the i-f amplifier stage both in average delay and in that of its major frequency components. Bode[6] has shown that there is a direct correspondence between the amplitude response of a filter and the envelope time delay of a signal passing through it, so that if the exact amplitude response of a stage can be measured over all practical frequencies (theoretically over an infinite frequency range) the phase characteristic can be plotted, and from this the time delay derived. Bode's method has been improved on by Murakami and Corrington.[7]

The plotted i-f stage time delay can be matched against the known curves of envelope delay for a low-pass filter having adequate bandwidth to transmit all important sidebands of the pulse properly. In such an arrangement the detected envelope of a pulsed carrier passing along a low-pass delay line will keep pace with the signal through the i-f amplifier.

When this approach was attempted, certain practical difficulties arose. An analysis of the method will bring out the fact that the major contribution to the *average* phase shift is due to the amplitude slope at the skirts of the i-f selectivity curve, far removed from the 3-decibel attenuation frequencies. Because of 416B overloading, inadequate signal generator output, and detector frequency response this approach proved impractical. It was also aggravated by the presence of poles outside the pass band (such as that due to the cathode compensation circuit) which tended to mask the asymptotic amplitude–frequency slope needed to calculate the phase response. Because of these limitations another approach was used. This involved an extension of the

---

[6] H. W. Bode, "Network Analysis and Feedback Amplifier Design," D. Van Nostrand Company, Inc., N. Y., 1945.

[7] T. Murakami and M. S. Corrington, "The Relation Between Amplitude and Phase in Electrical Networks," *RCA Review*, Vol. IX, p. 602, December, 1948.

"Band-Pass Low-Pass Analogy"[8] to the time domain, namely that a band pass amplifier which is symmetrical in amplitude about a frequency in the pass band in an *arithmetic manner* ($A_{(\omega_0-\omega_1)} = A_{(\omega_2-\omega_0)}$) will have the same time delay as a direct-coupled low-pass amplifier of the same amplitude response and ½ the bandwidth of the i-f amplifier. This may be more evident by considering that the carrier in the process of detection in a double-sideband system translates the various spectral components about itself so as to superimpose them upon their corresponding elements in a $(\omega_0 - \omega)$ or $(\omega - \omega_0)$ manner. The change of sign of phase shift above and below the carrier frequency provides the necessary sign correction for the superposition process. To the extent that the attenuation slopes on the high and low frequency cutoffs are identical and the symmetry of the response in the pass band about ω_0 is maintained, the band-pass and low-pass delays are identical. The problem then is to design a low-pass amplifier whose pass band and cutoff slope is approximately the same as the measured i-f characteristic.

Figure 22 shows the wide-band delay line used in the summation circuit and oscillograms of the amplitude response when the input was shifted from A to F. This is a negative mutual filter having the equivalent circuit of Figure 23. The theoretical delay characteristics for various coefficients of coupling are shown in Figure 24.[9] It is evident that the delay is most constant over the pass band for a coupling corresponding to $m = 1.4$. The provision of adjustable mutual coupling in each stage allows the equalization of delay for slightly different i-f bandpass characteristics in corresponding stages. This is synonymous with adjustment of the bandwidth and steepness of amplitude response of the low-pass delay line to match the i-f response. Figure 25 shows the plotted amplitude responses of the various line sections of Figure 22, starting with section 5 alone, 4 and 5, 3, 4 and 5, etc. The 3-decibel bandwidth is at least 100 megacycles. This width was provided so as not to attenuate the higher-frequency components of the detected pulse beyond the amount lost in the i-f amplifier. To compensate for the slightly decreased delay resulting from the increased bandwidth, the cutoff slope was made slightly steeper than that of the i-f amplifier, as shown in Figure 26. This represents the i-f amplitude response of stage No. 5 alone (curve *A*) and both 4 and 5 (curve *B*) and a plot of the corresponding low-pass curves of Figure 25 placed

[8] V. D. Landon, "The Band-Pass Low-Pass Analogy," *Proc. I.R.E.*, Vol. 24, p. 1582, December, 1936.

[9] E. L. Ginzton, W. R. Hewlett, and J. H. Jasberg, "Distributed Amplification," *Proc. I.R.E.*, Vol. 36, p. 956, August, 1948.

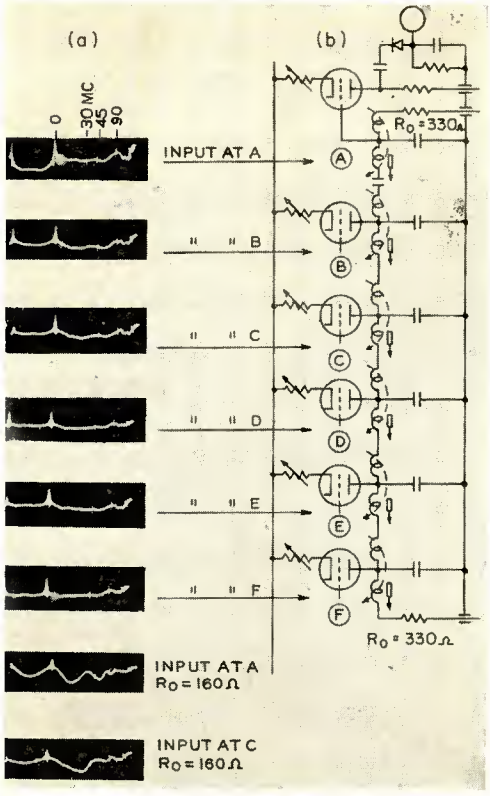

Fig. 22—Frequency response of summing delay line.

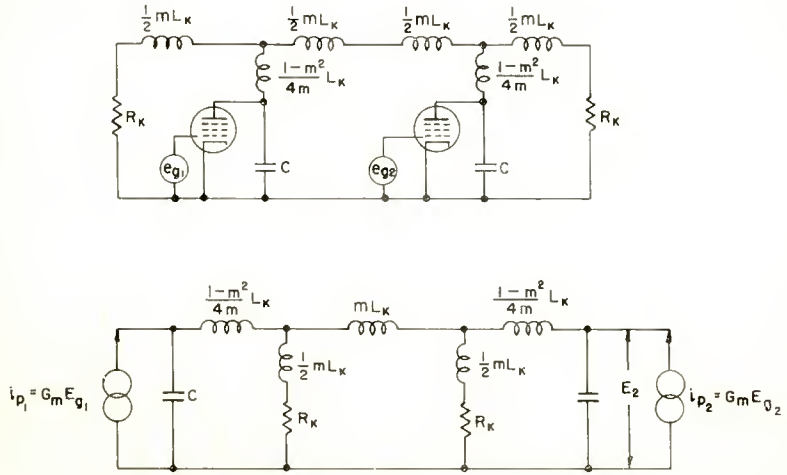

Fig. 23—Equivalent circuit of summing delay line.

symmetrically about $\omega_0 (= 2\pi \times 184 \times 10^6)$. Curves A' and B' are seen to be wider than the corresponding i-f curves, but have slightly steeper slopes. The photographs of the superimposed detected pulses to be discussed later (Figure 40) indicate that the delay compensation was quite adequate for the particular radar purpose for which the amplifier was designed. For more precise requirements such as ranging and computer use or for rectangular pulses the point-by-point method of Bode might be justified. It should be noted that *small* perturbations

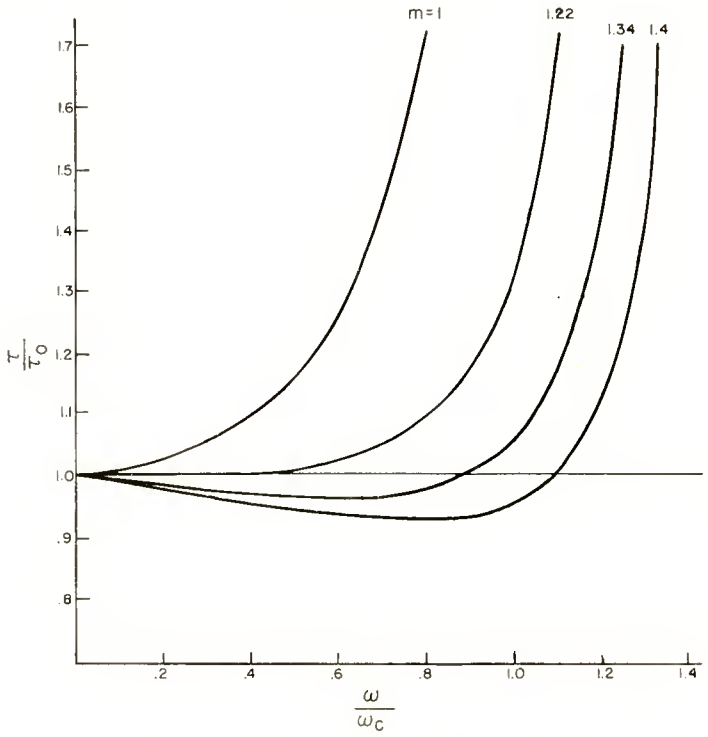

Fig. 24—Relative time delay versus coupling factor, m, for the negative mutual delay line.

in the amplitude response in the pass band do not materially affect the over-all delay, but do introduce a slight "dispersion" in the frequency components of the pulse.

As shown in Figure 22b, the simplified schematic circuit diagram of the delay line, provision is made to adjust the gain of the individual amplifiers feeding the line so as to allow variation in tubes and slight differences in i-f stage gains.

Figure 27 shows a schematic diagram of the wide-band log amplifier.

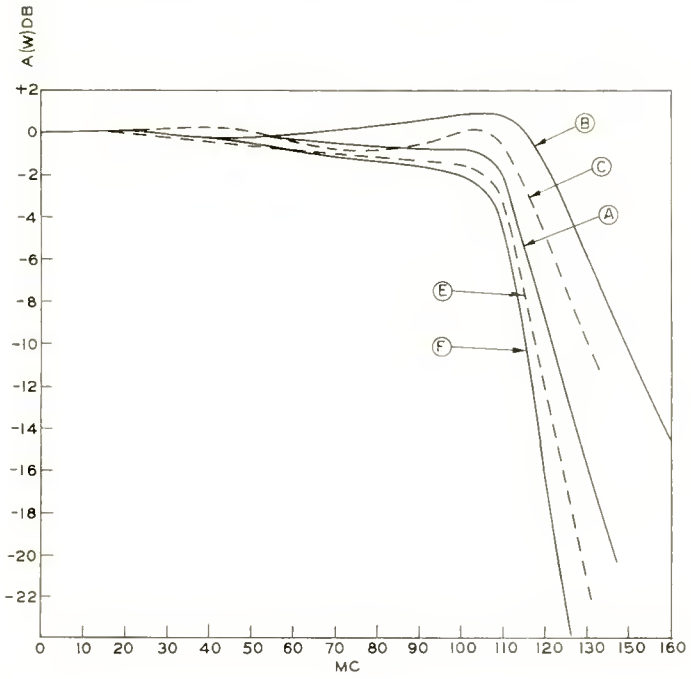

Fig. 25—Amplitude response of the summing delay line.

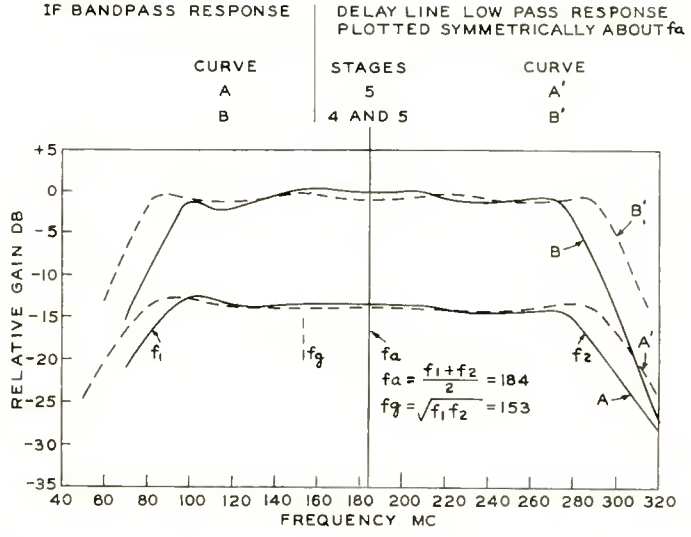

Fig. 26—I-F bandpass response and delay line low-pass response.

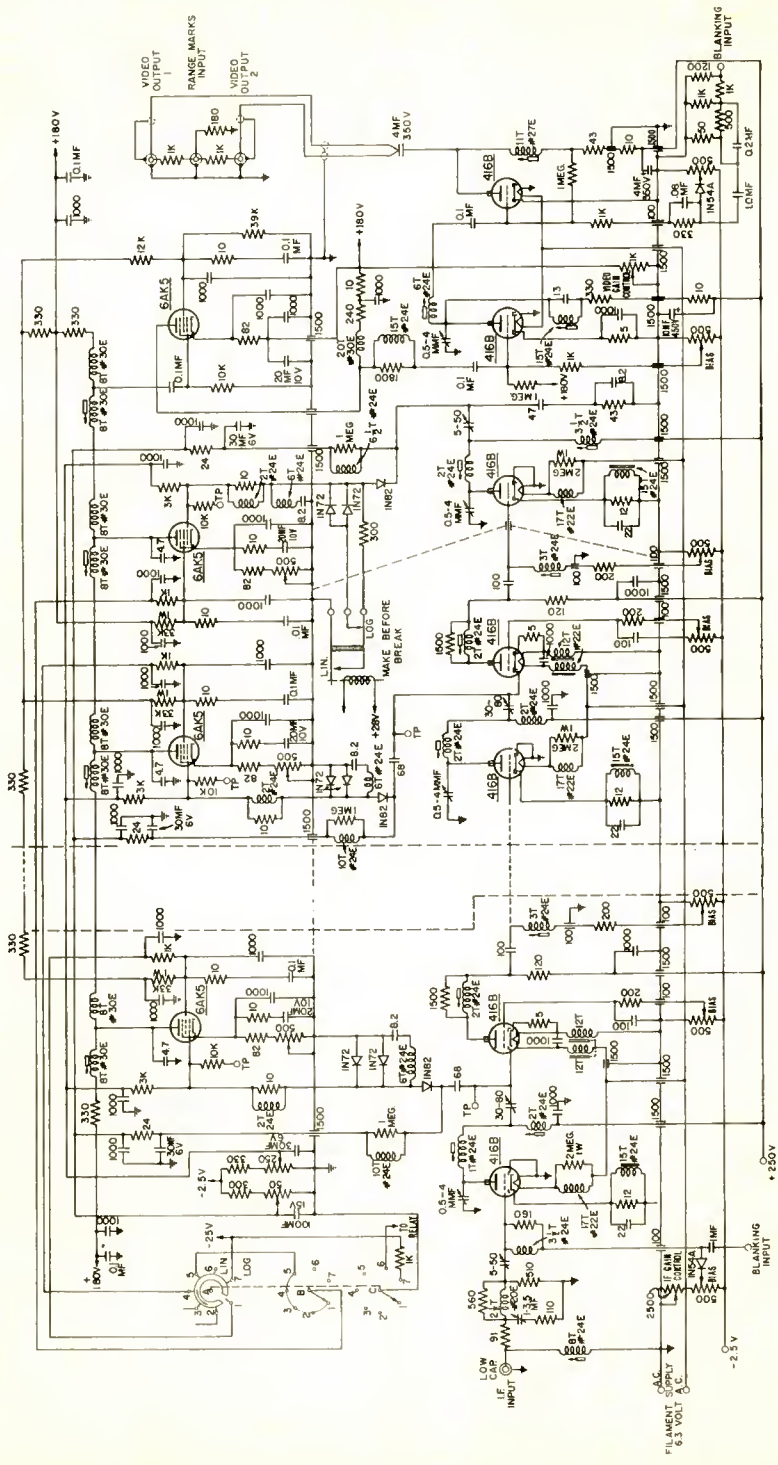

Fig. 27—Schematic wideband logarithmic amplifier (two prototype stages omitted).

The various i-f stages are numbered (1), (2), etc., and the corresponding delay line sections located at the top of the figure are (1^1) (2^1), etc. In the i-f stages the even-numbered tubes V_4, V_6, etc., are the grounded-cathode stages and the odd-numbered tubes, V_5, V_7, etc., are the grounded-grid stages. Component details have been included to provide design data.

At the input to V_4 there is a combined 170-ohm transmission line matching network and optimum transfer network into the tube input impedance. The circuit arrangement and frequency response of the network fed from 20 feet of 170-ohm cable are shown in Figure 28. This is considerably more complex than the network of the linear wide-

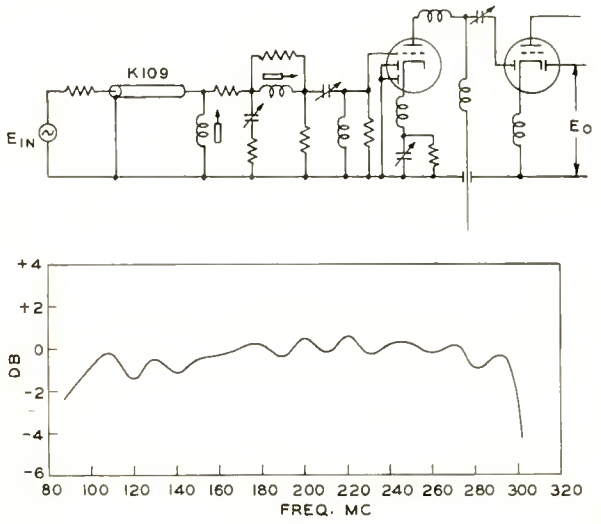

Fig. 28—Circuit arrangement and normalized transfer response of the log amplifier input circuit.

band amplifier previously described[1] and results in adequate match from 90 to 290 megacycles compared to the 130 megacycles attained therein.

The problem of designing a matching network was very real since the log amplifier was to be fed by a cable from a remote pre-amplifier which served to provide about 30 decibels of gain from the crystal mixer. It is evident that the input impedance must be resistive within approximately 10° over the pass band to provide a 200-megacycle match as shown, hence a dissipative network was used to allow less critical tuning adjustments. One preamplifier which was to be used with the log amplifier is shown in Figure 29.

To allow direct comparison of signals linearly or logarithmically amplified, a remotely driven switch, S_1 of Figure 27, is located in the housing of stage 5. This substitutes a 300-ohm resistor for the 1N72 crystal nonlinear load and simultaneously biases negatively the screens of the summing 6AK5, except for tube No. 23. Other positions of switch S_1 allow the viewing of the outputs of each stage by itself (positions 1 to 5) and the summed or log output in position 7.

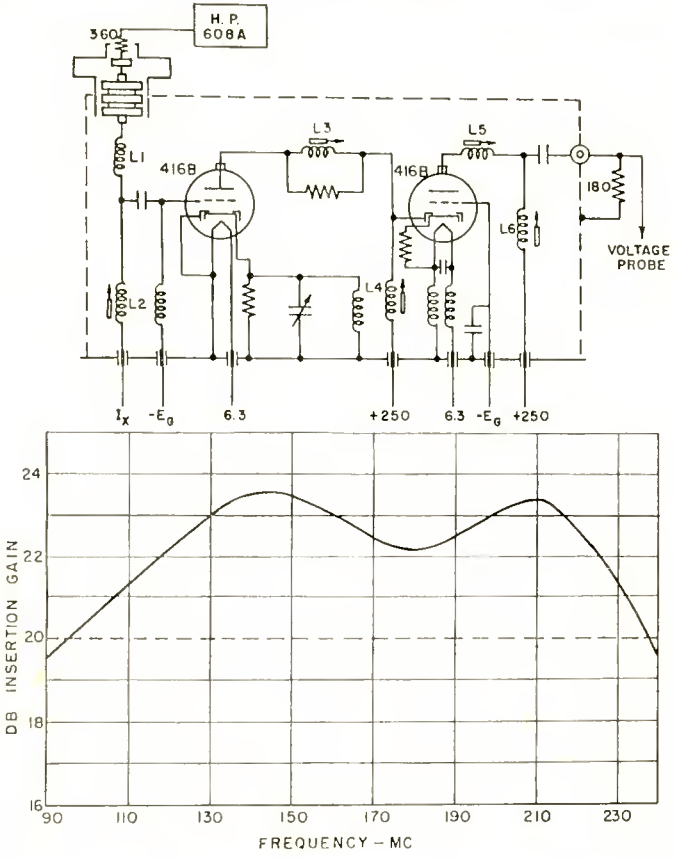

Fig. 29—Preamplifier for the log amplifier.

Due to the considerable variation in 416B tube characteristics, switch S_2 allows the individual adjustment of tube currents to 30 milliamperes.

Wide-Band Video Amplifier

At the right-hand side of Figure 27 schematic diagram is a wide-band video amplifier consisting of V24 (6AK5) summing amplifier

driving two 416B's, V13 and V14, both operating as grounded-cathode amplifiers. Because V14 was to feed two channels interconnected by 170-ohm cables, the plate impedance of 85 ohms results in a stage gain of 4. By carefully controlling the reactive elements and matching of the far end of the line, positive feedback through C_{pg} resulted mainly in increase in input capacitance according to the relation

$$\Delta C_i = C_{pg}\, G_m\, Z_L \cos\theta$$
$$\approx 4.2\, C_{pg},$$

where θ = load phase angle.

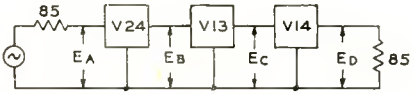

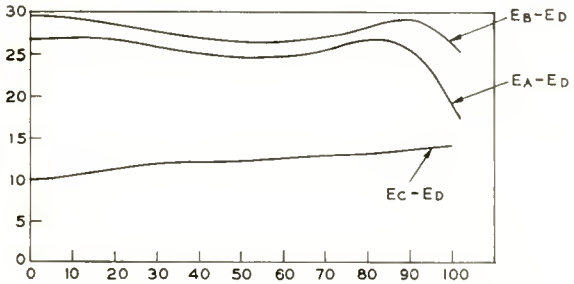

Fig. 30—Wide-band video amplifier response.

The plate network of V14 and a tuning adjustment of the interstage network between V13 and V14 allowed compensation for the above capacitance. The response of the video amplifier is shown in Figure 30, which indicates a 3-decibel bandwidth of 95 megacycles and a gain of 26 decibels. There is a loss of about 2 decibels in the summing tube V24 because of the greater than optimum grid bias adjustment to allow full pulse swing without drawing grid current. For small-signal operation, a gain of 3 decibels can be realized by use of optimum grid bias.

Provision is made to insert range blanking into the last video amplifier as well as gating in the first stage of the i-f amplifier. The use of 1N54-A diodes provides clamping action for the above function.

Figures 31 and 32 are photographs of the log amplifier. Figure 31, a left front view, shows the arrangement of the i-f, video, and summing amplifier stages. Careful shielding between stages and double filtering

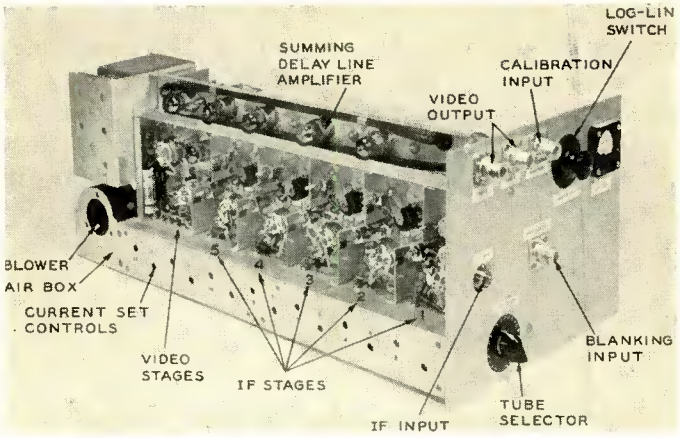

Fig. 31—Logarithmic amplifier, front view.

of all connections into each stage resulted in an amplifier singularly free of regeneration. The problem of providing adequate cooling of the 416B tubes was solved by using the bottom chassis as an air box from which plastic tubing through openings in the bases channelled air to both the grid and plate seals resulting in seal temperatures which were well below maximum allowable ratings.

The amplifier fits into one half standard aircraft ATR rack but the front panel was made large enough to support supplementary equipment for system operation.

Figure 32 is a right rear view of the amplifier. The crystal detector and logarithmatizing crystals are shown in the view. Figure 33 shows the amplifier with the shields in place and the front panel removed.

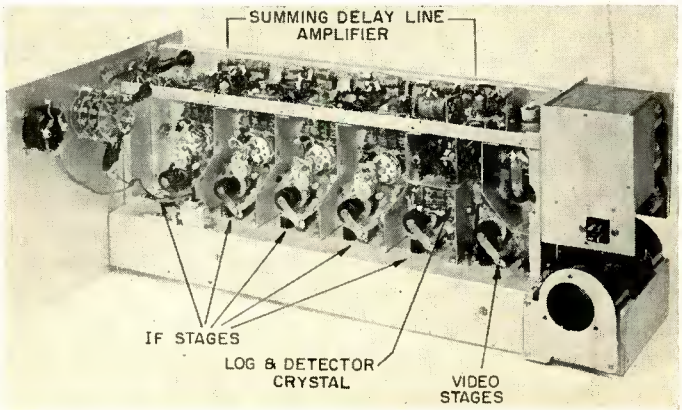

Fig. 32—Logarithmic amplifier, back view.

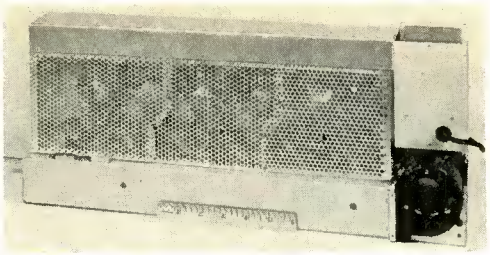

Fig. 33—Logarithmic amplifier with shields in place.

Dynamic Test of "Log-Lin" Amplifier

Figure 35 shows an arrangement to test the dynamic performance of the amplifier. VHF signal generator provides a 184-megacycle CW carrier to the "Narrow Pulse Modulator" which is triggered by the "Wide Pulse Generator" (0.3 microsecond) to produce a 10-millimicrosecond cosine-shaped pulsed carrier. The amplitude of output of this pulsed carrier can be linearly controlled by the calibrated attenuator of the signal generator. The pulsed 184-megacycle carrier is fed into the "Log-Lin" amplifier through a 170-ohm cable, and the amplifier video output goes into a 3-stage, rack-mounted, wide-band amplifier, as shown. The latter drives a low-capacitance high-intensity oscilloscope with provision for fast pulse photographic means. The wide pulse generator is also used to provide either sweep trigger for the scope at a 15-kilocycle repetition rate or the pulse rise itself may be used as the scope time base to expand to 10-millimicrosecond pulse on the face of the scope. Furthermore, the 0.3-microsecond pulse drives a triggered 55-megacycle oscillator which is used as a pulse-width calibrator ($\frac{1}{2}$ cycle $\approx$ 9 millimicroseconds). By superimposing both the pulse and the 55-megacycle sine wave, calibration is accurate regardless of the time-base linearity. A schematic diagram of the oscillator is shown in Figure 36.

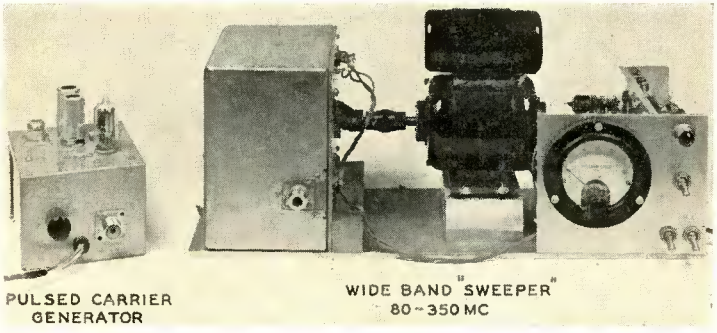

Fig. 34—Wide-band sweeping oscillator for amplifier alignment.

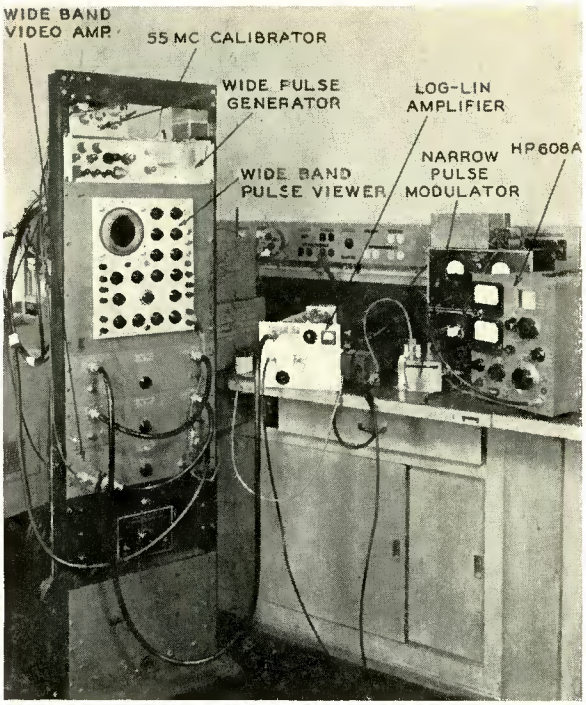

Fig. 35—10-millimicrosecond pulsed-carrier signal generator.

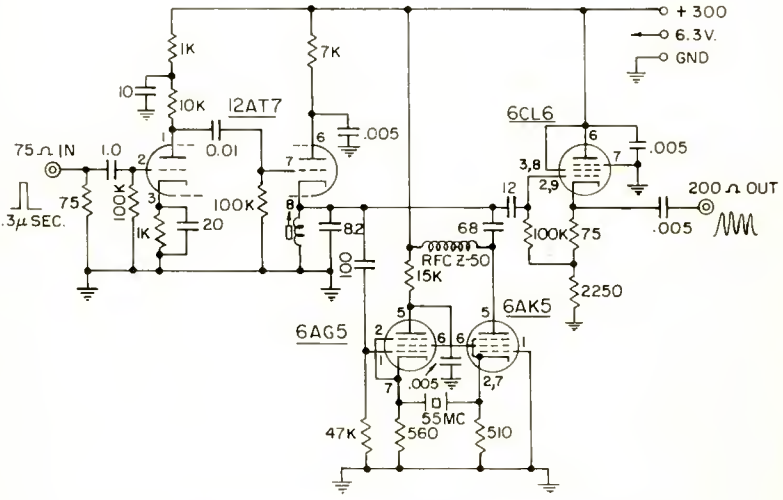

Fig. 36—Crystal-stabilized ringing circuit.

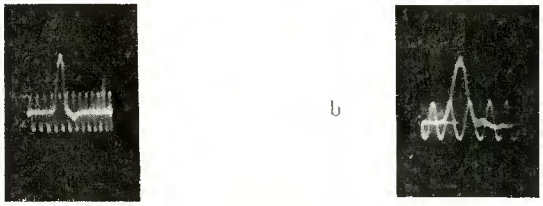

Fig. 37—Detected pulsed carrier signal generator output. (a) Sawtooth time base with 55-megacycle markers. (b) Pulse time base with 55-megacycle markers.

Figure 37 shows oscillograms of the detected output of the pulsed carrier signal generator, with the superimposed 55 megacycle sine wave calibrating voltage. In Figure 37a, the pulse is shown somewhat widened by the detector filter circuit on an expanded sawtooth sweep. In Figure 37b, the steep voltage rise of the .3-microsecond trigger pulse is used as a deflection means. This produces a sweep speed greater than 4 inches per microsecond, thus allowing quite accurate measurement of pulse shape and duration. The test pulse is estimated to be about 11 millimicroseconds at 3 decibels down and is made somewhat narrower than that of Figure 37a by the expedient of reducing the detector filter capacitance. Since this cannot be reduced below the minimum used in photographing Figure 37b, the actual signal generator pulse is approximately 10 millimicroseconds wide.

Figure 38 shows output pulses from stage 5. In Figure 38a the amplifier is in the linear mode and the input signal changed 20 decibels. In Figure 38b the same input signals are used but the amplifier is switched to the log mode. The degree of signal compression and the pulse shapes are very evident. It is estimated that at least 18 decibels of compression is attained at this input amplitude.

Figure 39 shows another comparison of the "Lin-Log" operation of stage 5. The video output is shown for constant signal input when the amplifier is switched from "Lin" to "Log" operation. About 18 decibels of compression is illustrated.

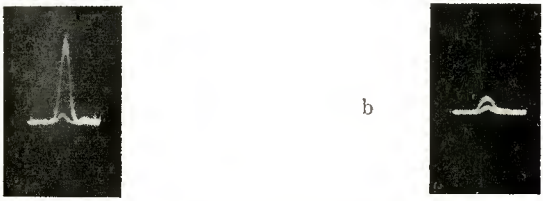

Fig. 38—Video output of stage 5. (a) Linear operation input signal ratio 20 decibels. (b) Log operation input signal ratio 20 decibels.

Figure 40 illustrates the operation of the complete amplifier including the video amplifier. Pulse *a* is the output with the amplifier in the linear mode and would rise to at least 3 times its height but for the internal shield in the XP-11 cathode-ray tube and test equipment overload. This is purposely expanded to show the various components of the composite logarithmic output, pulse *b*. Pulses *c*, *d*, and *e* are respectively the compressed outputs of stage 5, 4, and 3. Stage 2 output was evident, but too small to photograph under these conditions. It is important to note that the sequential stage outputs *do coincide in time*, which fact tends to confirm the assumption of equal time delay in the i-f and video channels. It might be noted that there is a small amount of decompression in the video amplifier for very low signals since the composite log pulse is slightly greater than the sum of its parts. This is difficult to overcome with normal tubes having positive G_m curvature in the cutoff region, but since the effect is quite small the increased

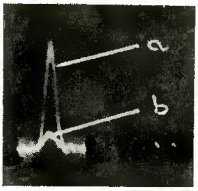

Fig. 39—Video output of stage 5 for constant signal input. (a) Linear mode. (b) Log mode.

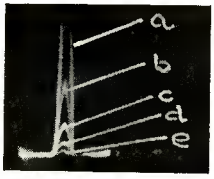

Fig. 40—Amplifier video output for constant signal input. (a) Linear mode. (b) Log mode. (c) Output of stage 5. (d) Output of stage 4. (e) Output of stage 3.

complexity resulting from wide-band compensation circuits makes their use unjustified.

In normal use of the amplifier at least 30 decibels of wide-band amplification precedes the input. Since the preamplifier was not available during these dynamic tests, the maximum dynamic range could not be shown nor could the appearance of signals in noise. The latter should appear quite similar to that in a linear system for weak signals, unless sufficient preamplification is used to drive the noise voltage amplitudes of approximately the r-m-s value into the compression region. This is normally not a desirable condition of operation because by keeping the noise amplitudes in the square-law region of the detectors, an improvement in S/N ratio is attained for signals in the vicinity of two times noise and higher.

If it is desired to have greater compression and a lower threshold, one or more 1N72 crystals can be paralleled with the two used in the amplifier described herein.

Dynamic Range

The dynamic range of the amplifier may be divided into two factors —the linear dynamic range and the compression dynamic range. In Figure 41, E_{limit} is the maximum detected voltage at the video input which will start to limit in the system.

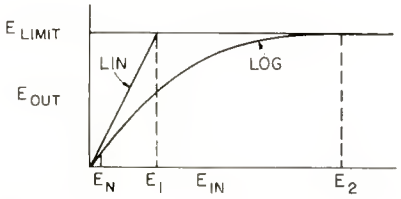

Fig. 41—E_{out} versus E_{in} for the "log-in" amplifier illustrating dynamic range.

For the linear amplifier, $E_{\text{limit}} = E_1 G^n$;

for the log amplifier $E_{\text{limit}} = E_2 nG$,

where E_1 and E_2 are the minimum input voltages to the amplifier which will produce saturation at the video input for the linear and log modes, respectively. Therefore

$$\frac{E_2}{E_1} = \frac{G^n}{nG} = \frac{G^{n-1}}{n},$$

and

$$\mathcal{R}_c = 20 \log \frac{E_2}{E_1} = (n-1)\ G_{db} - n_{db},$$

where $\mathcal{R}_c$ = compression dynamic range.

For $n = 5$, $G_{db} = 14$, $\mathcal{R}_c = 56 - 14 = 42$ decibels.

The total dynamic range $\mathcal{R}_t$ is $\mathcal{R}_c$ plus the linear range which is $\mathcal{R}_L = 20 \log (E_1/E_n)$, where E_n = the r-m-s noise voltage, the smallest useful voltage to be amplified. $\mathcal{R}_L \approx 25$ decibels. Therefore $\mathcal{R}_t = \mathcal{R}_c + \mathcal{R}_L = 67$ decibels.

Wide-Band I-F Sweep Generator

Because of the unavailability of test equipment for alignment and testing of wide-band circuitry for ten millimicrosecond pulsed carrier

systems, three experimental test equipments were built and extensively used in the log amplifier development program, namely:

1. Wide-band i-f sweep generator,
2. Wide-band video sweep generator,
3. Short-pulse-modulated carrier generator.

The wide-band i-f sweeper uses a "butterfly" circuit, as shown in Figure 42, to generate a sweep from 84 to 350 megacycles and provides about 1 volt into 50 ohms. Although no great effort was made to provide a linear sweep, the high-frequency end is sufficiently expanded to allow rapid alignment in that region. The position of the large output coupling loop, and the self resonance cathode circuit at the low-frequency end allow the equalization of output so that a maximum of 3 decibels amplitude variation occurs over the whole band. Figure 34 is a photograph of the sweeper showing the synchronous motor drive which allows scope synchronization to the line frequency.

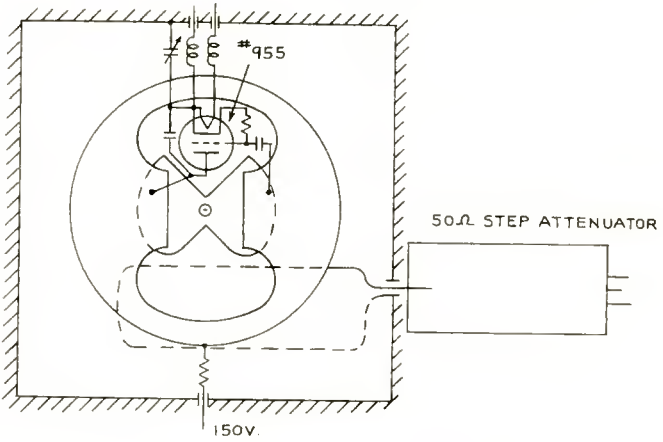

Fig. 42—Wide band i-f sweeper.

Ten-Millimicrosecond Pulsed-Carrier Generator

The schematic circuit of the pulse generator used in the dynamic testing of the log amplifier is shown in Figure 43. Here a trigger generator drives a type 1258 hydrogen thyratron with a 0.3-microsecond pulse, and a damped cosinusoidal oscillation of approximately 25 megacycles occurs in its plate circuit. C_1 adjusts the frequency, hence the width, of the half-cycle pulse which drives the screens of a balanced modulator. The latter consists of balanced ferrite cored transformers T_3 and T_4 and two 6AK5 pentodes. The r-f carrier input is fed anti-

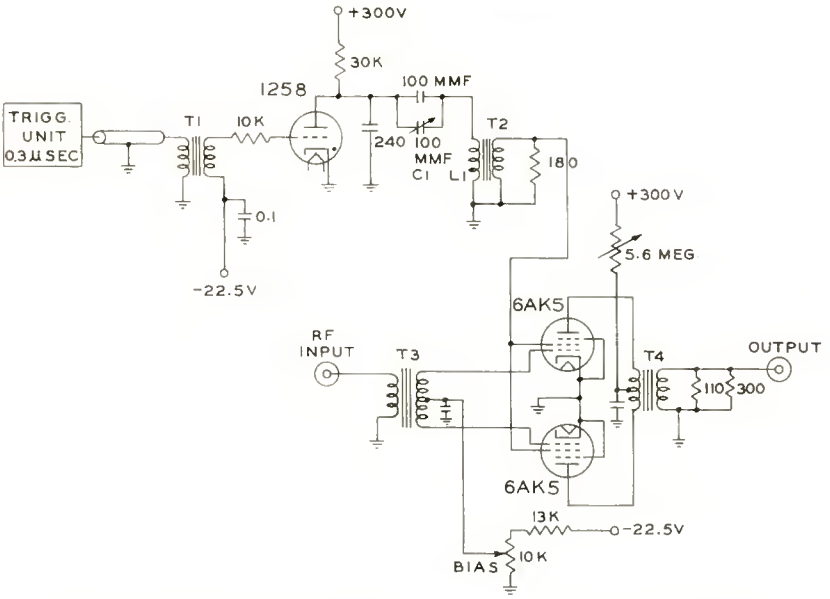

Fig. 43—Short pulse carrier generator (.01 to .03 microsecond).

phase at the grids while the pulse from T_2 is fed inphase to the screens. The use of a long-time-constant circuit in the 6AK5 plate supply insures that the modulator will conduct only on the first positive pulse cycle. By adjusting the 5.6-megohm resistor it is possible to get two or more pulses. A damper diode could also have been used to insure single-cycle firing, but the circuit used is flexible and effective. The grid-bias control allows the selection of the conduction point of the modulator, and hence the pulse width. Adjusting this in conjunction with C_1 allows the selection of a variable width undistorted cosine-shaped pulsed carrier whose amplitude may be controlled by the r-f input level. A photograph of the generator is shown in Figure 33.

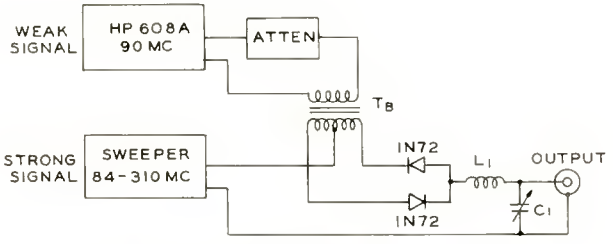

Fig. 44—Wide-band video sweep generator.

Wide-Band Video Sweep Generator

Figure 44 is the schematic diagram of a sweep generator which extends from 0 to 120 megacycles with a maximum of two decibels amplitude variation. This variation occurs mainly above 90 megacycles. The signal generator is maintained at 90 megacycles, with low output level relative to the wide-band i-f sweeper which provides a high level signal 84-300 megacycles (about 1 volt into 50 ohms) to the balanced modulator. The latter consists of a ferrite cored balanced transformer T_b, reversed 1N72 crystals, and an equalizing load filter L_1C_1. The use of a weak fixed signal and a sweeping strong signal insures that the beat (video) frequency be dependent in amplitude only on the weak (fixed) signal. Therefore amplitude variations up to 10 decibels in the sweeper across its frequency band will not appear in the video output.

The use of the video sweep in the alignment of the summing delay line was shown in Figure 22. Self-generating markers at 0, 30, 45, and 90 megacycles are evident on the oscillograms.

Conclusion

This paper describes a compact five-stage logarithmic amplifier having an over-all bandwidth of 180 megacycles centered at 180 megacycles and a total dynamic range of 67 decibels. The input signal required for 0.2 volt output from the fifth-stage detector in the linear mode is approximately 700 microvolts of 100 per cent modulated carrier at 180 megacycles. The amplifier input is impedance matched to a 170-ohm line to within ± 1 decibel over a 200-megacycle bandwidth. Additionally, a video amplifier of 90 megacycles bandwidth and 28 decibels gain feeding two parallel, matched, 170-ohm lines and driven by the logarithmic amplifier has been described. Means are included for the insertion of i-f amplifier gating, and for various blanking signals into the video amplifier. A novel method of continuous detection and wide-band video delay have been incorporated in the amplifier system.

Furthermore a description of amplifier alignment equipment using newly developed wide-band sweep, video, and ultra-short-pulse generators is included.

Acknowledgment

The crystal-stabilized ringing circuit (Figure 36) was constructed by K. H. Powers of RCA Laboratories.

Appendix

Some useful relationships for designing negative mutual delay lines are given below.

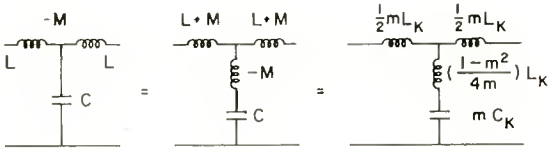

$L_K =$ series inductance of constant-K filter $= 2R_0/\omega_c$,

$C_K =$ shunt capacitance of constant-K filter $= 2/(\omega_c R_0)$,

$R_0 =$ terminating resistance $= \sqrt{\dfrac{L_k}{C_k}}$,

$\omega_c =$ angular cutoff frequency $= 1/(\pi R_0 C_k)$,

$L =$ series inductance of negative mutual filter $= \dfrac{m^2+1}{4m} L_k$,

$M =$ mutual inductance of negative mutual filter $= \dfrac{m^2-1}{4m}$,

$C = mC_k$,

$k =$ coefficient of coupling $= \dfrac{M}{L} = \dfrac{m^2-1}{m^2+1}$,

$m = \sqrt{\dfrac{1+k}{1-k}}$,

$x_K = \omega/\omega_c$,

$x_m = x_k/m$,

$\tau =$ time delay per section

$$= \frac{d\phi}{d\omega} = \frac{2}{\omega_c} \frac{m}{\sqrt{1-x_m^2}\,[1-x_m^2\,(1-m^2)]}$$

$$= \frac{2}{\omega_c} \frac{m^4}{\sqrt{m^2-x_k^2}\,[m^2-x_k^2\,(1-m^2)]}.$$

RCA TECHNICAL PAPERS†

Fourth Quarter, 1956

Any request for copies of papers listed herein should be addressed to the publication to which credited.

"Analytical Approaches to Local Oscillator Stabilization," W. Y. Pan and D. J. Carlson, *RCA Review* (December) 1956

"The Apparent Contact Potential of a Pseudo-Abrupt P-N Junction," H. Kroemer, *RCA Review* (December) 1956

"Bigradient Uniaxial Microphone," H. F. Olson, J. Preston, and J. C. Bleazey, *RCA Review* (December) 1956

"Camera Tubes for Color Television Broadcast Service," R. G. Neuhauser, *Jour. S.M.P.T.E.* (December) 1956

"Circuitry Report on RCA 21-Inch Color-TV Chassis," J. A. May and W. H. Fulroth, *Service* (October) 1956

"Conduction Band Structure of Germanium-Silicon Alloys," M. Glicksman and S. M. Christian, *Phys. Rev.* (December 1) 1956

"Contamination Gauge," E. O. Johnson, *Rev. Sci. Instr.* (December) (Notes) 1956

"Conversion of Airborne HF Receiver-Transmitter from Double Sideband to Single Sideband," H. A. Robinson, *Proc. I.R.E.* (December) 1956

"Dielectric Constant of Barium Orthosilicate," C. P. Hadley, H. W. Kraner, and M. R. Royce, *Jour. Appl. Phys.* (November) (Letter to the Editor) 1956

"Discharge Mechanism of Mercury Pool Arcs," K. G. Hernqvist, *Jour. Appl. Phys.* (October) 1956

"Electromechanical Filters for Single-Sideband Applications," D. L. Lundgren, *Proc. I.R.E.* (December) 1956

"An Electronic Thermostat," F. Cohen, *Rad. and Tele. News* (October) 1956

"Energy Levels of a Disordered Alloy," R. H. Parmenter, *Phys. Rev.* (October 1) 1956

"1500 Milliampere Power Supply For Broadcast TV Use," R. T. Ross and J. W. Wentworth, *Broadcast News* (October) 1956

"Key to Color TV Installation and Servicing," W. W. Cook, *Rad. and Tele. News* (December) 1956

"Latest Developments in VHF Television Transmitters," F. E. Talmage, *Broadcast News* (October) 1956

"Lighting for Color Opaques on Television," H. N. Kozanowski, *Jour. S.M.P.T.E.* (November) 1956

"Magnetic Properties of Zinc Sulfide Phosphors With Manganese Activator," S. Larach and J. Turkevich, *Jour. Physical Chemistry* (November) (Letter to the Editor) 1956

"Making the Microphone a More Versatile Acoustic Tool," R. M. Carrell and A. H. Lind, *Broadcast News* (December) 1956

† Report all corrections or additions to RCA Review, RCA Laboratories, Princeton, N. J.

"A Method of Predicting the Coverage of a Television Station," D. W. Peterson and J. Epstein, *RCA Review* (December) 1956

"A Miniature Vidicon of High Sensitivity," A. D. Cope, *RCA Review* (December) 1956

"Multiband Luminescence in Boron Nitride," S. Larach and R. E. Shrader, *Phys. Rev.* (October 1) 1956

"A New Ferrite Isolater," B. N. Enander, *Proc. I.R.E.* (October) ... 1956

"A New High-Gain Multiplier Phototube for Scintillation Counting," W. Widmaier, R. W. Engstrom, and R. G. Stoudenheimer, *Trans. I.R.E. PGNS* (November) 1956

"New Tubeless Convergence Circuit for RCA-21AXP22-A Color Kinescope," *RCA Application Note AN-168*, RCA Tube Division, Harrison, N. J. (December) 1956

"Phonetic Typewriter," H. F. Olson and H. Belar, *Jour. Acous. Soc. Amer.* (November) 1956

"Photoconductivity Speed of Response for High Intensity Excitation in Cadmium Sulfide and Selenide," R. H. Bube, *Jour. Appl. Phys.* (October) 1956

"Propagation Test on Microwave Communications Systems," H. R. Mathwich and Co-Authors, *Elec. Eng.* (November) 1956

"Quality Factor for Filters Whose Spectral Transmittances are Different from Color Mixture Curves, and Its Application to Color Photography," H. E. J. Neugebauer, *Jour. Opt. Soc. Amer.* (October) 1956

"Radio System Controls Railroad in Venezuela," B. Sheffield, *Electronics* (December) 1956

"RCA Developments in Worldwide Telecommunications," S. Sparks, *Wire and Radio Communications* (November) 1956

"Reduction of Co-Channel Television Interference by Precise Frequency Control of Television Picture Carriers," W. L. Behrend, *RCA Review* (December) 1956

"Replaceable Pole Tip Caps for CinemaScope Magnetic Reproduce Heads," M. Rettinger, *Jour. S.M.P.T.E.* (December) 1956

"Servicing RCA TV Portables," W. W. Cook, *Service* (October) 1956

"Single-Sideband Operation for International Telegraph," E. D. Becken, *Proc. I.R.E.* (December) 1956

"Some Problems Associated with Television AGC Circuits," L. P. Thomas, *RCA Rad. and Tele. Serv. News* (November) 1956

"Speech Communications in Noise: Some Equipment Problems," M. E. Hawley, *Jour. Acous. Soc. Amer.* (November) 1956

"SSB Receiving and Transmitting Equipment for Point-to-Point Service on HF Radio Circuits," H. E. Goldstine, G. E. Hansell, and R. E. Schock, *Proc. I.R.E.* (December) 1956

"Stability of Periodic-Field Beam Focusing," K. K. N. Chang, *Jour. Appl. Phys.* (December) 1956

"Stereophonic Microphone Placement," J. Cunningham and R. O. Jordan, *Audio* (November) 1956

"Test Signal for Measuring 'On-The-Air' Color-Television System Performance," R. C. Kennedy, *RCA Review* (December) 1956

"Thiourea, a New Ferroelectric," A. L. Solomon, *Phys. Rev.* (November 15) (Letter to the Editor) 1956

"Transistorized Television Cameras Using the Miniature Vidicon," L. E. Flory, G. W. Gray, J. M. Morgan, and W. S. Pike, *RCA Review* (December) 1956

"Tube Types for Audio Use," M. B. Knight, *Rad. and Tele. News* (November) 1956

"200-Mw-Output Battery-Operated Phonograph Amplifier Using RCA-2N109 Junction Transistors," *RCA Application Note AN-169*, RCA Tube Division, Harrison, N. J. (December) 1956
"The 'Universal' Voice-Control Circuit," L. O. Leigh, *QST* (November) 1956
"Use of Junction Transistors in Computer Amplifiers," W. A. Curtin, *Elec. Eng.* (November) 1956
"A Video Automatic-Gain-Control Amplifier," J. O. Schroeder, *RCA Review* (December) 1956
"Video Switching For TV Broadcast Centers," E. B. Pores, *Electronics* (December) 1956
"Viewing Storage Tubes for Large Displays," H. O. Hook, M. Knoll, and R. P. Stone, *RCA Review* (December) 1956
"The World We Face," D. Sarnoff, *Inter. Photographer* (December) 1956
Mathematics for Electronics with Applications, Henry M. Nodelman and Frederick W. Smith, Jr., McGraw-Hill Book Company, Inc., New York, N. Y. 1956

AUTHORS

WILLIAM E. BARNETTE matriculated at the University of Delaware in 1947. His studies were interrupted by a period of service with the U. S. Army, after which he returned to the University and received the B.E.E. degree in 1953. In June of 1953 he joined RCA Laboratories. In 1954, he was assigned to work in the Systems Research Laboratory, where he engaged in developing linear and logarithmic i-f amplifiers. Currently he is doing research in pulse code, digital communications and computer systems. Mr. Barnette is doing part-time graduate work in Electrical Engineering at Princeton University. He is a member of the Institute of Radio Engineers.

WALTER R. BEAM received the B.S. degree in Electrical Engineering from the University of Maryland. He pursued graduate work while serving as Instructor in Electrical Engineering at the same university, and received the M.S. degree in 1950. During part of this period he was also engaged in development of radio sounding instruments at Washington Institute of Technology. He joined the Microwave Tube group at RCA Laboratories in 1952. From 1952 to 1956 he was engaged in research on microwave amplifiers, electron guns and electron beam noise. In 1956 he became Manager of the Microwave Advanced Development activity of RCA Tube Division in Princeton. Dr. Beam is a member of the Institute of Radio Engineers, Tau Beta Pi, and Sigma Xi, and is a licensed Professional Engineer.

NORMAN DITRICK received the B.S. and M.S. degrees in Physics from Ohio State University in 1952. He joined RCA as a specialized trainee in July of 1952, and was later assigned to the Receiving-Tube Advanced Development Activity of the Tube Division. He was transferred to the Semiconductor Advanced Devices Development Activity in April of 1953 and, since that time, has been working principally on high-frequency transistor development. Mr. Ditrick is a member of Sigma Pi Sigma, Tau Beta Pi, and the Institute of Radio Engineers.

AARON L. KESTENBAUM received the B.S. degree in Engineering Physics from Lehigh University in 1948 and the M.S. degree in Physics from New York University in 1953. He has worked in the field of solid-state devices since 1950, and joined the Semiconductor Design activity of the RCA Tube Division in Harrison, New Jersey in 1953. Mr. Kestenbaum is presently a project leader on the germanium drift transistor program in the Advanced Development activity of the RCA Semiconductor Division at Somerville, N. J.

HARRY KIHN received the B.S. degree in Electrical Engineering from the Cooper Union Institute of Technology in 1934 and the M.S. degree from the University of Pennsylvania in 1952. Prior to joining RCA he was employed by the Hygrade-Sylvania Co., Polytherm (his own company), and the Ferris Instrument Company. He joined the RCA Manufacturing Company in Camden in 1939 and engaged in television field testing, receiver circuit development, and research in frequency modulation, fluctuating noise, ferromagnetic materials, and the APN-1 radio altimeter. In 1942, he was transferred to RCA Laboratories in Princeton, where he engaged in research on X-band receivers, silicon crystals, frequency modulation radar, automatic bombing devices, and the APN-22 altimeter. With the advent of color television, he participated in the development and design of the field test receivers. In 1953, he transferred to the System Research Laboratory, where he is doing research on millimeter wave high resolution radar. He is now directing research in pulse code and digital communication and computer systems. Mr. Kihn is a member of the Institute of Radio Engineers, Sigma Xi, and the Operations Research Society of America.

RONALD C. KNECHTLI received the Diploma in Electrical Engineering from the Swiss Federal Institute of Technology. He spent the academic year 1951-1952 at the Massachusetts Institute of Technology, where he pursued graduate studies while serving as a Research Assistant in the Research Laboratory of Electronics. From 1952 to 1953, he worked in the microwave laboratory of Brown Boveri (Switzerland). He joined the Microwave Tube group at RCA Laboratories in 1953. In 1955 he was awarded the Ph.D. degree from the Swiss Federal Institute of Technology. Since joining RCA, he worked on microwave tubes and electron guns. Dr. Knechtli is a member of the Institute of Radio Engineers, Sigma Xi, and the Committee on Vacuum Techniques.

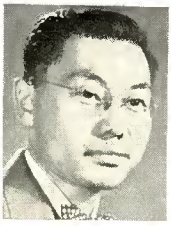

T. MURAKAMI received the B.S. degree in E.E. from Swarthmore College in 1944, and the M.S. degree from the Moore School of Electrical Engineering, University of Pennsylvania in 1947. From 1944 to 1946 he was an assistant and research associate in the Department of Electrical Engineering at Swarthmore College. Since 1946 he has been with the Advanced Development Section of the RCA Victor Television Division, Camden, N. J., working on radio frequency circuit development. Mr. Murakami is a Senior Member of the Institute of Radio Engineers and a member of Sigma Xi.

YONA PELESS received the B.S. degree in Electrical Engineering in 1953 and the Diplome Ing. in 1954 from the Israel Institute of Technology. During the years 1953-1955 he was assistant instructor at that institution. In 1955 he came to RCA on a special training program where he worked on television systems and circuitry. He is now studying for the M.S. degree at the Moore School of Electrical Engineering, University of Pennsylvania, where he is studying interference and noise in telecommunications. Mr. Peless holds a scholarship from the Hebrew Technical Institute.

JAMES W. SCHWARTZ received the B.S. and M.S degrees in Engineering Physics from Cornell University in 1951 and 1952 respectively. He has been employed at the Corning Glass Works and at Oak Ridge National Laboratories. Since December of 1952 when he joined the technical staff of RCA Laboratories, he has been engaged in electron optics and picture reproducer research. Mr. Schwartz is a member of the Institute of Radio Engineers and Sigma Xi.

WIESLAW W. SIEKANOWICZ received the B.S. degree in electrical engineering from the Imperial College of Science and Technology, London University, England, in 1948, and the M.S. degree in electrical engineering from Columbia University in 1950. He joined the RCA Tube Division at Harrison, N. J., in July, 1950, transferring to Princeton in 1956, and has worked in the microwave advanced development activity on traveling-wave tubes and electron beams. Mr. Siekanowicz is a member of the Institute of Radio Engineers and Sigma Xi.

FRED STERZER received the B.S. degree in physics from the City College of New York in 1951, and the M.S. and Ph.D. degrees in physics from New York University in 1952 and 1955, respectively. He worked for the Allied Control Co. in New York City from 1952 to 1953. During the school year of 1953 to 1954 he was an instructor in physics at the Newark College of Engineering in Newark, N. J., and a research assistant at New York University working on microwave spectroscopy. He joined the RCA Tube Division in Harrison, N. J., in October, 1954, and transferred to Princeton in 1956. His work with the microwave tube advanced development activity is concerned primarily with traveling-wave tubes and backward-wave oscillators. Dr. Sterzer is a member of Phi Beta Kappa, Sigma Xi, the American Physical Society, and the Institute of Radio Engineers.